



저작자표시-비영리-변경금지 2.0 대한민국

이용자는 아래의 조건을 따르는 경우에 한하여 자유롭게

- 이 저작물을 복제, 배포, 전송, 전시, 공연 및 방송할 수 있습니다.

다음과 같은 조건을 따라야 합니다:



저작자표시. 귀하는 원저작자를 표시하여야 합니다.



비영리. 귀하는 이 저작물을 영리 목적으로 이용할 수 없습니다.



변경금지. 귀하는 이 저작물을 개작, 변형 또는 가공할 수 없습니다.

- 귀하는, 이 저작물의 재이용이나 배포의 경우, 이 저작물에 적용된 이용허락조건을 명확하게 나타내어야 합니다.
- 저작권자로부터 별도의 허가를 받으면 이러한 조건들은 적용되지 않습니다.

저작권법에 따른 이용자의 권리는 위의 내용에 의하여 영향을 받지 않습니다.

이것은 [이용허락규약\(Legal Code\)](#)을 이해하기 쉽게 요약한 것입니다.

[Disclaimer](#)

Ph. D. Dissertation

**Investigation on electrochemical reaction mechanisms
of lithium-ion battery electrode materials
by transmission electron microscopy**

투과전자현미경을 통한 리튬이온전지
전극 재료의 전기화학 반응 메커니즘 연구

by

Seungyong Lee

February 2017

**Department of Materials Science and Engineering
College of Engineering
Seoul National University**

**Investigation on electrochemical reaction mechanisms
of lithium-ion battery electrode materials
by transmission electron microscopy**

Advisor: Prof. Miyoung Kim

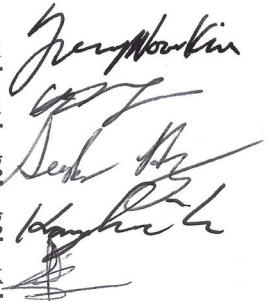
by
Seungyong Lee

A Dissertation Submitted to the Faculty of the Graduate School of
Seoul National University in Partial Fulfillment of the Requirements for
the Degree of Doctor of Philosophy
Department of Materials Science and Engineering

February 2017

**Approved
by**

Chairman of Advisory Committee: Young-Woon Kim
Vice-chairman of Advisory Committee: Miyoung Kim
Advisory Committee: Seong-Hyeon Hong
Advisory Committee: Kisuk Kang
Advisory Committee: Gyeong-Su Park



ABSTRACT

Investigation on electrochemical reaction mechanisms of lithium-ion battery electrode materials by transmission electron microscopy

Seungyong Lee

Department of Materials Science and Engineering

The Graduate School

Seoul National University

Having high energy densities, lithium ion rechargeable batteries are widely used for portable electronic devices, and they are still the subject of intensive investigation because of the possibility on a wide range of future applications including battery-only electric vehicles. To identify the electrochemical reaction mechanisms of lithium-ion battery electrode materials and suggest the appropriate directions for the improvement of the performance, there have been numerous researches using various analysis methods. In particular, transmission electron microscopy (TEM) studies can provide significant information on the electrochemical reaction mechanisms of lithium-ion battery at nano-scale, but there have been a lot of limitations due to the requirements of special configuration and sampling techniques that are compatible to the lithium-ion battery system. Here, we have focused on the better approaches to TEM investigation of lithium-ion battery electrode materials that can well describe and explain the electrochemical reactions in the lithium-ion battery. We improved TEM investigation techniques and applied properly for specific purpose of studies on lithium-ion battery electrode materials.

First, to reveal the origin of fast capacity fading shown in Ni-rich NCM cathode material, we directly compared the inside of secondary particles between NCM 1/1/1 and 8/1.5/0.5 materials by using FIB sampling technique. The observation on the cross-section of the same secondary particles before and after the electrochemical cycles clearly showed the micro-cracks between primary particles and the severe surface degradation in Ni-rich NCM material, which should be the major source of fast capacity fading. We revealed that the instability of Ni^{3+} ions in Ni-rich NCM material may result in the severe surface degradation by causing the structural transformation and transition metal-ion dissolution into the electrolyte from the surface of primary particles. Also, it was identified that the low-angle grain boundaries in a primary particle can also act as the surface of primary particles, which even lead to the development crack in the primary particle.

Furthermore, we improved the *ex situ* TEM experimental method to track the phase evolution of SnO_2 anode material and reveal the possibility of reverse conversion reaction and the origin of the additional capacity, which has been controversial. SnO_2 particles dispersed on a carbon film-coated copper TEM grid were placed with the conventional SnO_2 slurry electrode in a coin battery cell and electrochemically (dis)charged toward specific voltages to investigate the phase evolution of the same particles during the first full cycle by TEM. By this method, we demonstrated that reactions of Li_2O phase contribute to the extra capacity and the reverse conversion reaction of SnO_2 hardly occurs in the real battery system.

Finally, we applied the *in situ* TEM experimental technique to identify the actual lithium-ion diffusion paths and the lithiation mechanism of tunnel-structured MnO_2

nanowire. By setting up the special configuration using a carbon film-deposited copper TEM grid, we verified the facile diffusion through the unique tunnels in the α -MnO₂ nanowire rather than through the side wall of the nanowire. In addition, we revealed the precise lithiation mechanism of α -MnO₂ material up to the full-lithiation procedure. It was exposed that MnO intermediate phase appears during the conversion reaction of α -MnO₂ material. It was inferred that the MnO phase is developed at the original position of Mn ions in the octahedral site of the oxygen framework with the partial collapse of the tunnel structure. Moreover, we revealed that lithium and oxygen ions well maintain the 1-D array along the tunnels even after the full lithiation.

These studies suggest the robust TEM experimental methods which are widely applicable to the battery analysis. Furthermore, the studies provide the further profound information on the electrochemical reaction mechanisms of various promising lithium-ion battery electrode materials.

Keywords: Lithium-ion battery, electrochemical reaction mechanism, transmission electron microscopy (TEM), in situ transmission electron microscopy (in situ TEM), lithium nickel cobalt manganese oxide, tin oxide (SnO₂), manganese oxide (MnO₂).

Student Number: 2012-24165

Table of Contents

Abstract	i
Table of Contents	iv
List of Tables	vii
List of Figures	ix

Chapter 1. General introduction

1.1. Thesis overview	1
1.2. Lithium-ion battery	5
1.2.1. Principles of lithium-ion battery	5
1.2.2. Insertion reaction for cathode materials.....	8
1.2.3. Conversion reaction for anode materials.....	10
1.3. Transmission electron microscopic approaches on the analysis of lithium-ion battery	11
1.3.1. Electron diffraction.....	12
1.3.2. Atomic-resolution HAADF/ABF-STEM imaging	14
1.3.3. Electron energy loss spectroscopy.....	16
1.3.4. <i>In situ</i> I-V TEM measurement.....	18

Chapter 2. Visualization on degradation of Ni-rich Ni/Co/Mn cathode material

2.1. Introduction	20
2.2. Structural characterization of pristine NCM cathode material	23
2.3. Structural evolution of NCM cathode material during electrochemical cycles	29

2.3.1. Structural transformation at the surface of primary particles.....	29
2.3.2. Lithium-ion defects at tetrahedral position.....	35
2.4. Comparison between NCM 1/1/1 and 8/1.5/0.5 materials.....	37
2.4.1. Surface deterioration of primary particles	37
2.4.2. Crack development in primary particles	45
2.5. Summary.....	51

Chapter 3. Extra capacity of SnO₂ anode in lithium-ion battery investigated by *ex situ* TEM analysis

3.1. Introduction.....	53
3.2. Experimental details	56
3.2.1. Directly (dis)chargeable TEM grid electrode preparation.....	56
3.2.2. Electrochemical characterization and TEM analysis.....	57
3.3. Over-capacity phenomenon of the SnO ₂ anode material.....	58
3.4. Realistic <i>ex situ</i> TEM investigation technique for the analysis	62
3.4.1. Preliminary <i>ex situ</i> X-ray diffraction analysis of the SnO ₂ /Li battery.....	62
3.4.2. <i>Ex situ</i> TEM experimental procedure.....	64
3.5. Phase evolution in the discharge process.....	70
3.5.1. Inference on the source of LiOH phase.....	73
3.5.2. Inference on the source of nano-crystalline Li ₂ O phase	74
3.6. Details of phase indexing from SAED patterns	77
3.6.1. Identification of LiOH phase	77
3.6.2. Identification of nano-crystalline Li ₂ O phase.....	80
3.6.3. Identification of tetragonal SnO phase	80
3.6.4. Examination of electron beam effect on filmy layers.....	81
3.7. The unknown reactions in the charge process.....	83
3.7.1. Reactions of Li ₂ O phase as a major contributor to the extra capacity.....	83
3.7.2. An assessment of the possibility of the reverse conversion reaction.....	92
3.8. Summary.....	94

**Chapter 4. *In situ* TEM investigation on lithiation mechanism of
Tunnel-structured α -MnO₂ nanowire**

4.1. Introduction	96
4.2. Experimental details	99
4.2.1. Material synthesis and characterization.....	99
4.2.2. In situ TEM measurement.....	99
4.3. Structural characterization of α -MnO ₂ nanowire	100
4.4. Actual lithiation path in a tunnel-structured α -MnO ₂ nanowire	103
4.5. Structural evolution of α -MnO ₂ nanowires during lithiation procedure	108
4.5.1. Overall phase evolution of a single nanowire	108
4.5.2. MnO intermediate phase formation during conversion reaction	113
4.5.3. Structural relationship between α -MnO ₂ and Li ₂ O phases.....	125
4.6. Summary.....	131

Chapter 5. Conclusion 133

References..... 137

Abstract (in Korean)..... 149

List of Tables

- Table 2.1** Inductively coupled plasma atomic emission spectroscopy (ICP-AES) data from a full cell battery. Figure 1.2 Atomic structural model of LiCoO_2 cathode material.
- Table 2.2** Comparison of average primary particle size before and after electrochemical cycles in NCM 8/1.5/0.5 material.
- Table 3.1** Experimental and theoretical capacities of the first cycle of the SnO_2/Li and Sn/Li batteries. The influence of additives (Figure 3.2) was subtracted from the experimental capacities. The over-capacity rate was derived by dividing the experimental capacity by the theoretical capacity.
- Table 3.2** Statistical chart of indexed phases from various experimental data from the SnO_2/Li battery. The number of investigated positions in which the material increased or decreased from the previous stage was counted for each investigated transmission electron microscopy (TEM) grid electrode sample. The ratio of the increased/decreased number of each material to the number of total investigated positions in one grid electrode sample is expressed as a fraction. The increment/decrement of the material in each stage is inferred by comparing the diffracted peaks and the intensities of the selected-area electron diffraction (SAED) patterns from the previous stage. The first TEM investigated stage was diversified to enhance the reliability of the experiment. The fractional numbers recorded for the first investigated stage of each sample indicate the proportions of the material present.
- Table 3.3** Statistical chart of indexed phases from various experimental data from the Sn/Li battery. The chart is in the same format as Table 3.2. A detailed explanation of the table is provided in the caption to Table 3.2.
- Table 3.4** Simulated electron powder-diffraction data in the form of tables for the Miller indices, interplanar spacings, and corresponding relative intensities. JEMS code was used for the simulation. Kirkland's atomic form factors

were taken from simulations. These data were utilized to index the SAED patterns obtained from this experiment. Crystal data were taken from the following ICDD files: #04-004-7747 for tetragonal Sn, #04-014-6265 for cubic Sn, #04-012-6191 for tetragonal LiOH, #04-001-8930 for cubic Li₂O, and #04-005-4540 for tetragonal SnO.

Table 3.5 A summary of phase evolution of SnO₂ anode material in lithium-ion batteries. Significant phase changes are written on each stage.

List of Figures

- Figure 1.1** Schematic illustration of lithium-ion battery working principles.
- Figure 1.2** Atomic structural model of LiCoO_2 cathode material.
- Figure 1.3** Schematic illustration of Bragg condition.
- Figure 1.4** A photo of the *in situ* I-V TEM holder produced by Nanofactory.
- Figure 1.5** Schematic illustration of the *in situ* TEM experimental configuration for lithium-ion battery.
- Figure 2.1** Atomic model structure of NCM cathode material in [110] zone axis.
- Figure 2.2** Voltage vs. capacity profiles of NCM cathode materials with different composition ratios. (a) Charge/Discharge curves at the first cycle after the activation cycle. (b) Discharge curve at the first and the 50th cycle.
- Figure 2.3** A cross-sectional SEM image of a secondary particle of NCM 111 cathode material.
- Figure 2.4** (a) A representative ABF-STEM image of a primary particle from NCM 111 cathode material. (b) FFT pattern from an atomic-resolution HAADF-STEM image at the region indicated in (a). (c, f, g) Atomic-resolution HAADF-STEM images of corresponding regions indicated in (a). (d, e) FFT pattern from the indicated regions in (c).
- Figure 2.5** (a–c, e–g) Crystal orientation maps obtained from (a–c) NCM 1/1/1 and (e–g) 8/1.5/0.5 materials. (d, h) Disorientation relationship of grains in primary particles
- Figure 2.6** Atomic-resolution (a) HAADF- and (b) ABF-STEM images of pristine NCM cathode material. The atomic structure model is superposed onto each image.
- Figure 2.7** (a, b) HRTEM images and (c, d) FFT patterns of 300 cycled NCM 8/1.5/0.5 cathode material. (e, f) Corresponding atomic structure models at the region (c) and (d), respectively.
- Figure 2.8** Two example sets of dark-field imaging of 300 cycled NCM 8/1.5/0.5

cathode material. (a) A SAED pattern of the primary particle. (b, e) Bright-field images. (c, d, f, g) Dark-field images obtained from the (c, f) DF-01 and (d, g) DF-02 peaks indicated in (a).

Figure 2.9 (a, b) HAADF-STEM images of NCM 8/1.5/0.5 cathode materials after 300 cycles with 1C current rate. (c, d) Line-scanned intensity profiles along the indicated arrows in the HAADF-STEM images in (a) and (b).

Figure 2.10 (a, b) An example set of atomic-resolution (a) HAADF- and (b) ABF-STEM images showing the occupancy of lithium ions at tetrahedral sites after 300 cycles. (c) Line-scanned intensity profile of STEM images. (d) Atomic structure model of NCM cathode material with lithium ions at octahedral and tetrahedral sites.

Figure 2.11 SEM Cross-sectional images of secondary particles of NCM cathode material. Structural deterioration after 50 cycles was compared between (a, c) NCM 1/1/1 and (b, d) 8/1.5/0.5 materials.

Figure 2.12 Low-magnification (c, d, f) TEM and (a, b, e) ABF-STEM images of 300-cycled NCM (a, c, e) 1/1/1 and (b, d, f) 8/1.5/0.5 cathode materials.

Figure 2.13 Atomic-resolution HAADF-STEM images obtained near the surface of 300-cycled primary particles of (a, c, e) NCM 1/1/1 and (b, d, f) 8/1.5/0.5 cathode materials.

Figure 2.14 HRTEM analysis of crack points, which identifies the region where the crack occurs in the Ni-rich NCM cathode material. (a) A HAADF-STEM image at the crack developed primary particle. (b, c, e, f) FFT patterns from HRTEM images taken at the regions indicated in (a). (d, g) Atomic structural models corresponding to the regions indicated next to the models. (h) Atomic structural model showing the original crystal orientation relationship of the crack region. (i) SAED pattern at the zone axis tilted 5 degrees from the direction shown in (f).

Figure 2.15 Another example of the crack development in a single primary particle. (a) A HAADF-STEM (upper) and a HRTEM image (lower) at the crack developed primary particle. (b-e) FFT patterns from HRTEM images showing the direction of each region. (f) Atomic structural model of the

interested region before the crack development.

Figure 2.16 Noticeable cation mixing phenomenon at low-angle grain boundary (a) A low-magnification ABF-STEM image of the grain boundary region. (b) HAADF- and (c) ABF-STEM images show that the migration of transition metal ions is remarkable near the grain boundary.

Figure 2.17 Schematic illustration of the degradation of Ni-rich NCM cathode material.

Figure 3.1 Electrochemical characteristics of the SnO_2/Li battery tested between 0.001 and 2.5 V (vs. Li/Li^+). (a) Voltage vs. specific capacity profiles of the first cycle for various current rates with thermodynamic titration curves. (b) Cyclic voltammograms of the first, second, third, fifth, and tenth cycles at a scan rate of 0.1 mV s^{-1} . (c) Voltage vs. specific capacity profiles of the first, second, third, fifth, and tenth cycles at a current rate of 100 mA g^{-1} . The label 'Reaction A' indicates the controversial reaction curve of the SnO_2/Li battery system.

Figure 3.2 Voltage versus specific capacity profiles of the polyvinylidene fluoride (PVDF) binder-Super P carbon black conductive agent mixture, tested over the voltage range from 0.001 to 2.5 V (vs. Li/Li^+). The results from two test samples are shown. The binder and the conductive agent were mixed at a ratio of 1:2, the same ratio as that used for the slurry electrode. The other components of the cell were identical to the case shown in Figure 3.1. Five cycles at a current rate of 20 mA g^{-1} are shown for each.

Figure 3.3 Voltage versus specific capacity profile of the first cycle of the Sn/Li battery at a current rate of 20 mA g^{-1} , drawn with thermodynamic titration curves. The blue dash-lined circle indicates the corresponding region of the controversial reaction (Reaction A) in the SnO_2/Li battery shown in Figure 3.1.

Figure 3.4 Ex situ X-ray diffraction (XRD) results for SnO_2 slurry electrodes at various discharge/charged stages. The SnO_2 slurry electrodes were discharged and charged in the coin cell toward specific voltage points of interest. XRD data were collected in the 2θ range of $15\text{--}65^\circ$, in 0.01° increments. (a) Pristine SnO_2 slurry electrode before being charged or

discharged in the coil cell. The slurry electrodes were fully discharged and charged toward (b) the end of Stage IV (1 V) and (c) Stage V (2.5 V). The reference data for the related materials shown in the figures were obtained from the database of International center for diffraction data (ICDD): #00-041-1445 for tetragonal SnO₂, #04-005-4540 for tetragonal SnO, and #04-004-7747 for tetragonal Sn.

Figure 3.5 (a) Schematic diagram of the experimental technique for investigating the actual electrochemical reaction mechanisms of SnO₂ lithium-ion battery anode materials using *ex situ* TEM analysis. (b) Voltage vs. specific capacity profile, drawn in continuous form, of the first cycle of the SnO₂/Li battery, reproduced from Figure 3.1a. The division marks for Stages I to V indicate the states of charge investigated in this work.

Figure 3.6 (a, d, g, j) TEM images of traced SnO₂ particles on the grid, (b, e, h, k) their corresponding SAED patterns, and (c, f, i, l) background removed radial intensities of the SAED patterns in (a, b, c) the pristine state, (d, e, f) Stage I, (g, h, i) Stage II, and (j, k, l) Stage III. (b, e, h, k) The letters in parentheses next to the chemical formulas in the SAED patterns indicate the crystal structures of the materials (T = tetragonal, C = cubic). (c, f, i, l) Interplanar spacing and the corresponding relative intensities of the reference materials are shown. The data from Table 3.4 were used as reference data.

Figure 3.7 Representative example of the SAED patterns of trace Sn particles for (a) Stage II and (b) Stage III. The removed background radial intensities of the SAED patterns are shown next to each pattern. Reference electron diffraction data of the indexed materials (from Table 3.4) are shown in each radial intensity graph.

Figure 3.8 Voltage versus specific capacity for the first cycle of a Sn/Li battery in continuous form, reproduced from Figure 3.3. The division marks from I to V indicate the investigated states of charge. Each stage corresponds to the same voltage range as that used for the SnO₂/Li battery in this research.

Figure 3.9 Two representative SAED pattern examples of trace SnO₂ particles for Stage V, which have crystalline peaks corresponding to the (200) plane of

the tetragonal SnO phase. The relevant peaks are marked in the figures. The corresponding transmission electron microscopy (TEM) images of the SAED patterns are shown in the insets to the figure.

Figure 3.10 (a,b,d,e) SAED patterns acquired consecutively, for 15 seconds respectively, and (c,f) background removed radial intensity profiles of the SAED patterns. The SAED patterns obtained where (a,b) LiOH and (d,e) Li₂O are clearly visible respectively. (a,b,d,e) The contrast of the SAED patterns were inverted for better recognition. (c,f) Background radial intensities were removed using a power law. The *x*-axis was arranged in reciprocal form. There was almost no differences on the radial intensity profiles between the 1st and 2nd acquirement. It signifies that LiOH and Li₂O materials were hardly affected by TEM electron beam.

Figure 3.11 (a, b) A representative example of SAED patterns of traced SnO₂ particles from Stages IV and V and (c) background removed radial intensities of the SAED patterns. The example shows the decrement in Li₂O and slight increment in LiOH phases between Stages IV and V. The radial intensities were normalized for compensating the difference of acquisition times between the two SAED patterns. The corresponding TEM images of the SAED patterns at the recorded locations are shown in the inset to each figure.

Figure 3.12 Experimental EEL spectra of (a) Li *K*- and (b) O *K*-edges in Stage IV and V. The EEL spectra were recorded in an energy-filtered TEM mode at an accelerating voltage of 80 kV. The spectra from Stage IV and V were obtained from separate grid electrodes which dis/charged straight toward Stage IV and V respectively.

Figure 3.13 The collected experimental EEL spectra of Li *K*-edge in (a) Stage IV and (b) Stage V. The EEL spectra were recorded in an energy-filtered TEM mode at a 80 kV accelerating voltage. The spectra from Stage IV and V were obtained from separate grid electrode samples. Red dashed lines on both figures indicate the energy positions showing sharp peaks in Stage IV. (a) The EEL spectra show that most of them contain Li₂O phase in Stage

IV. (b) The spectra in Stage V signify that Li_2O phase was transformed to other phase in this stage.

Figure 3.14 An example set of SAED patterns obtained in the same experimental condition with the EELS measurements using 80 kV TEM instrument (Titan G2 Cube 60-300, FEI). The SAED patterns were obtained from the TEM grid electrodes dis/charged straight toward (a) Stage IV and (b) V each. Therefore, the samples had no chance to be exposed and crystallized in air. Background removed radial intensity profiles are also expressed on the right side of each SAED pattern. Nano-crystalline Li_2O phase is not observable due to its amorphous structure. It confirms that Li_2O was already exist in amorphous structure during the EELS measurement in Stage IV and V.

Figure 3.15 Li-p conduction band partial density of states (PDOS) calculation results of (a) cubic Li_2O and (b-n) various Li-deficient lithium oxide. Corresponding numbers of Li atoms were extracted from the unit cell of the cubic Li_2O phase to realize lithium-deficient lithium oxide. All possible configurations of Li atoms were considered for each Li_xO phase ($x=1.00, 1.25, 1.50, 1.75$). Relaxed structures of each Li_xO phase were shown as insets in each figure. The Fermi-levels were aligned in the middle of each band gap.

Figure 3.16 The experimental EEL spectra of Li K -edge obtained in (a) Stage IV and (b) Stage V compared with Li-p orbital partial density of states (PDOS) calculation results. Blue, black, and red curves indicate the experimental EELS spectra, the calculated Li p-character PDOS, and smoothed PDOS by fast fourier transform (FFT) filter, respectively. The smoothed PDOS curves show the predicted practical curves that can be obtained from the EELS experiment. (a) Li_2O PDOS curve is identical to the PDOS from Figure 3.15a. (b) Li_xO PDOS indicates the averaged PDOS of various Li-deficient Li_xO phase ($x=1.00, 1.25, 1.50, 1.75$), which are shown in Figure 3.15b-n.

Figure 3.17 Representative SAED patterns of trace (a, b) SnO_2 and (c, d) Sn particles

showing the emergence of the SnO tetragonal phase between Stage IV and V. The contrast in the SAED patterns was inverted, and the indexed materials were marked on the SAED patterns together with Miller indices and interplanar spacing. The corresponding TEM images of the SAED patterns are shown in the inset to each figure.

Figure 4.1 Crystallographic structural information of pristine potassium α -MnO₂ nanowire material. (a) PXRD pattern of potassium α -MnO₂ nanowires. (b, c) Atomic model structures of K₂Mn₈O₁₆ along the (b) $\langle 100 \rangle$ and (c) $\langle 001 \rangle$ zone axes. One $[2 \times 2]$ tunnel is indicated with a red dashed box. (d) TEM image of a single potassium α -MnO₂ nanowire. (e) HAADF-STEM image of a single nanowire along the $\langle 100 \rangle$ zone axis and (f) its FFT pattern. Corresponding planes of diffraction spots are described on the FFT pattern. (g, h) Atomic-resolution HAADF-STEM images of the nanowire along the (g) $\langle 100 \rangle$ and (h) $\langle 001 \rangle$ zone axis. The images were filtered by the inverse FFT method. Atomic model structures of potassium α -MnO₂ (K₂Mn₈O₁₆) are shown on each image.

Figure 4.2 Schematic illustration of the conventional *in situ* TEM experimental setup for the observation of lithiation into the nanowire materials.

Figure 4.3 (a) Schematic illustration of the configuration of a coin cell battery at the cross-sectional view. (b) Schematic illustration of the working electrode environment with nanowire electrode materials.

Figure 4.4 In situ TEM experiment for identifying actual lithiation paths in α -MnO₂ nanowire material. (a) Schematic diagram of in situ TEM experiment for investigation of the preferred Li-ion diffusion path in potassium α -MnO₂ nanowires. (b) A low-magnification TEM image of the in situ experiment, which was taken before applying a bias voltage. Nanowires are laid on carbon support film and Li_xO is in contact with the upper side of the carbon support film. The starting point of the nanowire is shown enlarged in the inset. The green box indicates the region recorded in real-time video, as well as the region shown in (c-h). The contact area between the Li_xO and the carbon support film is designated by a closed curve with white dashed lines.

The yellow dashed arrow indicates the closest path for lithium ions to reach the nanowire. (c–h) Captured TEM images from the real-time video, which are listed in chronological order. Each figure was captured every second, from 12 s after -1 V biasing. The red arrowhead indicates the progress of contrast, which should be strongly linked to lithium-ion movement. The yellow solid arrow indicates the observed Li-ion diffusion path in the nanowires. (i, j) TEM images of nanowires (i) before and (j) after the reaction. The width of each nanowire before and after the reaction is indicated in the figures.

Figure 4.5 Schematic illustration of the lithium-ion diffusion in α - MnO_2 nanowires.

Figure 4.6 A representative example of the *in situ* lithiation in a single α - MnO_2 nanowire with the conventional end-point-contact method. (a) A low-magnification TEM image acquired after the *in-situ* lithiation. (b) Captured TEM images from the real-time video, listed in chronological order. (c) A FFT pattern of the HRTEM image obtained from the pristine nanowire shown in (a). (d) A HAADF-STEM image taken at $[111]$ zone axis of a potassium-doped α - MnO_2 nanowire. (e) Atomic structural model of ideal $\text{K}_2\text{Mn}_8\text{O}_{16}$ material at $[111]$ direction.

Figure 4.7 Experimental TEM-EELS spectra acquired during the *in situ* TEM measurement procedure. (a) A TEM image of the *in situ* lithiated nanowire reproduced from Figure 4.6a. (b, c) EELS spectra of (b) manganese M- and lithium K-, and (c) oxygen K- and manganese L-edges obtained after *in situ* lithiation. The numbers on each spectrum indicate the regions where the spectra were taken, which correspond to the numbers shown in (a).

Figure 4.8 The changes of FFT patterns implying the gradual structural deformation depending on the lithiation level. The FFT patterns were obtained from several continuous HRTEM images of the *in situ* lithiated nanowire shown in Figure 4.6. The FFT pattern collected regions are written below the patterns with the corresponding numbers indicated in Figure 4.7a. The FFT patterns show the gradual structure transformation from (a) the state with almost no lithium ions to (f) the state with high lithium-content.

Figure 4.9 A SAED pattern obtained near Point 3 indicated in Figure 4.7a, which shows the formation of MnO and Li₂O phase.

Figure 4.10 MnO phase appearance on an *in situ* lithiated nanowire. (a) A TEM image of the *in situ* lithiated nanowire. (b) The experimental and (c) the simulated SAED pattern obtained from the pristine nanowire shown in (a). (d) The experimental SAED pattern acquired after the *in situ* lithiation. (e) The SAED pattern corresponding to (d) overlaid with the simulated MnO phase at [11x] zone axes. (f) Radial intensity profile of the SAED pattern in (d). (g) Atomic structural models and the simulated electron diffraction patterns of MnO phase at [11x] zone axes.

Figure 4.11 Schematic illustration of the crystal structural correlation between the appeared MnO phase and the lithiated α -MnO₂ phase of the nanowire.

Figure 4.12 TEM-EELS spectra array collected from several *in situ* lithiated nanowires. (a) Mn M- and Li K-edges, and (b) O K- and Mn L-edges of the TEM-EELS spectra obtained during the *in situ* TEM experiment from the several α -MnO₂ nanowires, which are arranged in order of lithiation levels. The lithiation levels were estimated based on both of the manganese L₃/L₂ intensity ratio and the spectra evolution trend. (c) Estimated lithium amount per unit structure, K_{0.8}Mn₈O₁₆. The lithium amounts were calculated on the basis of the experimental fingerprint shown in Figure 4.13.

Figure 4.13 Manganese L₃/L₂ intensity ratio variation on lithiation levels in potassium α -MnO₂ nanowires calculated from TEM-EELS experimental data. Nanowire samples with Li⁺ content of 0 (pristine), 2, 4, 6, and 8 in K_{0.8}Mn₈O₁₆ were prepared by electrochemical lithiation in half-cell batteries. The TEM-EELS data was taken with over 20 points in each sample, and each point contains several nanowires. The calculated Mn L₃/L₂ intensity ratios from each EELS spectrum are indicated with black dots on the graph. The average values of the Mn L₃/L₂ intensity ratios and the standard deviation are indicated with red column/bars. The polynomial fit curve is drawn with a solid line.

Figure 4.14 Another example of MnO phase formation during the lithiation into the α -

MnO₂ nanowire. (a) A TEM image of the *in situ* lithiated nanowire. (b) The experimental and (c) the simulated SAED pattern obtained from the pristine nanowire shown in (a), which is aligned at [133] zone axis. (d, e) The SAED pattern acquired near the (d) volume expansion front and (e) the endpoint of the *in situ* lithiated nanowire. (f) Radial intensity profile of the SAED pattern shown in (e) (lower), comparing with the radial intensity profile of Figure 4.10f (upper). Each intensity profile is indicated with the corresponding EELS spectrum number of Figure 4.12. Spectrum 6 and 4 acquired regions correspond to the circled areas shown in Figure 4.10a and Figure 4.14a, respectively.

Figure 4.15 (a, b) The simulated electron diffraction patterns of MnO phase developed from the α -MnO₂ nanowire at (a) [130] and (b) [133] zone axes. (c) The SAED pattern shown in Figure 4.14e overlaid with the simulated EDP in (b). (d) Atomic structural models show the 3-D spatial orientation relationship between [100] and [133] directions of the α -MnO₂ nanowire.

Figure 4.16 The simulated electron diffraction patterns of MnO phase developed during the lithiation from the α -MnO₂ nanowire oriented along [100], [133], [113] projecting directions.

Figure 4.17 Three-dimensional spatial orientation relationship among atomic structural models of MnO phases showing the origins of the diffraction peaks from (11-1), (00-2), (220), (-11-1), and (1-1-1) planes observed at α -MnO₂ [133] projection.

Figure 4.18 Three-dimensional spatial orientation relationship among atomic structural models of MnO phases showing the origins of the diffraction peaks from (020), (200), (02-2), and (20-2) planes observed at α -MnO₂ [133] projection.

Figure 4.19 Three-dimensional spatial orientation relationship among atomic structural models of MnO phases showing the origins of the diffraction peaks from (-13-1), (3-1-1), (-11-3), and (1-1-3) planes observed at α -MnO₂ [133] projection.

Figure 4.20 (a) A SAED pattern obtained at Point 1 from the *in situ* lithiated nanowire

shown in Figure 4.7a, which was originally oriented along the $\alpha\text{-MnO}_2$ [111]. (b) Radial intensity profile of the SAED pattern in (a). The d-spacings in the SAED patterns match well with the cubic Li_2O phase.

Figure 4.21 (a, b) The simulated electron diffraction patterns of Li_2O phase developed from the $\alpha\text{-MnO}_2$ nanowire at (a) [110] and (b) [111] projections. (c) The overlapped electron diffraction patterns shown in (a) and (b). (c) The SAED pattern shown in Figure 4.20a overlaid with the simulated EDP in (b). (d) Atomic structural models describe the origins of the diffraction peaks from Li_2O [11x] projection directions shown in (a).

Figure 4.22 Schematic illustration of the crystal structural correlation between the appeared Li_2O phase and the ideally full-lithiated $\alpha\text{-MnO}_2$ nanowire.

Figure 4.23 (a) Elongation of the nanowire after *in situ* lithiation in the TEM instrument. (b) Increment of c-lattice parameter estimated by the interpretation of the SAED pattern, which may correspond to the stretched length of the nanowire.

Figure 4.24 Schematic illustration of 32 tetrahedral sites in the $\alpha\text{-MnO}_2$ tunnel structure, which may be the ideal positions for lithium ions after the full lithiation of the $\alpha\text{-MnO}_2$ materials.

Chapter 1

General introduction

1.1. Thesis overview

Having high energy densities, lithium ion rechargeable batteries are widely used for portable electronic devices, and they are still the subject of intensive investigation because of the possibility on a wide range of future applications including battery-only electric vehicles. To identify the electrochemical reaction mechanisms of lithium-ion battery electrode materials and suggest the appropriate directions for the improvement of the performance, there have been numerous researches using various analysis methods. In particular, there have been many tries to reveal the reaction mechanism by the crystal structural analysis, such as x-ray diffraction (XRD), x-ray absorption spectra (XAS), nuclear magnetic resonance (NMR), and so on.[1-3] However, those analyses are limited on the bulk and statistical analysis. They are impossible to perceive the accurate particles or regions where the experimental result data acquired.

Transmission electron microscopy (TEM), facilitating the structural and chemical analyses at the nanoscale, is one of the most powerful analysis techniques. Using the high energy electron beam, it is possible to perform the various structural analysis while

Chapter 1. General introduction

directly observing the interested nano-area. It even shows the images of the materials at atomic levels. Accordingly, there have been diverse TEM researches to explain the electrochemical reaction mechanisms.[4-6] The structural transformation of electrode materials was visualized at atomic scale and the chemical states changes after electrochemical cycles were identified. Moreover, the structural evolution derived from the lithium insertion was observed in real-time by *in situ* TEM experiment. However, there were also several weaknesses on the previous TEM investigations of the battery electrode materials. First, most of the TEM observations were limited to the surface of a few nano-particles, which can lead to the mistake of hasty generalization on the conclusion drawn from the experimental results. In addition, the phase and structural evolution of the electrode materials during the electrochemical cycles were interpreted from the different samples. It can also mislead about the interpretation when the structural evolution was observed only at nano-scale because the pristine state of the observed particles was not guaranteed. Also, it has been controversial if the *in situ* TEM experimental results can be applied to the real environment because of the special configuration of the *in situ* TEM experiment.

Here, we show the improved TEM experimental techniques for the investigation of the lithium-ion battery electrode materials. By developing the TEM experimental methods elaborately, the inside of a micro-sized secondary particle was directly observed instead of the surface of the particles. Also, we developed the *ex situ* TEM technique that can track the same particles during the whole electrochemical cycles. We also improved the *in situ* TEM investigation technique to identify the actual lithium-ion diffusion paths in the electrode material, which has hardly been seriously considered.

Chapter 1. General introduction

We applied the improved TEM experimental techniques to the proper issues on the electrochemical reaction mechanisms of lithium-ion battery electrode materials. First, we directly observed and compared the structural degradation of lithium nickel cobalt manganese oxide (NCM) cathode materials with different Ni-content to reveal the origin of the worse cycle performance in the Ni-rich NCM cathode. By direct comparison on the inside of the secondary particles after prolonged electrochemical cycles, which was achieved by focused-ion beam TEM sampling technique, we clearly visualized the severe surface degradation on the Ni-rich cathode material compared to the conventional NCM 1/1/1 material. This experimental results suggest that the surface treatment of Ni-rich NCM cathode material would be beneficial for the better cycle performance.

In addition, we revealed the possibility of reverse conversion reaction and the origin of the additional capacity of SnO₂ anode material by tracing the phase evolution of the same particles during the first full cycle through the *ex situ* TEM experiment, which has long been controversial. We (dis)charged the SnO₂ particles directly on the copper TEM grid in a coin-type battery cell, which were placed together with the conventional SnO₂ slurry electrode. The direct (dis)charging on the copper TEM grid enabled us to observe the same SnO₂ particles at several (dis)charged states. Combining with the electron diffraction and electron energy loss spectroscopy (EELS) studies in TEM, we could reveal that the a few reversed SnO phase can be developed, but it does not mainly contribute to the additional capacity of the SnO₂ anode. Instead, the lithium-ion extraction from Li₂O phase would greatly contribute to the extra capacity. By the elaborate *ex situ* TEM investigation, this research extends the fundamental knowledge on the reaction mechanism of SnO₂ anode material.

Chapter 1. General introduction

Finally, we identified the detailed lithiation mechanism of tunnel-structured α -MnO₂ nanowire electrode material by the *in situ* TEM investigation, which reflected the real battery environment. The unique [2×2] tunnels in the α -MnO₂ nanowire are considered to be effective for the facile lithium-ion diffusion, but it has not been clearly proved. In this study, we set up the special configuration for comparing the lithium-ion movement through the tunnels and the side wall of the nanowire. It facilitated revealing the most favorable lithium-ion diffusion paths of the tunnel-structured nanowire, which turned out that the lithium-ion movement through the tunnels are the most preferred paths even under the actual electrolyte-covering conditions. Furthermore, we could describe how the lithiation into the α -MnO₂ nanowire leads to the phase evolution by the combination of electron diffraction, high-resolution TEM, TEM-EELS results obtained during the *in situ* TEM investigation. The development of MnO intermediate phase and the 3-D structural correlation between the original α -MnO₂ structure and MnO/Li₂O phase were clearly identified. The comprehensive *in situ* TEM studies provide the important information on the reaction mechanism of the tunnel-structured material.

In the next two sections, we will provide brief introduction on the lithium-ion battery and TEM analysis techniques for the lithium-ion battery electrode materials, which would be helpful for understanding this thesis. From the following chapters, we elucidate the detailed studies mentioned above. We expect that this thesis extends the fundamental and important knowledge on the electrochemical reaction mechanisms of the lithium-ion battery electrode materials, and provides the useful TEM experimental techniques widely applicable to the battery field, as well.

1.2. Lithium-ion battery

1.2.1. Principles of lithium-ion battery

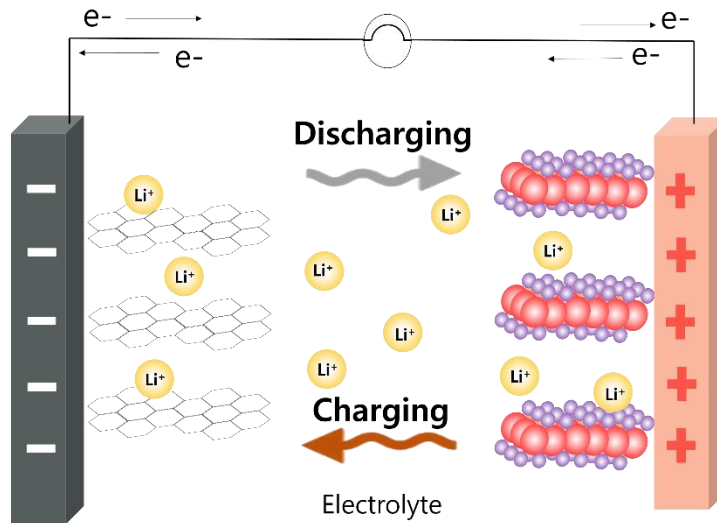


Figure 1.1. Schematic illustration of lithium-ion battery working principles.

Lithium-ion battery is a type of secondary battery, i.e. rechargeable battery, which is an electrical energy storage with high energy density. Due to their extremely high energy density, lithium-ion batteries are widely used for portable electronic devices, such as laptop computers, smartphones, electric vehicles, and so on. Lithium-ion battery is operated by the lithium-ion movement between the negative and positive electrodes inducing the electrochemical reactions in the electrode materials, which converts the electrical energy into the chemical energy and vice versa for the electrical energy storage and usage, respectively. The schematic illustration of the lithium-ion battery working principle is shown in Figure 1.1.

Chapter 1. General introduction

A lithium-ion battery cell is composed of positive electrode (cathode), negative electrode (anode), electrolyte, and separator. Lithium ions move toward the negative or the positive electrode through the electrolyte (generally with liquid phase) and electrons are also transferred toward the same electrode with lithium ions through external circuit. Electrons should not be transferred through the electrolytes not to cause a short circuit. For this reason, the electrolyte materials must be ionic conductor, but electronic insulator. Additionally, the separator is laid between the negative and positive electrodes, which also protects from the short circuit by physically separating the two electrodes.

The negative and the positive electrodes are directly related to the electrochemical reaction, which operates the lithium-ion batteries. When lithium ions are transferred into the electrode material, electrons are also transferred into the electrode material through the external circuit at the same time, which leads to the electrochemical reaction of the electrode material and the energy conversion between the electrical and the chemical energies. During the electrochemical reaction in the lithium-ion battery, it is generally known that oxidation or reduction occurs in the host material instead of the lithium ions. The solid state materials that are able to accept lithium ions can be either of cathode or anode materials depending on the relative lithium stability in the host material, i.e. lithium chemical potential. When two electrode materials are set up in the lithium-ion battery, the one in which lithium ions settle down more stable (lower chemical potential of lithium) is classified as the cathode material.

Discharging occurs by the spontaneous movement of lithium ions in the closed circuit from anode (higher Li chemical potential) to cathode (lower Li chemical potential), which is driven by Li chemical potential gradient between two electrodes. The stored

Chapter 1. General introduction

electrical energy from anode is used for the operation of electronic devices during the discharge procedure. On the contrary, charging process can occur by the external electric force that compels the electrons to move toward the anode side, which causes the lithium insertion into the anode and the electrical energy storage of the lithium-ion battery.

The energy density (volumetric or gravimetric) of lithium-ion battery is determined by the combination of the cell voltage and the specific (or volumetric) capacity. The cell voltage can be roughly calculated by the average potential difference between the anode and cathode. The specific (or volumetric) capacity indicates the available charge amount per unit weight (or volume). In general, the high specific capacity greatly contributes to the high energy density of lithium-ion batteries. The theoretical specific capacity of electrode materials can be simply calculated by the equation written below.

$$C_T = nF/w \quad (1.2.1)$$

C_T , n , F , and w indicate the theoretical specific capacity, mol number of electrons participating the electrochemical reaction, Faraday constant ($96,485 \text{ C/mol} = 26,801 \text{ mAh/mol}$), and molar weight of the material, respectively. The conventional cathode and anode materials, lithium cobalt oxide (LiCoO_2) and graphite (C_6), show the specific capacity of $\sim 135 \text{ mAh/g}$ and $\sim 370 \text{ mAh/g}$ in the practical voltage range; they result in the specific energy density of 140 Wh/kg , which is much higher than the previous Ni-MH battery, 75 Wh/kg .

1.2.2. Insertion reaction for cathode materials

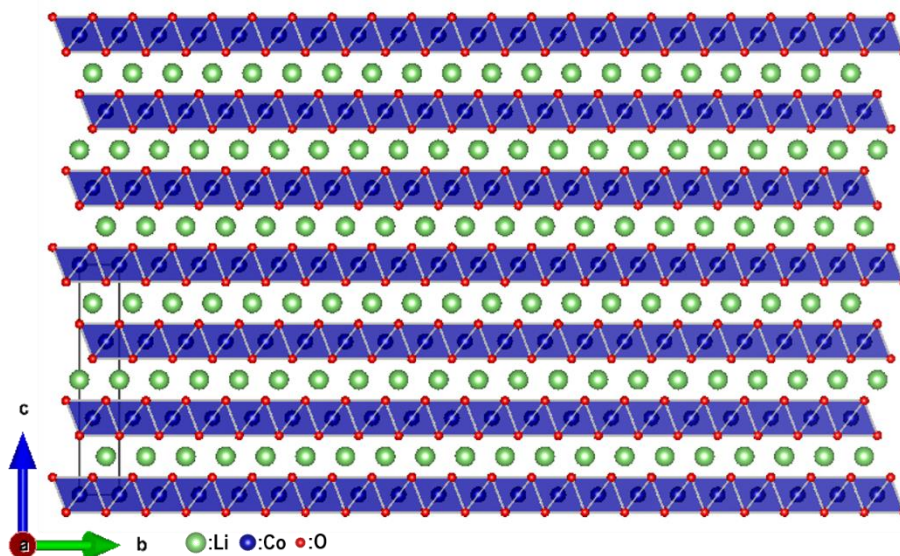


Figure 1.2. Atomic structural model of LiCoO₂ cathode material.

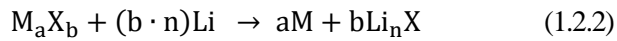
The widely commercialized cathode material, lithium cobalt oxide (LiCoO₂, LCO), is composed of the repetitive alternate layers of lithium and cobalt ions as shown in Figure 1.2. Due to the two-dimensional lithium layers, the movement of lithium ions is not impeded during lithium insertion (lithiation) and extraction (delithiation), which, therefore, can occur very quickly. Including the case of the above material, the reaction that lithium ions are inserted into the interstitial sites of the open crystal structured host materials is called insertion reaction. Because the crystal structure is not much changed during the insertion reaction, it has a great advantage of reversible reaction, which directly correlates with the cycle performance of the electrode materials. The widely used anode material, graphite (C₆), is also operated by the insertion reaction mechanism in the lithium-ion battery.

Chapter 1. General introduction

In addition to the conventional LCO and graphite materials, various materials reacting with lithium ions by the insertion reactions have been suggested as the promising candidates for the next-generation lithium-ion battery electrode materials. In particular, various cathode materials have been proposed to improve the performance of the current LCO cathode material. For example, lithium iron phosphate (LiFePO_4 , LFP), lithium nickel cobalt aluminum oxide ($\text{Li}(\text{Ni}_x\text{Co}_y\text{Al}_{1-x-y})\text{O}_2$, NCA), and lithium nickel cobalt manganese oxide ($\text{Li}(\text{Ni}_x\text{Co}_y\text{Mn}_{1-x-y})\text{O}_2$, NCM) are considered as very attractive cathode candidates. LFP material has one-dimensional tunnels for lithium ions, which leads to the insertion reaction with lithium ions through these tunnels. LFP cathode has slightly lower energy density than the conventional LCO cathode material, but it has advantages of the cycle performance and the rate capability. In addition, LFP is cheap, environmentally friendly, and safe. On the other hand, nickel-based materials, e.g. NCA and NCM materials, are used to increase the energy density by the higher specific capacity. NCM and NCA materials have same crystal structure with LCO material, $\alpha\text{-NaFeO}_2$ structure, but they have the substituted form of cobalt ions from LCO into the mixture of Ni/Co/Mn or Ni/Co/Al. In the common voltage range of lithium-ion battery cathode, the oxidation state of nickel ions varies from 2+ to 4+, while cobalt ions change between 3+ and 4+; it results in the doubled specific capacity of Ni-based cathode material, theoretically. Based on this principle, there have been various tries to contain as much as nickel ions in the material, but the worse cycle performance with the higher Ni-content makes it difficult to be realized.

1.2.3. Conversion reaction for anode materials

The conventional graphite anode material is operated by the insertion reaction mechanism, but most of the insertion reaction materials have the limitation on the low specific capacity. However, the introduction of conversion reaction materials aroused a leap in the capacity of the lithium-ion battery anode materials. The conversion reaction is described as the equation below.



As shown in the equation, the original material is totally changed after the conversion reaction. The conversion reaction electrode material is first developed by Fuji.[7] They introduced tin-based amorphous composite oxide (SnM_xO_y) for the lithium-ion battery anode and it showed the reversible specific capacity over 600 mAh/g, which is nearly twice value of the graphite, ~370 mAh/g. After the introduction of tin-based composite oxide material, various conversion reaction materials have been investigated for the future generation lithium-ion battery electrode materials. Because the conversion reaction generally occurs at the voltage lower than 1 V (vs. Li/Li^+), most of the conversion reaction materials have been suggested as the anode materials. Transition metal oxide materials have been widely examined for the anode, e.g. NiO, CoO, MnO, Fe_2O_3 , MoO_3 , RuO_2 , and so on. The specific capacities of these materials even reach ~1000 mAh/g. In addition to the metal oxide materials, metal fluorides, metal sulfides, metal nitrides, and metal phosphides can be the lithium-ion battery electrode materials (mostly anode materials) with high specific capacities through the conversion reaction mechanism.

However, most of the conversion reaction materials show poor cycle performance. Due to the severe structural transformation during the lithiation procedure, the full reverse reaction is difficult to be achieved. Accordingly, there still have been numerous approaches to improve cycle performance of conversion reaction materials. For example, surface coating and downsizing of the materials have been proved to be effective for the better coulombic efficiency. Even though the recently developed alloying reaction electrode materials show much higher specific capacity, e.g. ~4000 mAh/g in silicon, the conversion reaction materials continuously have been studied due to their high performance in the next-generation sodium-ion battery.

1.3. Transmission electron microscopic approaches on the analysis of lithium-ion battery

Transmission electron microscopy (TEM) is a microscopy technique, which visualizes the interaction of high-energy electrons and solid-state materials by transmitting the high-energy electron beam (mostly, 60–300 keV) through the ultrathin specimen under high vacuum condition. Having sub-angstrom spatial resolution, it basically enables the direct observation of the solid-state material at micro- to atomic-scale, which therefore can be simply used for the investigation on the morphology of nano-materials or defects in the materials. Besides, with the elaborate interpretation of electron diffraction patterns or electron energy loss spectra that can be obtained by TEM, it is able to identify the detailed crystal and electronic structure of the material at the interested nano-area. Accordingly, TEM is the robust analytical technique for the

investigation on physical and chemical properties of nano-sized materials including the lithium-ion battery electrode materials, which are generally composed of the nano-sized particles for the better performance. Numerous electrochemical reaction mechanisms of various lithium-ion battery electrode candidate materials have been identified by the aid of TEM studies.[6, 8, 9] Because it is even possible to directly observe the lithium-ion insertion/extraction procedure into the electrode materials at nano-scale by using the special TEM experimental technique, which is called *in situ* TEM measurement, TEM investigation has become one of the most important approaches on the lithium-ion battery analyses. In this section, basic principles of fundamental TEM experimental techniques will be explained, which have been extensively utilized for our researches.

1.3.1. Electron diffraction

Electron diffraction is a basic, but powerful analysis technique of TEM. When the high energy electron parallel beam passes through the specimen in TEM with a few picometer-sized wavelength, the electron waves are scattered by atoms of the specimen material. In particular, the interference of the elastically scattered electron waves is called electron diffraction. In TEM, the diffracted electrons make specific patterns as a series of spots, determined by the crystal structure of the specimen, at the back focal plane of the objective lenses. The electron diffraction pattern obtained from the particular region of the real-space chosen by a selected area aperture is named selected area electron diffraction (SAED) pattern, which can acquire the spot patterns from the a few hundreds of nanometer-sized real space area depending on the size of the selected area aperture.

Chapter 1. General introduction

By interpretation of the electron diffraction patterns, the crystal structural information of the specimen can be identified. It is because each spot in the electron diffraction pattern has originated from the specific lattice planes satisfying Bragg's law.

Bragg's law describes the specific conditions for the constructive interference of the scattered waves. It explains that two scattered waves from the lattice planes separated by interplanar spacing d can interfere constructively only when the path difference between the two scattered waves is equal to an integer multiple of the wavelength, which is described in Figure 1.3 and Equation 1.3.1 below.

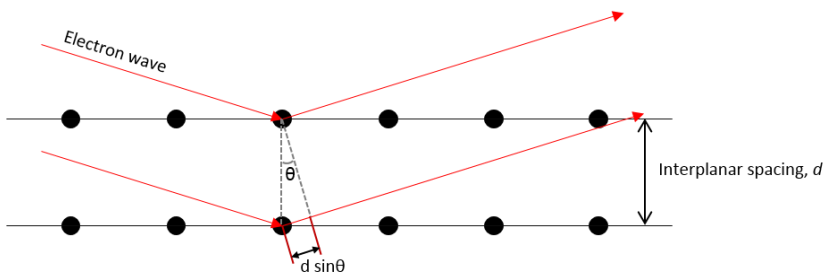


Figure 1.3. Schematic illustration of Bragg condition.

$$n\lambda = 2d\sin\theta \quad (1.3.1)$$

where n and λ indicate a positive integer and the wavelength of the incident wave, respectively.

While the position of diffracted plane is determined by Bragg's law, the amplitude of scattered atomic planes (hkl) is determined by structure factor, F_{hkl} , in the electron diffraction pattern. Structure factor describes how the incident beam is scattered by the material, which is defined as the sum of atomic-scattering factors multiplied by a phase factor from all atoms in the unit cell. The structure factor of (hkl) planes can be written

as Equation 1.3.2 below.

$$F_{hkl} = \sum_j^{\infty} f_j e^{2\pi i(hx_j + ky_j + lz_j)} \quad (1.3.2)$$

where f_j and (x_j, y_j, z_j) indicate the atomic scattering factor and the atomic coordinates of the j^{th} atom. By putting (hkl) plane in the equation, the structure factor of (hkl) planes from the crystal structure of the interested material can be obtained. The scattered intensity from (hkl) planes can be calculated by the square of the absolute value of the structure factor, $|F_{hkl}|^2$. According to the equation, the scattered intensities vary in the crystal structure as well as the elements of the material. Therefore, it leads to the formation of different electron diffraction patterns depending on the atomic structure, which enables to identify the crystal structure of the specimen from its electron diffraction pattern.

1.3.2. Atomic-resolution HAADF/ABF-STEM imaging

Scanning transmission electron microscopy (STEM) is a different mode of conventional TEM operation, which uses the convergent electron beam, instead of the parallel electron beam in the conventional TEM mode, making a tiny spot probe for scanning over the sample. The STEM was first designed and constructed by Manfred von Ardenne in 1937-1938. His motivation for the STEM development was to make a high-resolution image not degraded by chromatic aberration of the imaging lenses.[10] It was not successful at that time, but the development of cold field emission gun and the high quality objective lenses finally brought success to visualize single heavy atoms by Crewe *et al.*[11] In addition, the introduction of aberration-corrected STEM enabled to

Chapter 1. General introduction

realize the extremely high spatial resolution smaller than 2 angstrom probe in the late 1990s. The up-to-date aberration-corrected STEM even provides sub-angstrom spatial resolution.

STEM images are formed by counting the number of the scattered electrons that reach the STEM detectors. The larger number of the collected electrons results in the brighter intensity at this point. Two kinds of detectors are typically used for the STEM imaging: annular dark-field (ADF) and bright field (BF) detectors. The STEM-ADF detector is ring or donut-shaped around the transmitted electron beam, which collects electrons scattered between the specific ranges of the collection angle that are determined by the camera length. When the image is obtained from the STEM-ADF detector with the very large collection angles, e.g. typically the inner collection angle larger than 50 mrad and over twice the convergence angle, it is called high-angle annular dark-field (HAADF) or Z-contrast STEM image. The term, Z-contrast image, has originated from its nature, the intensity of which depends on the atomic number (Z) of the sample with the $Z^{1.7-2}$ dependence due to Rutherford and thermal scattering feature of the scattered electrons with large angles.[12] On the other hand, the STEM-BF detector is filled circle-shaped around the electron center beam, which collects both of the scattered and transmitted electrons in a small collection angle. However, when a small disk blocks the center of the BF detector, the ring-shaped detector is produced, the image obtained from which is called annular bright field (ABF) image. By increasing Scherzer resolution of contrast transfer function with the annular-shaped low angle detector, ABF-STEM image can visualize both of the light and heavy elements, even lithium atoms.[13] Thus, the HAADF- and ABF-STEM imaging techniques are powerful for the direct observation

of lithium-ion battery electrode materials, which can visualize the position of lithium ions as well as heavy elements at atomic scale.

1.3.3. Electron energy loss spectroscopy

Electron energy loss spectroscopy (EELS) is a chemical analysis technique that uses inelastically scattered incident electrons by the interaction with the specimen materials. When the high energy electron beam is scattered by the specimen, some electrons lose their energy because of phonon excitations, plasmon excitations, inter- and intra-band transitions, inner shell ionizations, and Cherenkov radiation. The spectrometer collects these inelastically scattered electrons as a function of the energy loss and spread it as a spectrum. In particular, the electron energy loss by the inner shell ionization, i.e. core-loss EELS, is useful for the identification of the chemical states of each element in the specimen. The inner shell ionization indicates the transition of electrons at core levels to empty states above the Fermi level of the material. Because the energy loss levels are mostly determined by the characteristic energy levels of each element, the existence of specific element in the specimen can be simply recognized by the acquisition of core-loss EELS near the well-known energy loss levels of the interested element. Furthermore, the chemical state variation of the element can be predicted by the slight change of the electron energy loss, and the atomic and electronic structures are even able to be identified by the precise interpretation of the core-loss EELS fine shape.[14]

For the lithium-ion battery analysis, EELS studies are widely used for the identification of existence of specific element, the prediction of the crystal structure, the

Chapter 1. General introduction

estimation on the oxidation state of the transition metal ions, and so on. In particular, the oxidation state of the transition metal ions is typically estimated by the interpretation of the experimental EELS data in various ways. Typically, the L_3/L_2 -edge intensity ratio, the absolute energy shift of the core edge, the energy difference between metal L_2 - and L_3 -edges, the energy difference between the metal L_3 -edge and O K-pre-edge, and O K-pre-edge splitting have been used for the valence state estimation of transition metal elements. Unfortunately, there is no well-established method that can perfectly determine the valence state of transition metal ions from an electron energy loss spectrum due to its sensitivity to atomic structural arrangements in addition to the valence state. Nevertheless, use of the L_3/L_2 -edge intensity ratio is the generally accepted method for estimating the chemical valence state of transition metals. The L_3 and L_2 -edges imply the transition of electrons from $2p_{3/2}$ and $2p_{1/2}$ levels to the conduction band, mostly to the unoccupied $3d$ states due to the selection rule. In principle, the L_3/L_2 intensity ratio should be 2:1 based on the quantized number ratio of total angular momentum of $2p_{3/2}$ and $2p_{1/2}$ levels in a one-electron model. However, it has been observed that the L_3/L_2 -edge intensity ratio shows negative correlation with d -state occupancy for most of the $3d$ and $4d$ transition metals. In spite of many efforts based on one-electron approximation or band-structure studies, the origin of this anomalous relationship has not been clearly understood.[15] Though, it has been verified empirically that the L_3/L_2 -edge intensity ratio reflects the d -state occupancy of most of transition metal elements quite well in comparison with other interpretation methods, and therefore, it is widely utilized for the analysis of the oxidation states of transition metal elements included in the interested materials.

1.3.4. *In situ* I-V TEM measurement

In situ I-V (current-voltage) TEM measurement is an advanced TEM experimental technique that enables the direct observation on the changes of materials induced by the electrical stimulus applied in the TEM instrument. The *in situ* TEM experiment can be performed with the specialized TEM holder and the electric signal generator that can provide the electric current or voltage to the material. A photo of the *in situ* TEM holder, produced by Nanofactory, is shown in Figure 1.4. A tip stuck into the hat can be moved by piezoelectric actuator. Therefore, the sharp tip can be directly connected to the area of interest in the TEM specimen, and electrical bias can be then applied to the closed circuit formed between the tip and the specimen.



Figure 1.4. A photo of the *in situ* I-V TEM holder produced by Nanofactory.

By Huang *et al.*, the *in situ* TEM experimental technique was first applied to the lithium-ion battery.[16] They directly observed the lithiation into a single SnO₂ nanowire

Chapter 1. General introduction

by the *in situ* TEM technique. The *in situ* TEM experimental configuration for the investigation on the lithiation of lithium-ion battery electrode materials developed by Huang *et al.* is drawn in Figure 1.5.[16, 17] Lithium metal is coated onto a sharp metal tip as the counter electrode and the nanowire electrode material is attached to the other side. A thin layer of lithium oxide solid electrolyte is naturally formed on the lithium metal upon short-time air exposure during the transfer of the holder into the TEM column. After moving the lithium oxide coated lithium tip to make contact with the endpoint of the nanowire sample in the TEM instrument, voltage bias is applied to induce lithiation into the nanowire electrode. It has been controversial among some researchers if the *in situ* TEM experimental results can be applied to the actual battery environment, but this conventional *in situ* experimental method is still widely used for the investigation on the dynamics of reaction in the lithium-ion battery electrode materials.

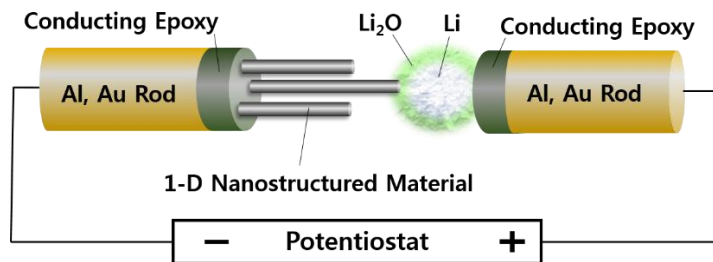


Figure 1.5. Schematic illustration of the *in situ* TEM experimental configuration for lithium-ion battery.

Chapter 2

Visualization on degradation of Ni-rich Ni/Co/Mn cathode material

2.1. Introduction

In spite of the successful commercialization of LiCoO_2 (LCO) cathode material, it requires improved cathode materials having higher capacity due to the development of electronic technology. Ni/Co/Mn-based layered oxide (NCM) material is one of the most promising materials for the future generation cathode material, which has higher capacity than the conventional LCO cathode.[18] NCM cathode material is known to have the same crystal structure with LCO cathode material, $\alpha\text{-NaFeO}_2$ structure with space group R-3m (No. 166), but cobalt atoms are replaced by nickel, cobalt, and manganese atoms randomly, the chemical formula of which is written as $\text{Li}(\text{Ni}_x\text{Co}_y\text{Mn}_{1-x-y})\text{O}_2$, accordingly. Having two-dimensional layers of lithium ions, this layered structure has a great advantage of facile lithium-ion insertion/extraction with structural stability, which therefore has excellent cycle performance during prolonged cycles.[19] The atomic model structure of NCM material is shown in Figure 2.1.

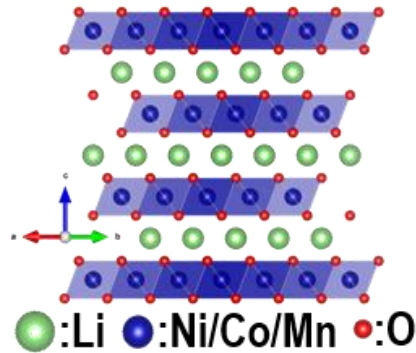


Figure 2.1. Atomic model structure of NCM cathode material in [110] zone axis.

Despite the same crystal structure with LCO cathode, NCM cathode shows better performance contributed to the advantages of nickel, manganese elements. While it requires high voltage to change the oxidation state of cobalt ions from 3^+ and 4^+ during electrochemical cycles in the lithium-ion battery, nickel ions can vary between 2^+ to 4^+ in the lower voltage range, which can contribute to higher capacity.[20] Even though manganese ions are considered to be inactive during the cycles, it is known that the MnO_6 octahedra with Mn^{4+} oxidation states have the exceptional high stability, which provides the great structural stability of the parent structure during the repeated cycles. Also, the low cost and the environmental friendliness of manganese element makes it attractive to contain more in the material.[21] In addition, it is believed that cobalt ions improve the rate capability of the material.

Taking those great advantages of Ni/Co/Mn elements, NCM cathode material with 1:1:1 (111) composition ratio of Ni/Co/Mn elements is close to the commercialization, but the NCM cathode material with higher Ni concentration, such as 6:2:2 (622) or 8:1:1 (811) composition ratio, has been continuously demanded for much higher capacity. As

Chapter 2. Visualization on degradation of Ni-rich Ni/Co/Mn cathode material

explained above, the higher Ni-content produces the greater specific capacity as shown in Figure 2.2a.

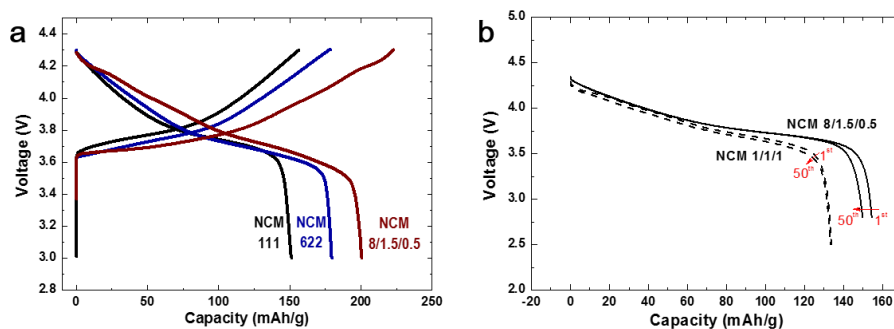


Figure 2.2. Voltage vs. capacity profiles of NCM cathode materials with different composition ratios. (a) Charge/Discharge curves at the first cycle after the activation cycle. (b) Discharge curve at the first and the 50th cycle.

However, the NCM material with higher Ni-content shows the worse cycle performance, which is clearly shown in Figure 2.2b. Ni-rich NCM (8/1.5/0.5) cathode shows faster capacity fading than NCM 111 cathode even under the narrower voltage range. To improve the cycle performance of NCM cathode, numerous fundamental studies approaching the origin of the degradation have been performed.[22-24] It is generally known that the NCM material undergoes the phase transformation into rocksalt phase at the surface of primary particles after the charge and discharge process, which is resulted from the mixing of Li, Ni, Co, Mn ions causing the cations indistinguishable, called the cation mixing phenomenon.[22] In addition, it was predicted by the calculation that the intrinsic instability of Ni-rich NCM cathode may result in the severe degradation.[25] As above, there has been great achievement in unraveling degradation mechanism of

Chapter 2. Visualization on degradation of Ni-rich Ni/Co/Mn cathode material

general NCM cathode materials, but the fast capacity fading of Ni-rich NCM material is not still clearly understood. In addition, most of the TEM observations limited to the very surface of micro-sized secondary particles hindered the full understanding of the overall degradation mechanism, and the grinding and destructive method for the TEM sampling makes it difficult to investigate the deteriorated material as it is. Those attribute to the rare studies on the direct observation and comparison between Ni-poor and Ni-rich NCM materials.

In this study, we focused on the fundamental understanding of structural evolution of NCM cathode materials from the micro-sized secondary particles to the nano-sized primary particles. Utilizing the focused-ion beam (FIB) technique, we directly observed and compared the structural changes of NCM 8/1.5/0.5 and 1/1/1 cathode materials as they were after 300 electrochemical cycles. The comprehensive electron microscopic studies led to suggest more important reasons of severe degradation on Ni-rich NCM cathode as well as new useful information on the structural evolution, which helps to draw a big picture on the electrochemical reaction mechanisms of NCM cathode material.

2.2. Structural characterization of pristine NCM cathode material

We first characterized NCM cathode material at wide range of scale, from micro-scale of secondary particles (cluster of primary particles) to atomic-scale of primary particles. The NCM materials were synthesized by co-precipitation method, provided by Samsung. A cross-sectional scanning electron microscopy (SEM) image of secondary

Chapter 2. Visualization on degradation of Ni-rich Ni/Co/Mn cathode material

particle is shown in Figure 2.3. As shown in the figure, the material is composed secondary particles with the diameter smaller than 10 μm , which is a cluster of densely packed primary particles with the diameter of a few hundred nanometers. It seems that each primary particle is single crystal and it is generally regarded as the single crystal, but our further analysis on the primary particles revealed that each primary particle is composed of a well-bonded poly-crystals as shown in Figure 2.4.

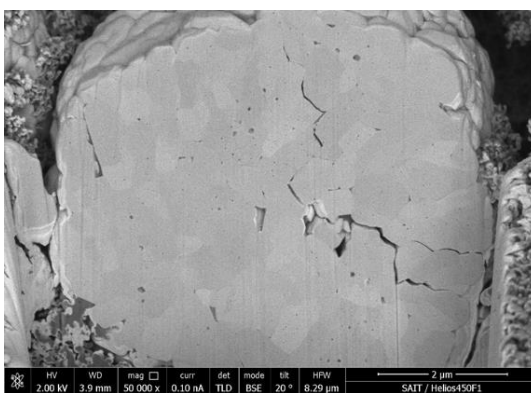


Figure 2.3. A cross-sectional SEM image of a secondary particle of NCM 111 cathode material.

Figure 2.4a shows a representative example of a primary particle from NCM 111 cathode material taken by ABF-STEM mode of TEM. The TEM sample was made by FIB technique, which etched the cross section of a secondary particle with the thickness narrower than 100 nm. As clearly shown in the figure, a single primary particle has several numbers of grain boundaries. In addition, there is contrast difference among several grains, which may have originated from the diffraction contrast. They imply that a primary particle is composed of several grains arrayed with different crystallographic orientations. Figure 2.4b shows that two nearby grains arrayed with slightly different

Chapter 2. Visualization on degradation of Ni-rich Ni/Co/Mn cathode material

orientations. The atomic-resolution HAADF-STEM image from the region indicated in Figure 2.4a is shown in the inset of Figure 2.4b. It seems that the two nearby grains have almost same orientation, but its FFT pattern reveals that there is a rotational orientation relationship of 2 degrees between the grains.

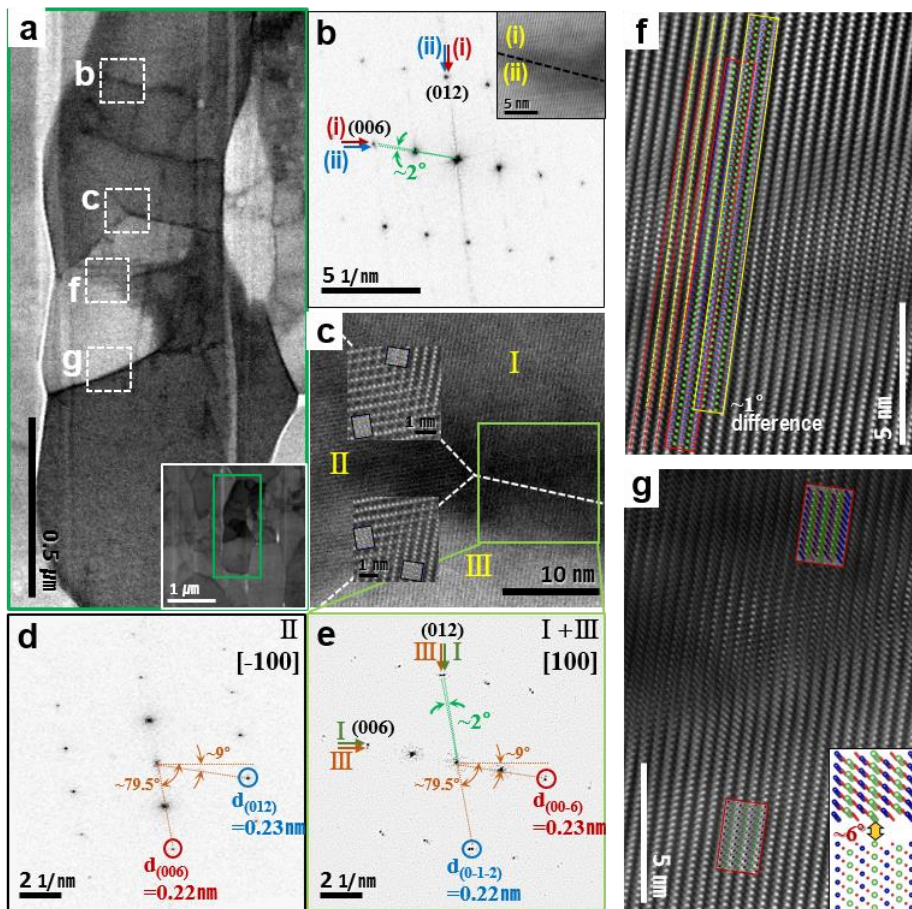


Figure 2.4. (a) A representative ABF-STEM image of a primary particle from NCM 111 cathode material. (b) FFT pattern from an atomic-resolution HAADF-STEM image at the region indicated in (a). (c, f, g) Atomic-resolution HAADF-STEM images of corresponding regions indicated in (a). (d, e) FFT pattern from the indicated regions in (c).

Chapter 2. Visualization on degradation of Ni-rich Ni/Co/Mn cathode material

There are separate (012) and (006) peaks observed in the FFT pattern, which implies that there is at least 2-degree tilt between the grains. It can have slightly more degree of misorientation away from this zone axis. Figure 2.4f and g also show other cases of low-angle grain boundaries in the same primary particle. The atomic-resolution HAADF-STEM images clearly show the misorientation between the nearby grains with the angle difference less than 10 degrees. In particular, the two overlapped grains with the slight in-plane rotational relationship along the same zone axis (Figure 2.4f) result in the appearance of moire fringes in the low-magnification ABF-STEM image (Figure 2.4a), which is difficult to be observed in HRTEM images due to the small angle difference between the overlapped grains. In the region shown in Figure 2.4c, a grain with the obviously different orientation was observed, indicated as II in the figure. In this figure, the grain II has the same zone axis family, $\langle 100 \rangle$, with all other grains in the same primary particle, but having the 180-degree flipped orientation, $[-100]$. Also, the grain II is rotated in-plane about 70 degrees, which fits well at the atomic view with the nearby grains at the grain boundaries forming defect spinel structure (MgAl_2O_4 structure), as clearly shown in the atomic-resolution HAADF-STEM image of Figure 2.4c. This special grain boundaries, leading to the formation of the distinct stable phase, would be exceptionally more stable than other kinds of grain boundaries with similar angle relationship. Interestingly, variation of interplanar spacing was also observed among those grains making special orientation relationship at the grain boundary (Figure 2.4c). Due to the crystallographic relationship, two grains share several diffraction peaks at the same position; the diffraction peaks from (012) planes in II and (00-6) planes in I+III, and the peaks from (006) planes in II and (0-1-2) planes in I+III. For the precise fit

Chapter 2. Visualization on degradation of Ni-rich Ni/Co/Mn cathode material

between two grains at the atomic scale, the sharing diffraction peaks have same interplanar spacing, which therefore results in the difference on the slab spacing. As shown in Figure 2.4d and e, the interplanar spacing of (006) planes in grain II, the spacing of the slabs, is 0.22 nm, while 0.23 nm in grain I and III, which shows ~5 % difference. It implies that the interplanar spacing or atomic spacing of NCM cathode material can be flexible to some extent depending on the orientation relationship of the nearby grains.

There are more examples of the primary particles composed of several grains with small angle difference. Figure 2.5 shows crystallographic orientation map of primary particles constructed based on scanning nanobeam electron diffraction patterns using ASTAR program (NanoMEGAS[26]). Disorientation relationship of grains in primary particles is shown in Figure 2.5d and h. Scan 1 in Figure 2.5a–c corresponds to the primary particle described in Figure 2.4. The slightly misorientated grains in the primary particle are also clearly detected by the ASTAR analysis. The misorientation angle curves (Figure 2.5d and h) obviously show that primary particles are mostly composed of several grains with low-angle grain boundaries.

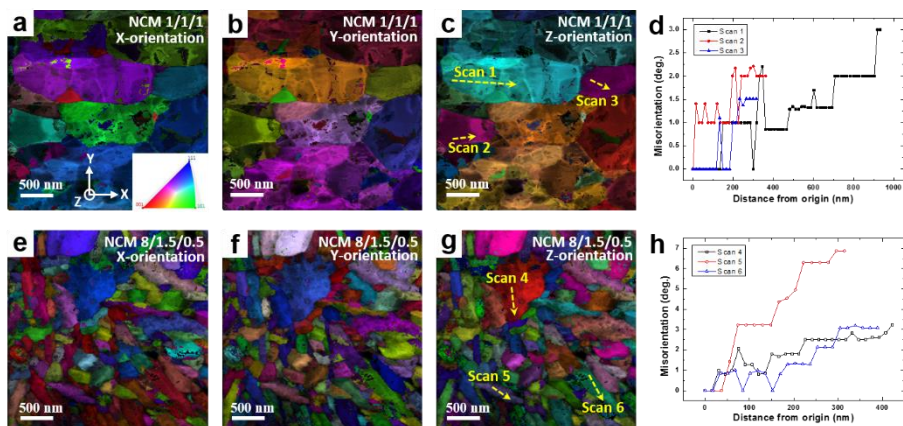


Figure 2.5. (a–c, e–g) Crystal orientation maps obtained from (a–c) NCM 1/1/1 and (e–g) 8/1.5/0.5 materials.

(d, h) Disorientation relationship of grains in primary particles

It seems that the grains with the low-angle grain boundaries can bond strongly due to the low energy of the low-angle grain boundaries, which results in the formation of the poly-crystalline primary particles that are likely to be misinterpreted as a single crystal. These results confirm that most of the primary particles in a secondary particle of NCM material consist of several grains with low-angle grain boundaries, which is difficult to be observed by high-resolution TEM (HRTEM) images or selected area electron diffraction (SAED) patterns that have worse spatial resolution than atomic-resolution HAADF- and ABF-STEM images.

We further observed the pristine NCM cathode material with atomic-resolution HAADF- and ABF-STEM images, and confirmed its α - NaFeO_2 structure (space group R-3m) as shown in Figure 2.6. The HAADF-STEM image (Figure 2.6a) clearly shows the layers of transition metal atoms and the oxygen atoms with weak intensities are also distinguishable. The absence of intensity at the middle of the transition metal layers in the HAADF-STEM image implies that there is almost no invasion of transition metal

atoms into the lithium layers at its pristine state. The ABF-STEM image (Figure 2.6b) obviously shows the lithium atoms at the middle of the transition metal layers where nothing was detected in the HAADF-STEM image. The atomic structure model of α -NaFeO₂ structure along [100] zone axis superposed onto the STEM images exactly matches with the both images.

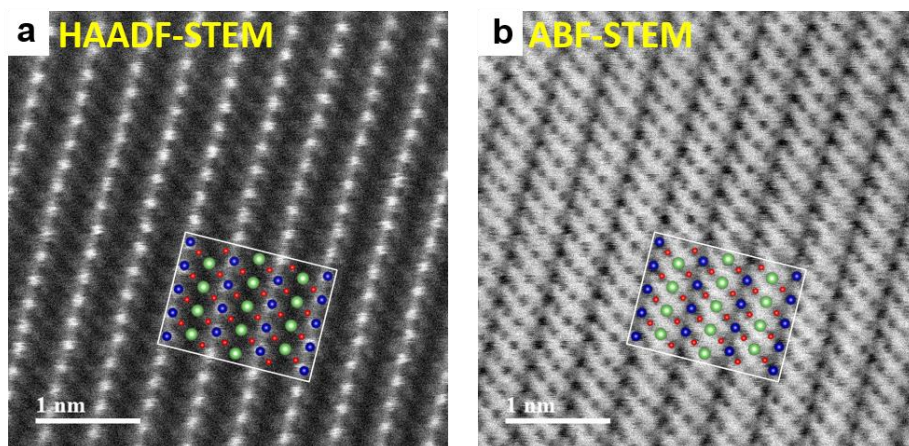


Figure 2.6. Atomic-resolution (a) HAADF- and (b) ABF-STEM images of pristine NCM cathode material.

The atomic structure model is superposed onto each image.

2.3. Structural evolution of NCM cathode material during electrochemical cycles

2.3.1. Structural transformation at the surface of primary particles

By TEM investigation of the electrochemically cycled NCM cathode materials with the TEM samples made by FIB technique, similar to the pristine material, we could identify the structural evolution of primary particles during the cycles. Given that the

Chapter 2. Visualization on degradation of Ni-rich Ni/Co/Mn cathode material

secondary particles are the cluster of physically adhering primary particles, the identification of the electrochemical reaction mechanism of primary particles would lead to the understanding on the reaction mechanism of the whole NCM cathode material.

As already revealed by numerous previous reports,[20, 22] we could observe the structural changes near the surface of primary particles after cycles with various TEM techniques. Figure 2.7 shows an HRTEM image of a primary particle after 300 cycles with 1C rate. The inside of the primary particle was revealed to have the same crystal structure with its pristine state, α -NaFeO₂ or LiMO₂ structure, based on the FFT pattern shown in Figure 2.7c. However, the diffraction peaks from {003} and {01-1} planes gradually became faint as it approached to the surface of the particle. The FFT pattern obtained from the surface of the material (Figure 2.7d) can be indexed as the rocksalt structure (space group Fm-3m), which is same as the α -NaFeO₂ structure with the indistinguishably mixed layers of transition metal ions and lithium ions. The corresponding atomic structure models are drawn in Figure 2.7e and f. In other words, the disappearance of {003} peaks of the layered oxide structure should be attributed to the impossibility to differentiate between the lithium and the transition metal layers because of severe cation mixing near the surface. It implies that the transition metal ions and lithium ions invade the each other's layers during the charge and discharge procedure. However, given that the diffusivity of the lithium ion is much higher than the transition metal ions and the two-dimensional lithium layers are the most effective paths for the lithium-ion diffusion, it is likely that the slow transition metal ions have higher driving forces to invade the lithium layers during the charge process for moving easily through the already empty lithium layers.

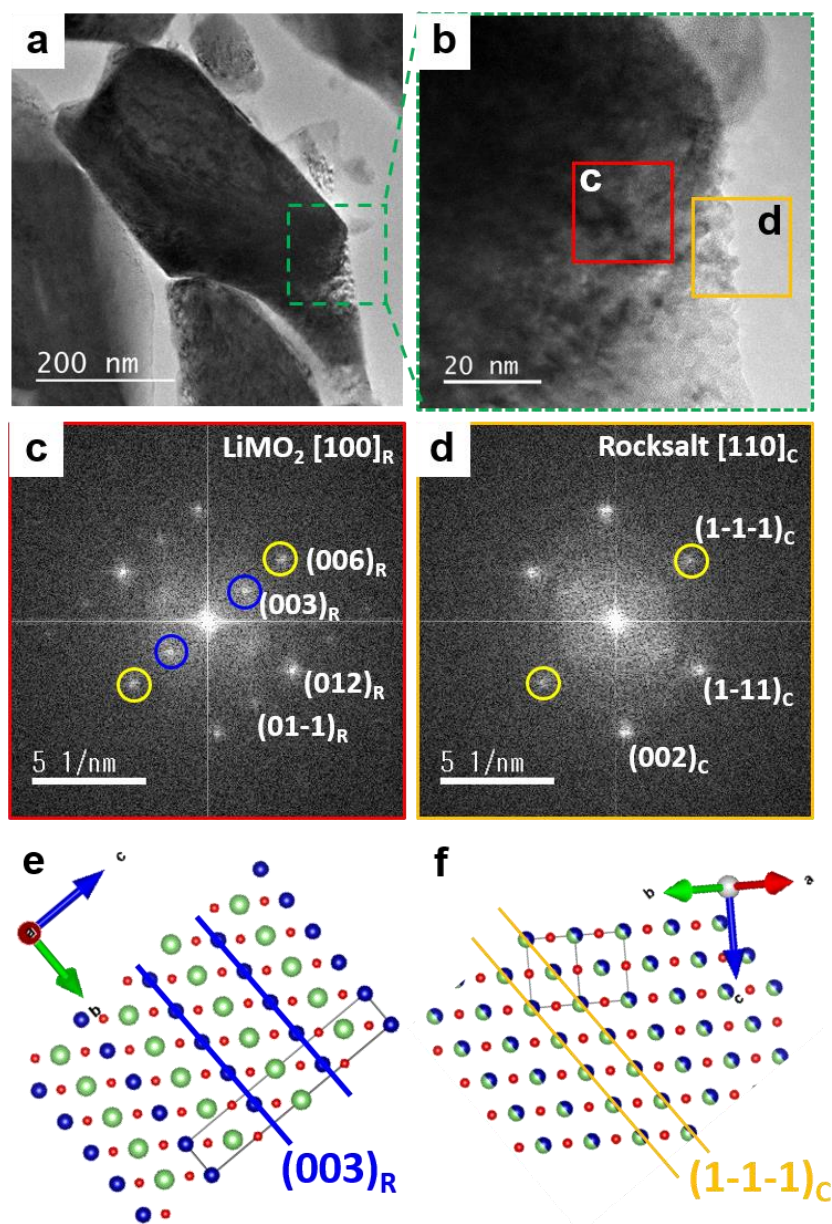


Figure 2.7. (a, b) HRTEM images and (c, d) FFT patterns of 300 cycled NCM 8/1.5/0.5 cathode material. (e, f) Corresponding atomic structure models at the region (c) and (d), respectively.

Chapter 2. Visualization on degradation of Ni-rich Ni/Co/Mn cathode material

We further investigated the structural transformation near the surface by dark-field imaging technique as shown in Figure 2.8. The dark-field imaging helps to comprehend the overall distribution of the layered LiMO_2 and the rocksalt phase in the larger area than HRTEM studies. It can separate the layered LiMO_2 phase from the rocksalt phase by dark-field images, however, unfortunately, it is not possible to perfectly distinguish the rocksalt phase from the layered LiMO_2 phase due to the overlap of the diffracted peaks. As shown in Figure 2.7c and d, all of the diffraction peaks from the rocksalt phase are overlapped with the peaks from the layered LiMO_2 phase, whereas there are additional peaks in the layered LiMO_2 phase, which are not in the rocksalt phase; it makes impossible to perfectly divide the rocksalt phase from the layered LiMO_2 phase. Nevertheless, it is still possible to speculate about the rough area of the rocksalt phase by comparing with the dark-field images of the layered LiMO_2 phase fully separated from the rocksalt phase.

In the SAED pattern (Figure 2.8a) obtained from the primary particle shown in the both bright-field images in Figure 2.8b and e, the diffraction peak nearest the transmitted electron beam indicated as DF-01 corresponds to the $\{003\}$ planes of the layered LiMO_2 phase shown in Figure 2.7c. Likely, the peak DF-02 in Figure 2.8a corresponds to both of the $\{006\}$ planes of the layered LiMO_2 phase and the $\{1-1-1\}$ planes of the rocksalt phase. Therefore, the dark-field images from the peak DF-02 (Figure 2.8c and f) only show the layered LiMO_2 phase, while Figure 2.8d and g show both of the layered LiMO_2 and the rocksalt phase. The remarkable difference between the two dark-field images from the peaks DF-01 and DF-02 is observed near the surface of the particle. It is shown that the dark-field images from DF-02 is bright near the surface, while it is not in the

Chapter 2. Visualization on degradation of Ni-rich Ni/Co/Mn cathode material

images from DF-01; it implies that the concentration of the rocksalt phase at the surface.

The structural transformation into the rocksalt phase is obvious at ~5 nm depth from the surface of the particle.

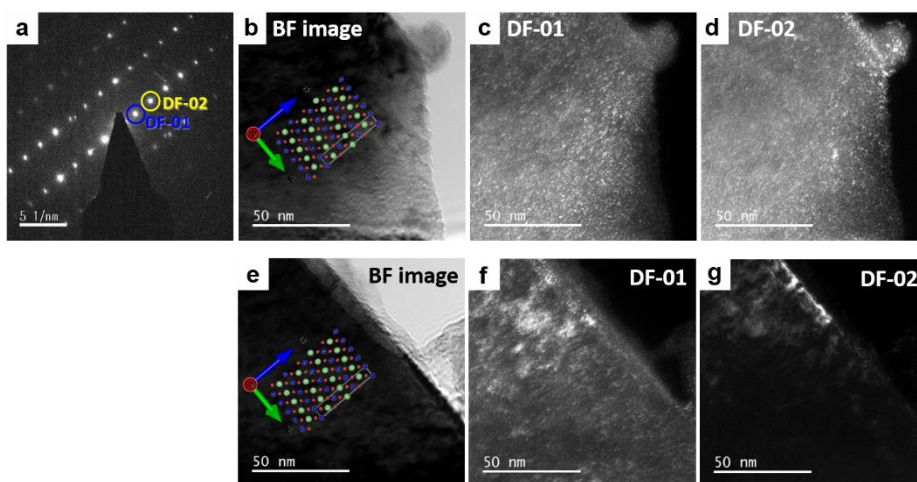


Figure 2.8. Two example sets of dark-field imaging of 300 cycled NCM 8/1.5/0.5 cathode material. (a) A SAED pattern of the primary particle. (b, e) Bright-field images. (c, d, f, g) Dark-field images obtained from the (c, f) DF-01 and (d, g) DF-02 peaks indicated in (a).

We, therefore, focused on the structural evolution near the surface of the particles, and the more detailed information was obtained by atomic-resolution STEM image analyses. The structural transformation from the surface during the cycles is clearly shown in Figure 2.9. In Figure 2.9a, the transition metal layers and the lithium layers are obviously distinguished at the inside of the primary particle; the transition metal ions are observed, but the lithium ions are invisible due to its low atomic number. However, as it approaches to the surface, several atoms are observed in the lithium layers, which implies the invasion of the transition metal ions into the lithium layers. Finally, the transition metal

Chapter 2. Visualization on degradation of Ni-rich Ni/Co/Mn cathode material

layers and the lithium layers are transformed to be indistinguishable at the far surface. The line-scanned intensity profiles of the HAADF-STEM images (Figure 2.9c and d) confirm the structural evolution of the layered LiMO_2 structure toward the rocksalt structure near the surface. The HAADF-STEM image intensity increment of the lithium layers from the inside to the surface led to the appearance of the intermediate spinel-like near the surface, and it finally resulted in the same intensity between the transition metal and the lithium layers. It may imply that the repeated lithium-ion extraction/insertion during the cycles causes the migration of the transition metal ions leading to the formation of the more stable rocksalt structure at the surface of the particles where the structural transformation can easily occur.

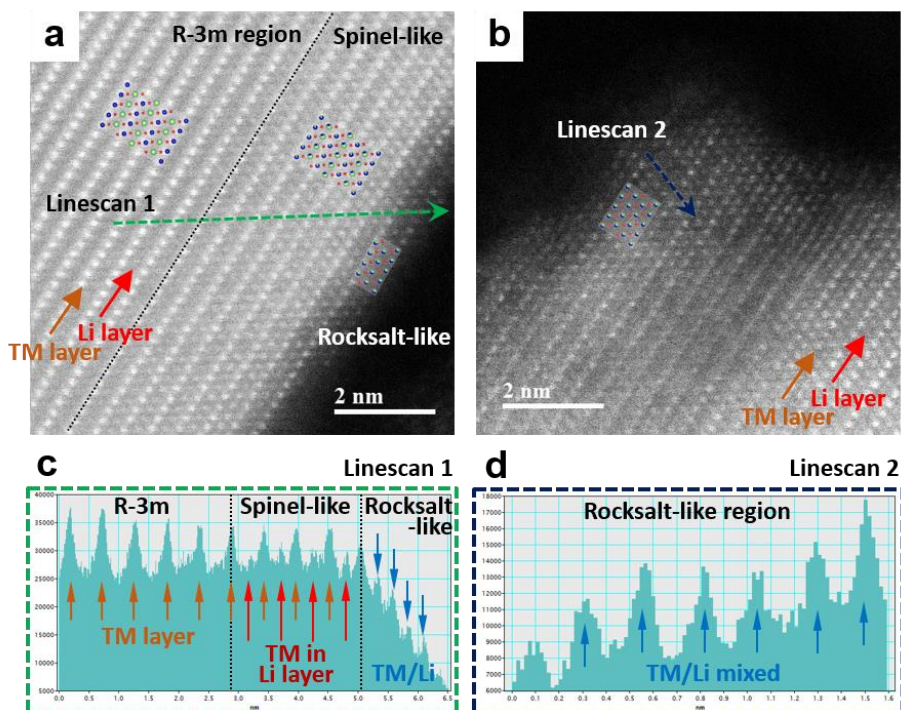


Figure 2.9. (a, b) HAADF-STEM images of NCM 8/1.5/0.5 cathode materials after 300 cycles with 1C current rate. (c, d) Line-scanned intensity profiles along the indicated arrows in the HAADF-STEM images in (a) and

(b).

2.3.2. Lithium-ion defects at tetrahedral position

As shown in the above STEM images and atomic structure models, lithium and transition metal ions generally occupy the octahedral positions with the nearby oxygen ions forming the MnO_6 octahedral in the pristine NCM cathode material with $\alpha\text{-NaFeO}_2$ structure. There have been several reports suggesting that the transition metal and the lithium ions use the tetrahedral sites as the diffusion paths during the de/lithiation or the cation mixing procedure, but it was not clearly revealed yet.[27, 28] In this STEM image study, we could find out that lithium ions are possible to occupy the tetrahedral sites during the cycles in the NCM cathode material. The atomic structure model of the lithium-ions at the tetrahedral sites are drawn in Figure 2.10d. Figure 2.10 is an example that shows the occupancy of lithium ions at the tetrahedral sites. The HAADF- and ABF-STEM images in Figure 2.10a and b are taken at the surface of a primary particle of NCM 8/1.5/0.5 material after 300 cycles with 1C current rate. As already explained above, several transition metal ions are observed in the lithium layers near the surface due to the cation mixing during the cycles. Interestingly, the dark contrast is observed at a few uncommon sites of the lithium layers in the ABF-STEM image, which is boxed in Figure 2.10b. The position is coincident with the tetrahedral sites of the lithium layers. It could be attributed to the transition metal ions or the lithium ions at this position, and the comparison with the HAADF-STEM image (Figure 2.10a) confirmed that it would be the lithium ions. As shown in the line-scanned intensity profile of the STEM images

Chapter 2. Visualization on degradation of Ni-rich Ni/Co/Mn cathode material

(Figure 2.10c), the contrast at the tetrahedral sites were only detected at the ABF-STEM image, which implies that the contrast in the ABF-STEM image have originated from the light element. However, lithium ions detected at the tetrahedral sites were only a few in all possible sites; therefore, it is not enough to say that lithium ions generally pass through the tetrahedral sites during the de/lithiation process. Rather, it could be more possible that lithium ions occupy the tetrahedral sites as defects when the diffusion is impeded by other ions.

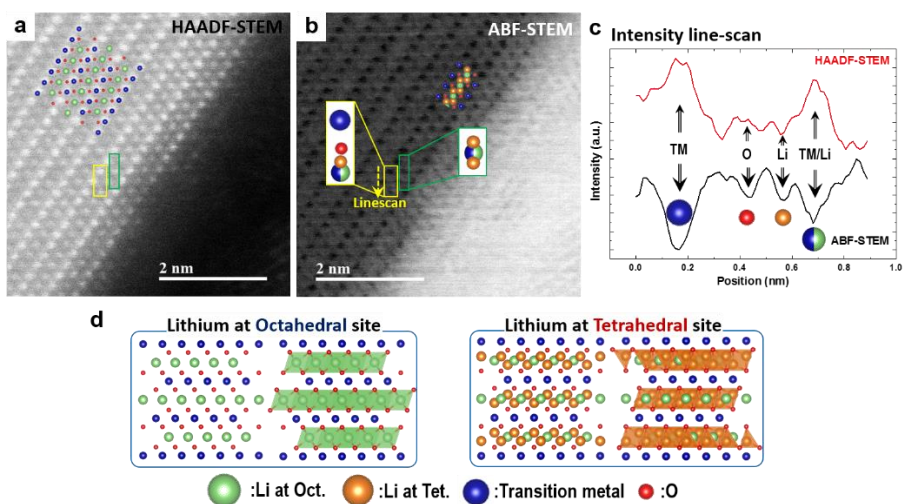


Figure 2.10. (a, b) An example set of atomic-resolution (a) HAADF- and (b) ABF-STEM images showing the occupancy of lithium ions at tetrahedral sites after 300 cycles. (c) Line-scanned intensity profile of STEM images. (d) Atomic structure model of NCM cathode material with lithium ions at octahedral and tetrahedral sites.

2.4. Comparison between NCM 1/1/1 and 8/1.5/0.5 materials

2.4.1. Surface deterioration of primary particles

Here, we directly compared the changes during the cycles between NCM 1/1/1 and 8/1.5/0.5 materials to identify the origin of the severe degradation in Ni-rich NCM cathode material. We first observed the overall changes that occur during the cycles at the micro-scale in the secondary particle. Figure 2.11 shows an example set of SEM images that compares the structural deterioration after 50 cycles between NCM 1/1/1 and 8/1.5/0.5 materials. The NCM electrode was loaded into the FIB instrument, and a secondary particle was cut as shown in Figure 2.11a and b. Then the electrode was electrochemically cycled in the battery cell with lithium reference electrode. After 50 cycles, the electrode was gently washed and the cross section of the secondary particle was slightly cut again by FIB to clearly observe the cross section by removing the residual electrolyte on the surface. It is the reason why some of the cracks observed in the pristine state disappeared in the image taken after 50 cycles (Figure 2.11a and c).

It is shown that two NCM materials with different composition ratios have different sizes of primary particles and different packing density at the pristine state. The secondary particle size is similar, but NCM 1/1/1 material is composed of larger primary particles, which are densely packed, while NCM 8/1.5/0.5 material is composed of much smaller primary particles coarsely packed containing numerous voids. The different primary particle size between NCM 1/1/1 and 8/1.5/0.5 can be attributed to the synthesis conditions, but it could also imply the instability of the Ni-rich NCM

Chapter 2. Visualization on degradation of Ni-rich Ni/Co/Mn cathode material

compound. The structural deterioration discrepancy after 50 cycles is obvious as shown in Figure 2.11c and d. Cracks are more developed in the both samples, but most of bonding among the primary particles are well maintained in NCM 1/1/1 material.

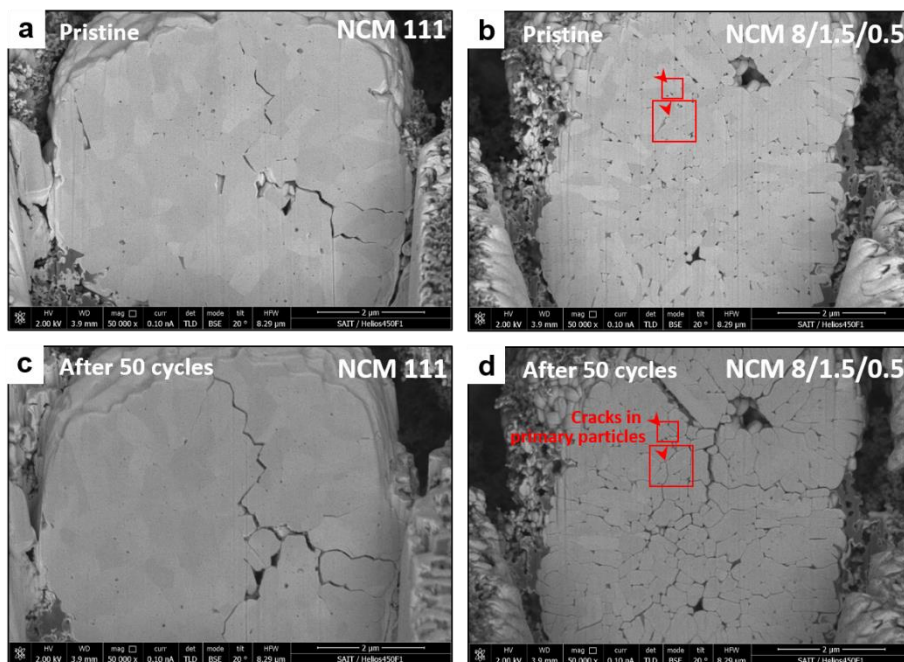


Figure 2.11. SEM Cross-sectional images of secondary particles of NCM cathode material. Structural deterioration after 50 cycles was compared between (a, c) NCM 1/1/1 and (b, d) 8/1.5/0.5 materials.

There is almost no structural degradation observable in the NCM 1/1/1 sample. However, cracks are severely developed in NCM 8/1.5/0.5 material and crevices are noticeable at most of the primary particle surfaces. It may be attributed to the severe volume changes of Ni-rich NCM material during the charge and discharge procedure, which was proposed by the experimental results and calculations in previous reports. [29, 30] In addition, it seems that cracks are developed even in a single primary particle, which

Chapter 2. Visualization on degradation of Ni-rich Ni/Co/Mn cathode material

generally has much stronger bonding than the bonding between the primary particles. Those clearly tell the weak bonding and the instability of Ni-rich NCM material at a glance.

We further compared the NCM 1/1/1 and 8/1.5/0.5 material closely by making TEM samples with FIB technique. Figure 2.12 shows low-magnification images of the samples taken by TEM. Each TEM sample contains primary particles in a single secondary particle, which is 300-cycled with 1C current rate in a full cell battery. As expected based on the cross-sectional SEM images, NCM 8/1.5/0.5 material suffered severe degradation after 300 cycled, whereas NCM 1/1/1 material well maintains its morphology even at the surfaces of the primary particles. The TEM images further show the thick surface electrolyte interphase (SEI) layers on the Ni-rich cathode material. The transparent polymeric layers observed between the primary particles are the SEI layers, which are formed by the reaction between the electrolyte and the NCM cathode material. It obviously shows the reasons of fast capacity fading during the cycles in the Ni-rich NCM cathode material. In addition to the influence of severe volume changes, it appears that Ni-rich NCM material easily dissolves in the electrolyte, which results in the shrinkage of the active material and the sluggish diffusion of lithium ions through the SEI layers.

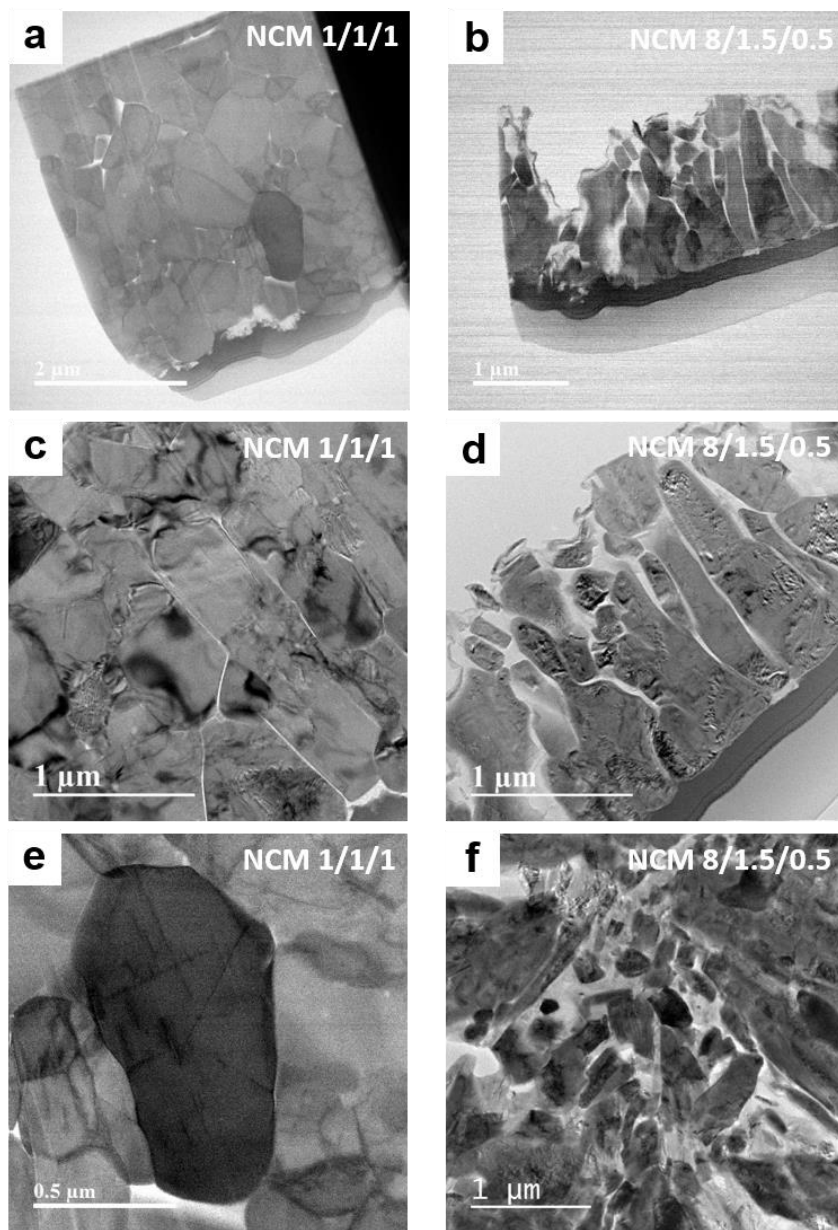


Figure 2.12. Low-magnification (c, d, f) TEM and (a, b, e) ABF-STEM images of 300-cycled NCM (a, c, e)

1/1/1 and (b, d, f) 8/1.5/0.5 cathode materials.

Chapter 2. Visualization on degradation of Ni-rich Ni/Co/Mn cathode material

Further comparison with atomic-resolution HAADF-STEM images confirms the severe surface dissolution and deterioration after the cycles in the Ni-rich NCM material (Figure 2.13). The cation mixing phenomenon was also observed at the surface of the primary particle in NCM 1/1/1 material, but the depth of the cation mixing from the surface was less than 5 nm even after 300 cycles. In addition, it maintains the flat surface, which implies the low dissolution at the surface of the NCM 1/1/1 material given that there was almost no separation between the primary particles observed in the SEM and TEM images (Figure 2.11 and 2.12). On the other hand, Ni-rich NCM material has rough surface after the cycles and the cation mixing was frequently observed in places near the surface. Rocksalt structure is clearly observable at the surface. As shown in Figure 2.13b and d, there are some distinct regions where it is well focused or not. It may imply the different height forming terrace near the surface or the severe structural collapse in partial regions, both of which support the severe dissolution of the Ni-rich NCM material during the cycles.

Interestingly, the structural collapse was not much severe at the surface facing the slabs. The surfaces facing the slab planes show very similar feature between NCM 1/1/1 and 8/1.5/0.5 materials. They show flat surface as well as the limited depth of the cation mixing even in the Ni-rich material. In addition, the transition metal layers and the lithium layers are still distinguishable, which implies the low degrees of the cation mixing at this surface. It may be related to the surface energy. It appears that {003} planes of Ni-rich NCM cathode material with α -NaFeO₂ structure, i.e. the slab planes, have much lower surface energy than the planes that the lithium and the transition metal

Chapter 2. Visualization on degradation of Ni-rich Ni/Co/Mn cathode material

layers are both exposed, e.g. {10-2} or {xy0} planes; accordingly the latter planes may break easily during the cycles.

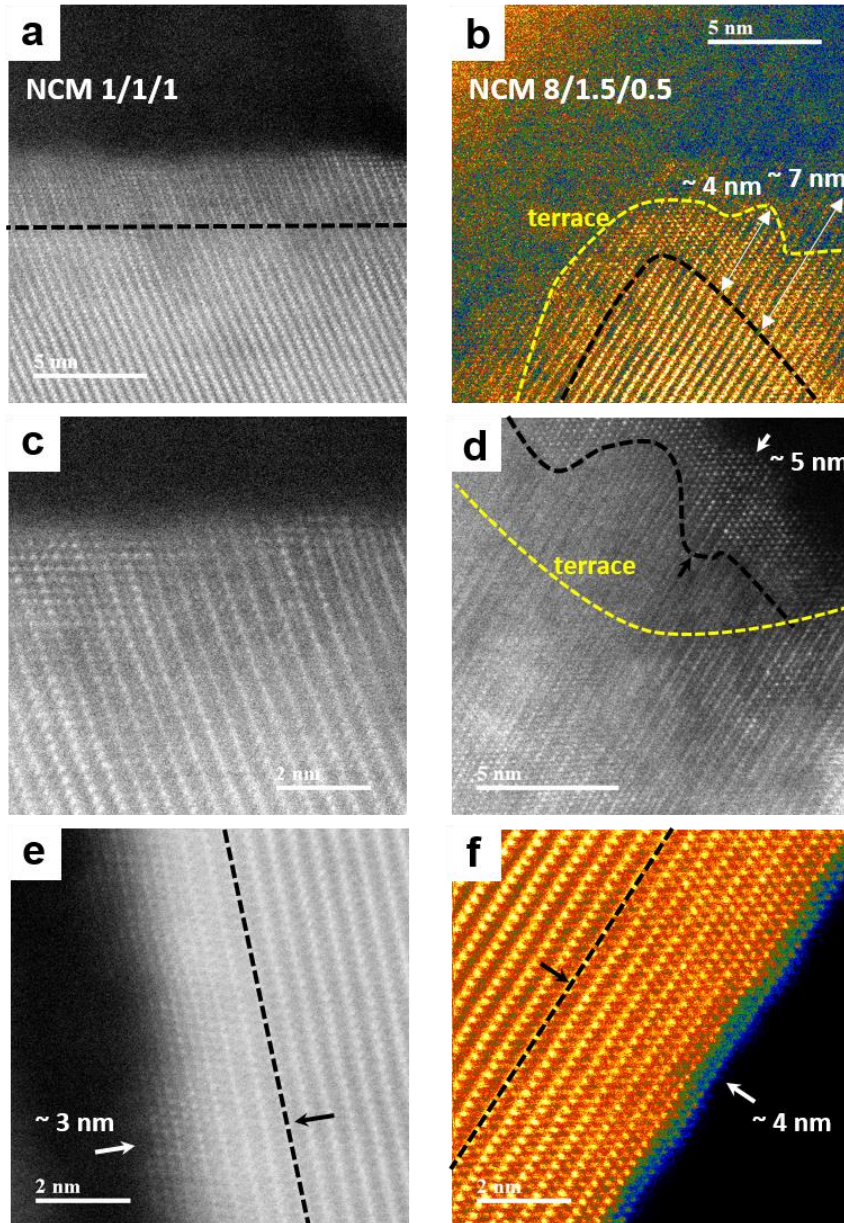


Figure 2.13. Atomic-resolution HAADF-STEM images obtained near the surface of 300-cycled primary particles of (a, c, e) NCM 1/1/1 and (b, d, f) 8/1.5/0.5 cathode materials.

Chapter 2. Visualization on degradation of Ni-rich Ni/Co/Mn cathode material

To investigate the dissolution of the Ni-rich NCM cathode material, we performed inductively coupled plasma atomic emission spectroscopy (ICP-AES) analysis. ICP-AES is an analytical method for the detection of metal elements. It dissolves the material in the acid and heat the solution to the high temperature to excite the atoms. Then it calculates the weight of the particular elements by detecting the emitted electromagnetic radiation at characteristic wavelengths of the elements. This machine finally provides the weight percentages of the detected materials. The ICP-AES analysis is beneficial for the measurement of the composition ratio of trace metals. Due to the impurities inevitably included in the samples during the ICP-AES analysis, e.g. the components of the acid solution, the absolute detected weights of the elements are not commonly important in this analysis, but the relative weight percentage is very meaningful.

Table 2.1. Inductively coupled plasma atomic emission spectroscopy (ICP-AES) data from a full cell battery.

Sample	Cycle	Raw data (wt %)				Relative atomic ratio (Ni = 1)			
		Li	Ni	Co	Mn	Li	Ni	Co	Mn
NCM 8/1.5/0.5 (Cathode)	Pristine	6.60	42.72	5.32	4.95	1.307	1.000	0.124	0.124
	300-cycled	5.03	41.89	5.26	4.85	1.016	1.000	0.125	0.124
Graphite (Anode)	Pristine	0.00	0.00	0.00	0.00	-	-	-	-
	300-cycled	2.30	0.33	0.005	0.012	58.951	1.000	0.015	0.039
Separator	300-cycled	0.19	0.05	0.0022	0.0018	32.141	1.000	0.044	0.038

Chapter 2. Visualization on degradation of Ni-rich Ni/Co/Mn cathode material

In this study, the 300-cycled Ni-rich cathode, graphite anode, and separator were analyzed by ICP-AES and compared with the pristine materials. After the 300 cycles of a full cell battery with 1C current rate, the cell was disassembled and each component used for the ICP-AES analysis. The ICP-AES data is shown in Table 2.1. The relative atomic ratio was calculated from the weight percentage data. The relative atomic ratio of the pristine NCM cathode material shows the composition ratio of Ni:Co:Mn as 8:1:1, which confirms that the pristine material has high nickel content. The ratio was maintained even after 300 cycles, but the amount of lithium ions were relatively decreased, which implies the lithium-ion defects in the NCM material and the capacity fading after cycles. Even though it showed similar relative atomic ratio of Ni/Co/Mn in the cathode after cycles, it does not necessarily indicate the uniform dissolution of transition metal ions at the surface of each particle because the surface takes only a little portion of the whole material.

The detection of Ni, Co, and Mn elements at the graphite anode and separator after 300 cycles confirms the severe dissolution of transition metal ions from the Ni-rich NCM cathode material. The calculated relative atomic ratio of Ni/Co/Mn at separator shows the easier dissolution of nickel ions given that the nickel ions have much higher proportion among Ni, Co, and Mn ions than the composition ratio of the cathode material. In other words, because most of the detected ions in the separator may reflect the composition of the electrolyte, we can say that the nickel ions are much dissolved into the electrolyte during the cycles. In particular, Ni ions were even detected at the graphite anode side with the higher proportion compared to Co and Mn ions. The detected transition metal ions at the graphite anode may have originated from the inside

of the anode and the residual electrolytes on the surface of the anode, both. Therefore, it is risky to conclude that the transition metal ions are inserted into the anode during the cycles. Still, we can say that the severe dissolution of transition metal ions, nickel ions in particular, from the Ni-rich NCM cathode material may accelerate the degradation of the anode as well as the cathode, considering that the nickel ions can act as the lithium ions attributed to their similar ionic sizes.[31]

2.4.2. Crack development in primary particles

Besides the surface degradation, we could observe several cracks developed in a single primary particle. Figure 2.14a shows an example of the crack that was developed in a single primary particle. As shown in the figure, the separated particles upward and downward share very similar outer border shape, which is highly probable to have originated from a single primary particle. In addition, the boundary line between the two small particles seems to fit well to each other. We performed HRTEM analysis in the nearby area to reveal where the cracks occur. Figure 2.14b, c, e, and f are the FFT patterns derived from the HRTEM images taken from the zone axis aligned for the upper particle. Figure 2.14b and c were well indexed as the [120] zone axis of the layered LiMO_2 structure. The atomic-resolution HAADF-STEM images shown as the insets confirms the structure aligned to the [120] zone axis. Figure 2.14b is almost same as the pristine state without cation mixing in the lithium layers, which implies that the pristine structure is well maintained during the cycles at the inside of the particles. However, the {003} peaks disappeared near the crack point, which indicates that the layered LiMO_2 structure

Chapter 2. Visualization on degradation of Ni-rich Ni/Co/Mn cathode material

transformed into the rocksalt structure where the transition metal and lithium layers are indistinguishable.

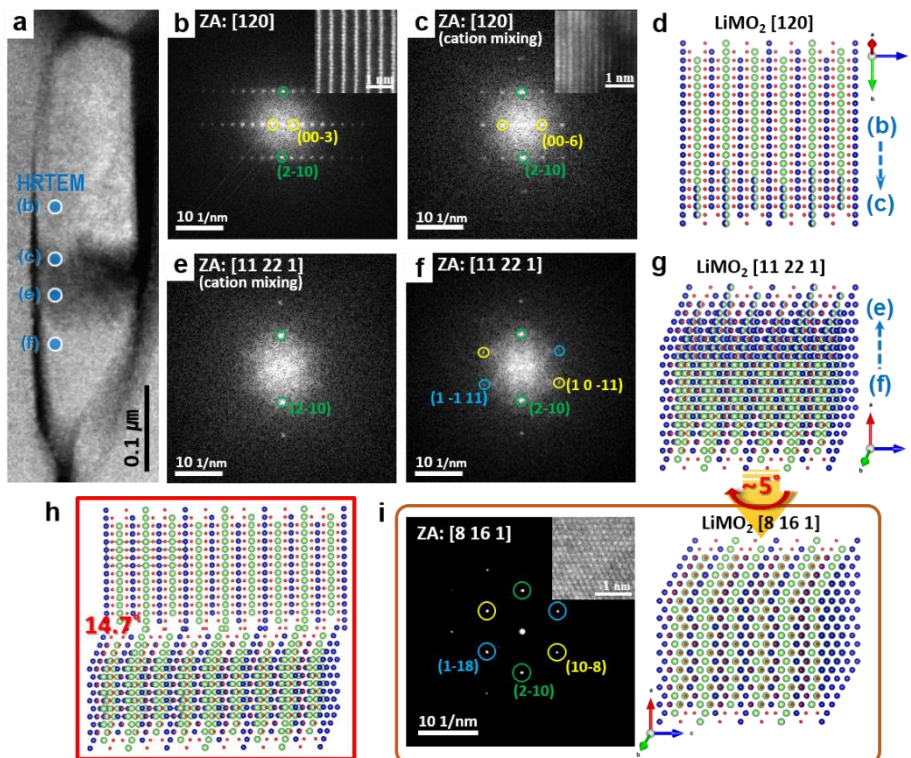


Figure 2.14. HRTEM analysis of crack points, which identifies the region where the crack occurs in the Ni-rich NCM cathode material. (a) A HAADF-STEM image at the crack developed primary particle. (b, c, e, f) FFT patterns from HRTEM images taken at the regions indicated in (a). (d, g) Atomic structural models corresponding to the regions indicated next to the models. (h) Atomic structural model showing the original crystal orientation relationship of the crack region. (i) SAED pattern at the zone axis tilted 5 degrees from the direction shown in (f).

The HAADF-STEM image shows the cation mixed structure observed near the crack point. Because the zone axis was aligned on the basis of the upper particle, we could not

Chapter 2. Visualization on degradation of Ni-rich Ni/Co/Mn cathode material

obtain clear FFT patterns from the HRTEM images of the lower particle (Figure 2.14e and f). Nevertheless, it was possible to be indexed as the high-index zone axis, $[11\ 22\ 1]$, of the layered LiMO_2 structure. Similar to the upper particle, several diffracted peaks vanished near the crack point due to the cation mixing phenomenon. The direction of the lower particle was confirmed by the SAED pattern acquired after tilting of small degrees for the alignment along the lower-index zone axis of the lower particle (Figure 2.14i). The SAED pattern shown in Figure 2.14i is indexed as $[8\ 16\ 1]$ zone axis of the layered LiMO_2 structure and the atomic-resolution HAADF-STEM image obtained at this zone axis agrees with the atomic structural model. In addition, the orientation and the angle relationships between $[11\ 22\ 1]$ and $[8\ 16\ 1]$ match well with the tilting direction and angle; it clearly confirms that the lower particle was accurately indexed. The original orientation relationship between the upper and lower particles before the crack development is drawn in Figure 2.14h; the edges of the slabs in the upper and the lower particles are facing each other with slightly tilting angles. It implies that the crack developed at the low-angle grain boundary between the grains in a primary particle. The low-angle grain boundary was already observed in numerous primary particles as shown in Figure 2.4 and 2.5. We already showed that the primary particles are mostly composed of the poly-crystals connected with the low-angle grain boundaries. It seems that the low-angle grain boundaries can act as the surface of the primary particles where structural transformation into the rocksalt structure occurs. Based on the HRTEM-FFT and HAADF-STEM analyses, the structural transformation at the low-angle grain boundary in the primary particle may weaken the bonding of the grain boundary, which finally results in the separation of two nearby grains.

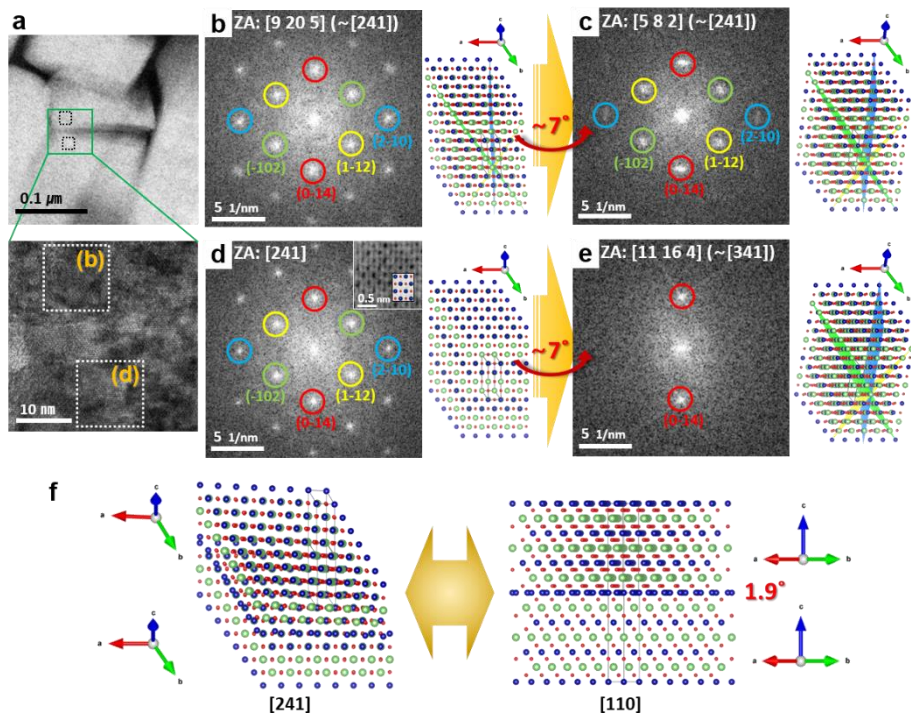


Figure 2.15. Another example of the crack development in a single primary particle. (a) A HAADF-STEM (upper) and a HRTEM image (lower) at the crack developed primary particle. (b-e) FFT patterns from HRTEM images showing the direction of each region. (f) Atomic structural model of the interested region before the crack development.

Another example of the crack development is shown in Figure 2.15. The HAADF-STEM image in Figure 2.15a shows the primary particle after the crack development. The separated border is clearly seen at the center of the figure. It seems that the crack caused the tilting of two separated particles. We identified the crystal orientation relationship between two nearby separated particles as the same way with the former case (Figure 2.14). We compared the FFT patterns at the left side of the particles that seemed to be the smallest tilting region. The zone axis was aligned to the region of Figure

Chapter 2. Visualization on degradation of Ni-rich Ni/Co/Mn cathode material

2.15d, but the same zone axis of Figure 2.15b was also very close with only slight tilting angle difference. This is why the two FFT patterns of Figure 2.15b and d are very similar. The lower particle can be easily indexed as the [241] zone axis of the layered LiMO_2 structure and it was confirmed by the atomic-resolution ABF-STEM image shown as inset in Figure 2.15d. The orientation of the upper particle was identified by comparing with the FFT patterns obtained after tilting with 7 degrees. The similar FFT pattern was observed again even after tilting of 7 degrees, which is attributed to the higher order Laue zone (HOLZ) effect of the high-index zone axis. Based on the two FFT patterns from different zone axes, the zone axis of the Figure 2.15b could be identified as [9 20 5], which is only 1.9 degrees away from [241]. The crystal orientation relationship of the crack region shown in Figure 2.15a is illustrated by atomic structural model in Figure 2.15f. The two separated particles seem to have bonded with small tilting angle, originally. But in this case, the crack occurred along the grain boundary that a slab plane is facing at, which shows a perpendicular relationship with the former case of the crack shown in Figure 2.14. It implies that the cracks can occur at the low-angle grain boundaries in a primary particle regardless of the orientation relationship of the grain boundaries after severe deterioration of the material. Figure 2.16 shows an example of noticeable cation mixing observed at the grain boundary region. Transition metal ions migrated into the lithium layers at the grain boundary during the cycles like the surface of primary particles. It signifies that grain boundary would be the next unstable region to the surface in primary particles, which justifies the possibility of the crack development in primary particles.

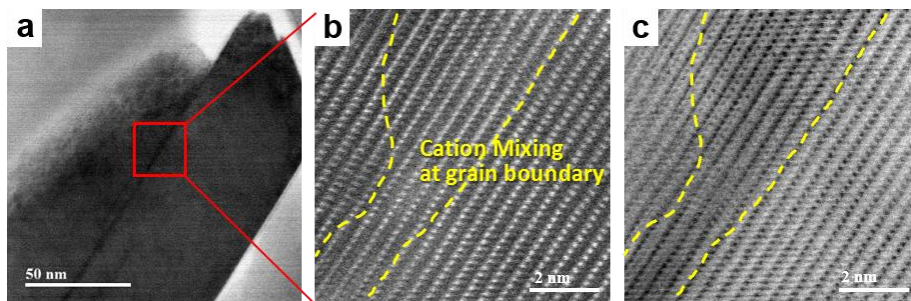


Figure 2.16. Noticeable cation mixing phenomenon at low-angle grain boundary (a) A low-magnification ABF-STEM image of the grain boundary region. (b) HAADF- and (c) ABF-STEM images show that the migration of transition metal ions is remarkable near the grain boundary.

Comparison of average primary particle size before and after the electrochemical cycles in NCM 8/1.5/0.5 material (Table 2.2) shows the probability of the crack development in primary particles. At the severely deteriorated region after 300 cycles under the full-cell test, the primary particles were reduced to nearly half size of the pristine particles. It implies that cracks were developed in the primary particles resulting in the separation of a primary particle into two particles. In addition, it shows that the crack development in primary particles should also be considered as one of the important factors that attribute to the fast capacity fading in Ni-rich NCM cathode materials.

Table 2.2. Comparison of average primary particle size before and after electrochemical cycles in NCM 8/1.5/0.5 material.

Primary particle	Average size (nm)	Standard deviation (nm)
Pristine	466	189
300-cycled ^{a)}	282	60

a) Primary particle sizes were calculated at the severely deteriorated region.

2.5. Summary

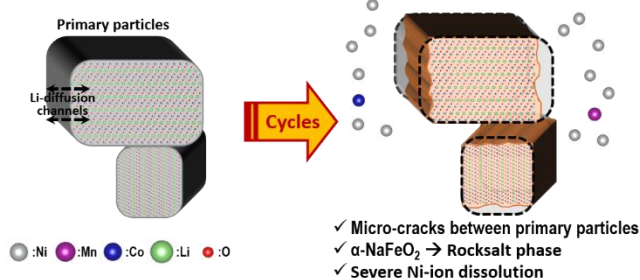
We directly visualized and compared the structural degradation of the NCM cathode materials depending on the Ni-content by comprehensive TEM studies. By observing the structural changes of the electrochemically cycled NCM cathode materials through TEM as well as SEM images, we found out that the micro-cracks between primary particles, the structural transformation and the dissolution of nickel ions from the surface of the primary particles would be the major origins of the worse capacity retention during the cycles in the Ni-rich NCM cathode materials. The further investigation with ICP-OES analysis revealed that the severe Ni-ion dissolution into the electrolyte may also affect the faster degradation of the anode material because of the Ni-ion invasion into the anode material with lithium ions during the charge process. Moreover, we revealed that cracks can be developed at low-angle grain boundaries between the nearby grains, even in a primary particle, which also can be one of the important factors that contribute to the fast capacity fading after the prolonged cycles. The degradation mechanisms of Ni-rich NCM cathode material is illustrated in Figure 2.17.

Based on the experimental results, we suggest the direction for the better performance of the Ni-rich NCM cathode material. First, the size of the primary particles should be optimized for the better cycle performance. The smaller the size, the easier full lithiation and delithiation. However, the smaller primary particles create the larger surface area, which leads to the severer structural transformation and the dissolution. Therefore, the primary particle size should be adjusted compromising the pros and cons that accompany with the size effect. In addition, the surface treatment that can make the

Chapter 2. Visualization on degradation of Ni-rich Ni/Co/Mn cathode material

nickel ions stable or protect from the structural transformation would be very effective for the cycle performance improvement of the Ni-rich NCM cathode materials. Because the faster capacity fading comes from the surface degradation including the structural transformation and the transition metal-ion dissolution due to the instability Ni-rich NCM materials, the surface treatment, e.g. surface coating or doping, will contribute to the maintenance of the material during the cycles.[32]

1. Micro-cracks & Surface Degradation btw/of primary particles (Major factor)



2. Crack Development in a primary particle (Minor factor)

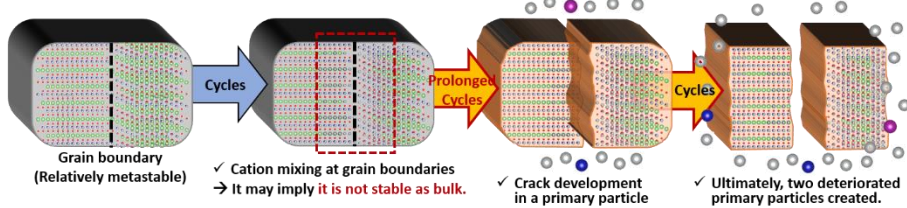


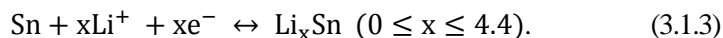
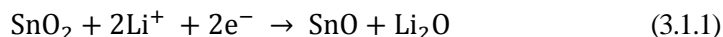
Figure 2.17. Schematic illustration of the degradation of Ni-rich NCM cathode material.

Chapter 3

Extra capacity of SnO₂ anode in lithium-ion battery investigated by *ex situ* TEM analysis

3.1. Introduction

Tin oxide (SnO₂) has been studied as a promising alternative to the commercially used graphite anode material because of its much higher theoretical specific capacity, which arises from different electrochemical reactions.[7, 33-36] Recently, it has attracted increasing interest again due to its high performance in sodium-ion batteries.[37, 38] The reaction mechanism includes conversion and subsequent alloying reaction as follows:



This mechanism was first proposed in 1997 based on *in situ* X-ray diffraction (XRD) studies.[39-41] The SnO₂ material is first transformed into tin metal (Sn) and lithium oxide (Li₂O) (Equations 3.1.1 and 3.1.2), and then the rechargeable battery operates by a reversible alloying reaction (Equation 3.1.3). The conversion reactions (Equations

3.1.1 and 3.1.2) usually occur as a single step under experimental conditions. Although reactions 3.1.1 and 3.1.2 are believed to be irreversible and consume considerable amounts of lithium ions, this could be an advantageous situation; the resulting Li₂O could act as a mechanical buffer against significant volume changes during de/lithiation.[42, 43]

However, a few unresolved but important questions concerning the reaction mechanisms of SnO₂ anodes in the lithium-ion battery system remain. First, the issue of extra specific capacity that exceeds the theoretical value, commonly reported for metal oxide/lithium (MO/Li) batteries, also occurs in the SnO₂/Li battery.[44-48] Many studies have tried to explain this phenomenon in MO/Li batteries using various analytical techniques such as infrared spectroscopy[49], nuclear magnetic resonance (NMR)[3, 50], X-ray photoelectron spectroscopy[49], mass spectroscopy,[51] and theoretical calculations[52-54]. These experiments commonly ascribed the origin of extra capacity to electrolyte decomposition[3, 54, 55] and interfacial storage[52, 53, 56, 57], however, it is still under debate. Recently, Hu et al. elucidated the origin of the additional capacity of the RuO₂/Li battery by *in situ* X-ray and NMR studies.[3] They showed that the additional capacities of transition metal oxide/lithium (TMO/Li) batteries derive from the reversible reaction between lithium hydroxide (LiOH) and Li₂O phases, which are initially formed by electrolyte decomposition and conversion reactions, respectively. However, TMO/Li batteries such as the RuO₂/Li cell operate by the reversible conversion reaction,[44] whereas the SnO₂/Li battery operates by the reversible alloying reaction of Equation 3.1.3.

Second, the partial reversibility of the conversion reactions (Equations 3.1.1 and 3.1.2)

has long been a subject of interest. Previous studies provided mostly indirect evidences such as interpretations of cyclic voltammogram,[58-61] Mössbauer spectroscopy,[62-64] energy-dispersive X-ray spectroscopy (EDS),[33, 65] and conductivity studies[66] to assert partial reversibility. Since it is known that Li-Sn alloys de-alloy below 1 V, reaction curve shown above 1 V is attributed to the additional reverse conversion reaction.[58-61] Furthermore, increased Sn-O bonding was observed by Mössbauer spectroscopy,[62-64] oxygen atoms were observed by EDS,[33, 65] and conductivity of the lithiated SnO₂ electrode was drastically decreased[66] during the delithiation process. Accordingly, the partially reversible reaction may primarily contribute to the extra capacity of the SnO₂/Li battery,[34, 46, 48, 67] provided that it is correct, but more direct and convincing evidence is required.

In this work, we studied the electrochemical reactions within the SnO₂ anode material to elucidate the origin of the extra capacity and the possibility of the reverse conversion reaction. Each major electrochemical reaction of the SnO₂/Li battery system was investigated by *ex situ* transmission electron microscopy (TEM). Using TEM for the structural and chemical analyses allowed the examination of distinctive features in each nano-area, which facilitated the detection of partial or localized reactions. The strategy applied for this work was to trace the same particles during the complete reaction cycle and to observe the phase evolution of the SnO₂ material during each electrochemical reaction stage. For the precise investigation, we developed an *ex situ* TEM characterization process to ensure that each electrochemical stage was the same as that occurring in a real battery cell. This approach is more realistic than conventional *in situ* TEM analysis in that it reflects the actual battery-operating environment. For instance, it

uses the usual ethylene carbonate/dimethyl carbonate (EC/DMC) electrolyte instead of an ionic liquid electrolyte. Moreover, it analyzes the electrode materials dis/charged in the all-around-electrolyte-covering environment of the real system rather than one-side-electrolyte-contacting condition for the traditional *in situ* TEM analysis method. The phase evolution of the SnO₂ electrode was further compared with that of the Sn electrode in which only reversible alloying reaction (Equation 3.1.3) takes place, using the same experimental procedure to reach an accurate conclusion. In this way, we concluded that the reactions associated with the Li₂O phase generated the extra capacity of the SnO₂/Li battery. Additionally, there was no trace of the reversed SnO₂ phase at all. Few re-oxidized SnO phases were observed, however, which turned out to have negligible effect on the capacity.

3.2. Experimental details

3.2.1. Directly (dis)chargeable TEM grid electrode preparation

For *ex situ* TEM analysis of the various (dis)charged states of SnO₂ particles, commercial SnO₂ particles (Sigma–Aldrich) and a carbon-support-film-coated copper mesh TEM grid (Ted Pella) were used as an active material and a current collector. SnO₂ particles ground by a mortar and pestle were dispersed in methanol, sonicated, and dropped onto the TEM grid. The grid was air dried overnight before being studied by TEM. For *ex situ* TEM investigation of Sn electrode as a comparison group, commercial Sn particles (Sigma–Aldrich) were used as an active material. The preparation method

was identical to that of the SnO₂ sample, except that the Sn particles were dispersed in anhydrous DMC, the entire process of which was performed in an argon-filled glove box to avoid oxidation of the material.

3.2.2. Electrochemical characterization and TEM analysis

Coin cells (CR2032 type) were assembled in the argon-filled glove box. The working electrodes included both the SnO₂ (or Sn) particles dispersed on the copper-mesh TEM grid and the conventional slurry electrode. The slurry electrode consisted of SnO₂ (or Sn) particles (70 wt%), polyvinylidene difluoride (PVDF) binder (10 wt%), carbon black (Super P) conductive agent (20 wt%), and *n*-methylpyrrolidone (NMP) solvent. It was coated onto copper foil, dried at 120°C for 30 min, and roll pressed. Then, the cell was assembled into a two-electrode cell with the slurry and apposed grid working electrodes, a Li metal counter electrode, a glass microfiber filter separator (GF/F, Whatman), and an electrolyte of 1M LiPF₆ in a 1:1 (v/v) mixture of EC and DMC. Charging and discharging of the TEM grid including the cell was performed at between 0.001 and 2.5 V (vs. Li⁺/Li) using a constant current–constant voltage (CC–CV) method; at each stage, the cell was (dis)charged at a current rate of 20 mA g⁻¹ and the voltage was retained until the current rate reaches 2 mA g⁻¹ at the end of the stage. The charge/discharge curves shown in Figure 3.1 were obtained without the grid electrode. The bright-field images and diffraction patterns were obtained with a 200 kV field-emission TEM instrument (JEM-2100F, JEOL). EELS experiments were performed in an energy-filtered TEM mode with an 80 kV field-emission TEM instrument equipped with an electron gun

monochromator (Titan G2 Cube 60-300, FEI).

3.3. Over-capacity phenomenon of the SnO₂ anode material

Figure 3.1 exhibits the over-capacity phenomenon in the experiments. The voltage profiles of the first cycle of the SnO₂/Li battery cell with various current values and thermodynamic titration curves are shown in Figure 3.1a. The specific capacities of the first discharge and charge processes at a current rate of 20 mA g⁻¹ were *ca.* 1800 and 1100 mAh g⁻¹, respectively. However, the contribution on the capacities from the conductive agent and binder used in the slurry electrode should be excluded for the accurate estimation of the additional capacity come from the active material. Figure 3.2 shows the voltage profiles of mixtures of a polyvinylidene fluoride (PVDF) binder and Super-P carbon-black conductive agent, which were included in the SnO₂ slurry electrodes. The binder and the conductive agent were mixed in the same ratio (1:2) as that in the SnO₂ slurry electrodes, shown in Figure 3.1. The electrochemical profile was measured twice to ensure reproducibility.

The first discharge and charge capacities were 375 and 160 mAh g⁻¹, respectively. Considering that the ratio between the active material (SnO₂ or Sn particles) and additives (the binder and the conductive agent) was 7:3, the capacity influence of the additives in the slurry electrode should be 3/7 that of the measured capacities in Figure 3.2. Therefore, the contributions of the additives to the capacity of the SnO₂ (or Sn) slurry electrode should be 160 and 70 mAh g⁻¹ during discharging and charging, respectively.

Accordingly, the specific capacities excluding the contribution of the additives

Chapter 3. Extra capacity of SnO₂ anode in lithium-ion battery investigated by ex situ TEM analysis

became 1640 (9.2 Li per SnO₂) and 1030 mAh g⁻¹ (5.8 Li per SnO₂), still exceeding the theoretical values of 1493 (8.4 Li per SnO₂) and 782 mAh g⁻¹ (4.4 Li per SnO₂), respectively. The over-capacity phenomenon of the SnO₂/Li battery is noticeable when compared with that of the Sn/Li battery. The experimental and theoretical capacities of the first cycle of the SnO₂/Li and the Sn/Li batteries are listed in Table 3.1.

As shown in the table, the extra capacity, beyond the theoretical value, appeared only in the SnO₂/Li battery. In particular, the over-capacity of the first charge in the SnO₂ material was remarkable, which was a 32 % higher experimental capacity than the theoretical value on the first charge. This clearly revealed that other electron-participating reactions were occurring in the first cycle, especially considerable in the charge process, complementing the well-known theoretical reaction mechanism.

Table 3.1. Experimental and theoretical capacities of the first cycle of the SnO₂/Li and Sn/Li batteries. The influence of additives (Figure 3.2) was subtracted from the experimental capacities. The over-capacity rate was derived by dividing the experimental capacity by the theoretical capacity.

	SnO ₂		Sn	
	1 st discharge	1 st charge	1 st discharge	1 st charge
Experimental capacity a) [mAh g ⁻¹]	1640	1030	880	650
Theoretical capacity [mAh g ⁻¹]	1493	782	993	993
Over-capacity rate ^{b)}	110 %	132 %	89 %	65 %

^{a)} Contributions of additives; *i.e.*, 160 mAh g⁻¹ during discharge and 70 mAh g⁻¹ when charging, were subtracted from measured capacities.

^{b)} Experimental capacity divided by theoretical capacity.

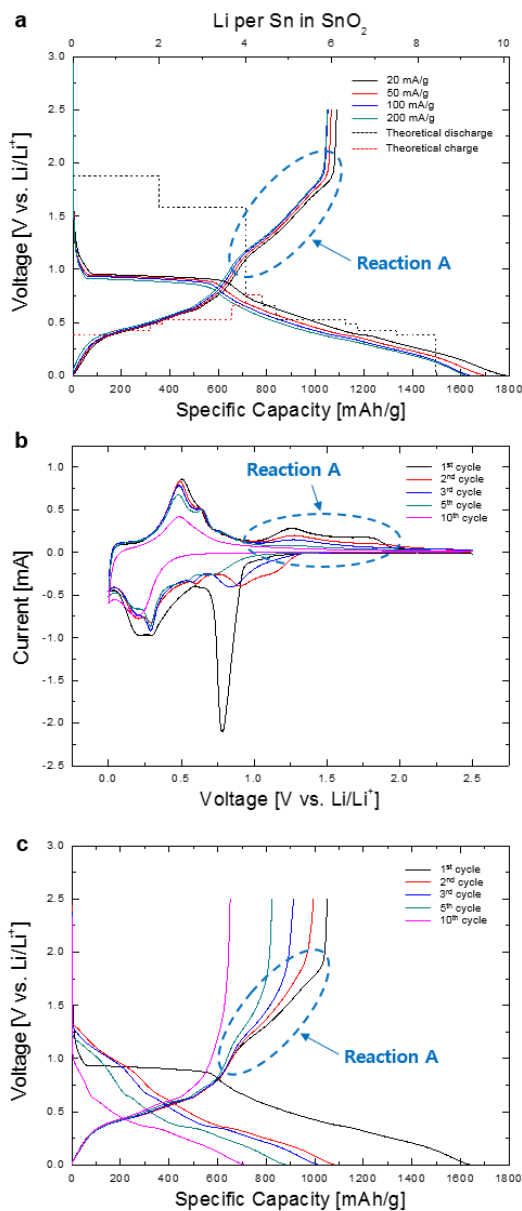


Figure 3.1. Electrochemical characteristics of the SnO₂/Li battery tested between 0.001 and 2.5 V (vs. Li/Li⁺).

(a) Voltage vs. specific capacity profiles of the first cycle for various current rates with thermodynamic titration curves. (b) Cyclic voltammograms of the first, second, third, fifth, and tenth cycles at a scan rate of 0.1 mV s⁻¹. (c) Voltage vs. specific capacity profiles of the first, second, third, fifth, and tenth cycles at a current rate of 100 mA g⁻¹. The label 'Reaction A' indicates the controversial reaction curve of the SnO₂/Li battery system.

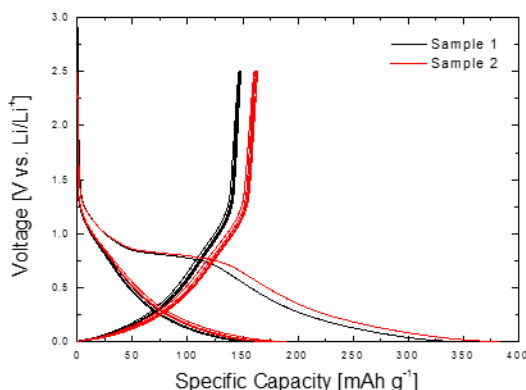


Figure 3.2. Voltage versus specific capacity profiles of the polyvinylidene fluoride (PVDF) binder-Super P carbon black conductive agent mixture, tested over the voltage range from 0.001 to 2.5 V (vs. Li/Li⁺). The results from two test samples are shown. The binder and the conductive agent were mixed at a ratio of 1:2, the same ratio as that used for the slurry electrode. The other components of the cell were identical to the case shown in Figure 3.1. Five cycles at a current rate of 20 mA g⁻¹ are shown for each.

The unknown reactions may be related to the gentle slope of the voltage profile charge curve, marked as ‘Reaction A’ in Figure 3.1. Two reaction peaks appeared at *ca.* 1.26 and 1.79 V (vs. Li/Li⁺) (Figure 3.1b). Because it is known that the de-alloying reaction of Li-Sn alloys occurs below 1 V on charging,[39] the precise nature of ‘Reaction A’ has remained unsolved. Furthermore, the relation of the gentle slope, ‘Reaction A’, to the unknown reaction, an immediate cause of the additional capacity in the SnO₂/Li battery, is more obvious when compared with the voltage profile of the Sn/Li battery (Figure 3.3). There were negligible contributions to the capacity in the corresponding region of the Sn/Li battery; this makes the difference in the extra capacity between the two batteries. On the other hand, the ‘Reaction A’ in the SnO₂/Li battery shows two distinct features; it emerged independent of the charge/discharge rate (Figure 3.1a) and

disappeared after a few cycles (Figure 3.1b and c).

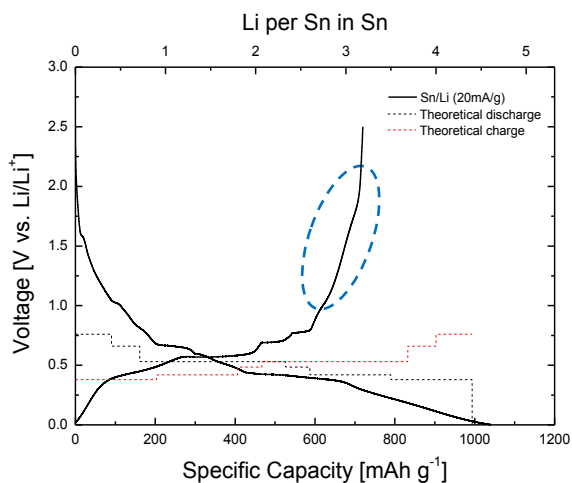


Figure 3.3. Voltage versus specific capacity profile of the first cycle of the Sn/Li battery at a current rate of 20 mA g⁻¹, drawn with thermodynamic titration curves. The blue dash-lined circle indicates the corresponding region of the controversial reaction (Reaction A) in the SnO₂/Li battery shown in Figure 3.1.

3.4. Realistic *ex situ* TEM investigation technique for the analysis

3.4.1. Preliminary *ex situ* X-ray diffraction analysis of the SnO₂/Li battery

We first conducted *ex situ* X-ray diffraction (XRD) studies of the SnO₂/Li battery to identify the reaction that occurred during the controversial stage (Reaction A). Stages IV and V (Figure 3.5b) were investigated with a focus on Reaction A. The SnO₂ slurry electrodes were fully discharged and charged toward the end of Stages IV and V in the coin cell. The cell was discharged/charged using constant current (20 mA g⁻¹) – constant

voltage (until 2 mA g⁻¹) method, similar to the conditions used in *ex situ* TEM analysis in this research. The slurry electrode was washed in DMC before XRD measurement.

Figure 3.4a shows that the pristine material is SnO₂ with a tetragonal crystal structure. In Stage IV, Sn phases were mainly observed, as expected (Figure 3.4b). Blunt peaks at small angle measurements were believed to have originated from the remaining Li-Sn alloys. SnO and SnO₂ phases were not observed in the XRD pattern. The peak near 26° did not seem to have originated from the SnO₂ phase due to the fact that no other peaks belonging to SnO₂ were observed. No significant difference was observed between Stages IV and V (Figure 3.4c). The ambiguous peaks at small angles remained, but peaks related to the SnO or SnO₂ phases were not observed. The Sn peaks were smaller than those in Stage IV, but the significance of this finding was difficult to substantiate due in part to the effect of the experimental conditions on crystallization of the Sn material. Therefore, it was difficult to observe any distinctive new phase that may be associated with the extra capacity. It shows a limitation in bulk analysis thus draws attention to the potential for TEM analysis which allows local variations both in the structure and composition to be examined.

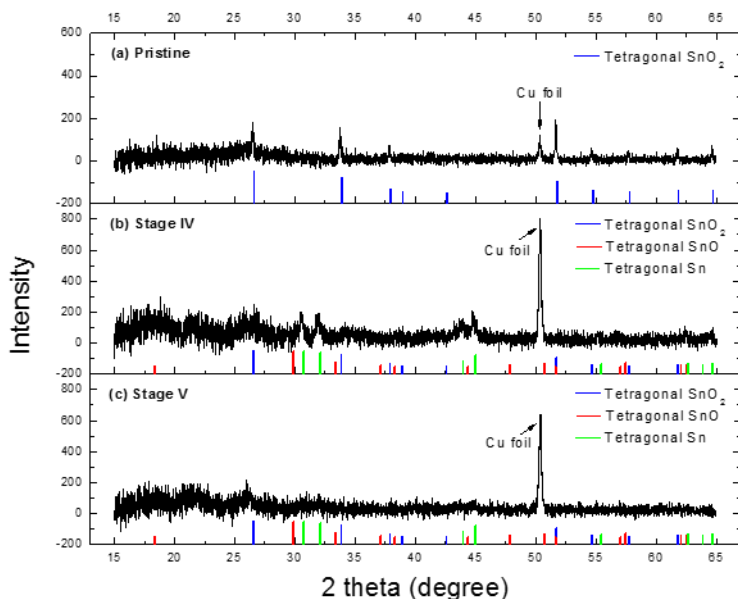


Figure 3.4. Ex situ X-ray diffraction (XRD) results for SnO₂ slurry electrodes at various discharge/charged stages. The SnO₂ slurry electrodes were discharged and charged in the coin cell toward specific voltage points of interest. XRD data were collected in the 2θ range of 15–65°, in 0.01° increments. (a) Pristine SnO₂ slurry electrode before being charged or discharged in the coil cell. The slurry electrodes were fully discharged and charged toward (b) the end of Stage IV (1 V) and (c) Stage V (2.5 V). The reference data for the related materials shown in the figures were obtained from the database of International center for diffraction data (ICDD): #00-041-1445 for tetragonal SnO₂, #04-005-4540 for tetragonal SnO, and #04-004-7747 for tetragonal Sn.

3.4.2. Ex situ TEM experimental procedure

Figure 3.5 provides a schematic diagram of the analysis method and the stages that were investigated in this work. We developed an *ex situ* TEM investigation technique which enables tracing same particles with an attempt to establish the electrochemical

reaction mechanism of the SnO₂ anode, improving and optimizing a recently introduced method.[68, 69] SnO₂ particles dispersed on a carbon film-coated copper TEM mesh grid were placed with the conventional SnO₂ slurry electrode in a coin cell. The SnO₂ particles were then charged and discharged directly on the TEM grid (Figure 3.5a). The SnO₂ particles on the TEM grid were expected to go through the same electrochemical process as the slurry electrode because the grid was comprised of copper metal, which is commonly used as a current collector for the anode in lithium-ion batteries. Additionally, the slurry electrode ensured the reliability of the electrochemical characterization because it had a sufficient amount of active materials for the acquisition of a credible electrochemical profile. We used the constant current–constant voltage (CC–CV) method to (dis)charge the grid-containing coin cell. It was driven slowly enough toward each major reaction stage to generate the same charge state between the grid and the slurry electrode. The cell was then disassembled to examine the SnO₂ particles using *ex situ* TEM after each reaction step, (dis)charging from the left boundary to the right boundary of each stage shown in Figure 3.5b, sequentially. The (dis)charged TEM grid was removed from the coin cell, gently washed with anhydrous DMC, and stored in a sealed vial filled with DMC. It should be noted that the DMC covered the TEM grid when the grid was loaded into a TEM chamber, and it protected the samples from exposure to air before TEM investigation. When investigating the particles by TEM, the electron beam was broadly spread to prevent high-energy electron beam damage. After TEM observations, the examined grid electrode and the slurry electrode were reassembled again in a coin cell, and the above processes were repeated to investigate subsequent states. Exploring phase evolution on the first full cycle by tracing

the same SnO₂ particles was facilitated with this approach.

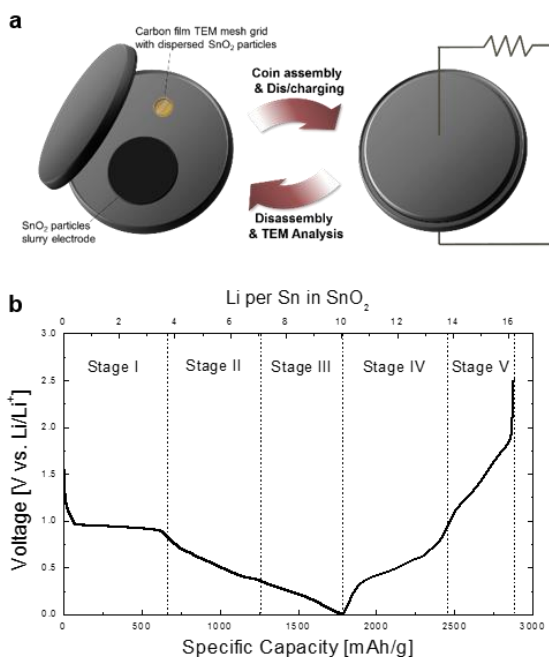


Figure 3.5. (a) Schematic diagram of the experimental technique for investigating the actual electrochemical reaction mechanisms of SnO₂ lithium-ion battery anode materials using *ex situ* TEM analysis. (b) Voltage vs. specific capacity profile, drawn in continuous form, of the first cycle of the SnO₂/Li battery, reproduced from Figure 3.1a. The division marks for Stages I to V indicate the states of charge investigated in this work.

Figure 3.5b shows the voltage profile of the first cycle of the SnO₂/Li battery in a continuous form; the investigated stages are marked as I to V. About 20 different locations were traced and examined in each TEM grid. The entire experimental procedure was repeated several times using other TEM grids to compensate for the limited accessibility of TEM on macroscopic phenomena as well as to account all statistical incidences, by observing differences between different regions. A statistical

Chapter 3. Extra capacity of SnO₂ anode in lithium-ion battery investigated by ex situ TEM analysis

chart of the indexed phases from all data is given in Table 3.2. Because the tracing grid electrode could not be protected from air exposure during the few seconds required for holder extraction from the transmission electron microscopy (TEM) system after the first investigation, we diversified the first cell-disclosure stage. Protection from air exposure was completely ensured during the first TEM investigation, for experimental reliability.

Chapter 3. Extra capacity of SnO₂ anode in lithium-ion battery investigated by ex situ TEM analysis

Table 3.2. Statistical chart of indexed phases from various experimental data from the SnO₂/Li battery. The number of investigated positions in which the material increased or decreased from the previous stage was counted for each investigated transmission electron microscopy (TEM) grid electrode sample. The ratio of the increased/decreased number of each material to the number of total investigated positions in one grid electrode sample is expressed as a fraction. The increment/decrement of the material in each stage is inferred by comparing the diffracted peaks and the intensities of the selected-area electron diffraction (SAED) patterns from the previous stage. The first TEM investigated stage was diversified to enhance the reliability of the experiment. The fractional numbers recorded for the first investigated stage of each sample indicate the proportions of the material present.

TEM grid No.	Material	Variation in stage I	Variation in stage II	Variation in stage III	Variation in stage IV	Variation in stage V
1	SnO(T)	0/24	+0/24	+0/24	+0/22	+3/22
	Sn(T)	21/24	+21,-3/24	-24/24	+7/22	+17/22
	LiOH(T)	0/24	+3/24	-2/24	+0/22	+9/22
	Li ₂ O(C)	0/24	+0/24	+24/24	+11/22	-15/22
	Sn(C)	0/24	+15/24	+9,-3/24	+3,-6/22	+13,-1/22
2	SnO(T)	0/19	+0/19	+0/18	+0/17	+2/16
	Sn(T)	19/19	+3,-16/19	-17/18	+13,-1/17	+9/16
	LiOH(T)	0/19	+5/19	+4,-4/18	+6,-1/17	+7/16
	Li ₂ O(C)	0/19	+0/19	+18/18	+1/17	-7/16
	Sn(C)	0/19	+7/19	+2,-2/18	-1/17	+0/16
3	SnO(T)	-	0/18	+0/18	+0/17	+2/16
	Sn(T)	-	18/18	+1,-17/18	+12/17	+5/16

Chapter 3. Extra capacity of SnO₂ anode in lithium-ion battery investigated by ex situ TEM analysis

	LiOH(T)	-	15/18	-15/18	+1,-3/17	+5,-1/16
	Li ₂ O(C)	-	0/18	+17/18	-3/17	-2/16
	Sn(C)	-	0/18	+14/18	-10/17	+1/16
	SnO(T)	-	-	0/20	+0/20	+3/20
	Sn(T)	-	-	20/20	+4,-5/20	+8,-1/20
4	LiOH(T)	-	-	18/20	-16/20	+2/20
	Li ₂ O(C)	-	-	0/20	+1/20	-1/20
	Sn(C)	-	-	0/20	+1/20	-1/20
	SnO(T)	-	-	-	0/22	+3/21
	Sn(T)	-	-	-	22/22	+8,-5/21
5	LiOH(T)	-	-	-	18/22	+1,-9/21
	Li ₂ O(C)	-	-	-	0/22	+0/21
	Sn(C)	-	-	-	0/22	+1/21
	SnO(T)	-	-	-	0/23	+0/23
	Sn(T)	-	-	-	23/23	+4,-1/23
6	LiOH(T)	-	-	-	22/23	-11/23
	Li ₂ O(C)	-	-	-	0/23	+0/23
	Sn(C)	-	-	-	0/23	+0/23

3.5. Phase evolution in the discharge process

Figure 3.6 shows a representative example of traces of the SnO₂ particles on discharging, recorded as TEM images and their associated selected area electron diffraction (SAED) patterns. Radial intensity profiles of the respective SAED patterns were also expressed to clearly show the phase evolution in each stage. Pristine SnO₂ particles dispersed on a carbon film-coated TEM grid are shown in Figure 3.6a. The particles were a few hundreds of nanometers in size. The SAED pattern of the pristine SnO₂ particles shows that the SnO₂ particles had a stable tetragonal crystal structure (Figure 3.6b and c). When discharged through a first large plateau from the initial state (Stage I), the particles divided into smaller sizes and became surrounded by gel-like layers (Figure 3.6d), forming a group. Crystalline SAED peaks were identified as tetragonal tin (Sn) metal, indicating that the SnO₂ particles were reduced to elemental Sn particles (Figure 3.6e and f). This is consistent with previous studies, which concluded that the conversion reactions (Equation 3.1.1 and 3.1.2) occur when the first plateau appears on the discharge curve at *ca.* 0.9 V.[39, 66] The gel-like layers evident in Figure 3.6d seem to be amorphous lithium oxide phases that appear as a broad background halo in the diffraction pattern.[42, 70] With further discharging through Stages II and III, the particles scattered into smaller particles, while the groups of particles became larger (Figure 3.6g and j).

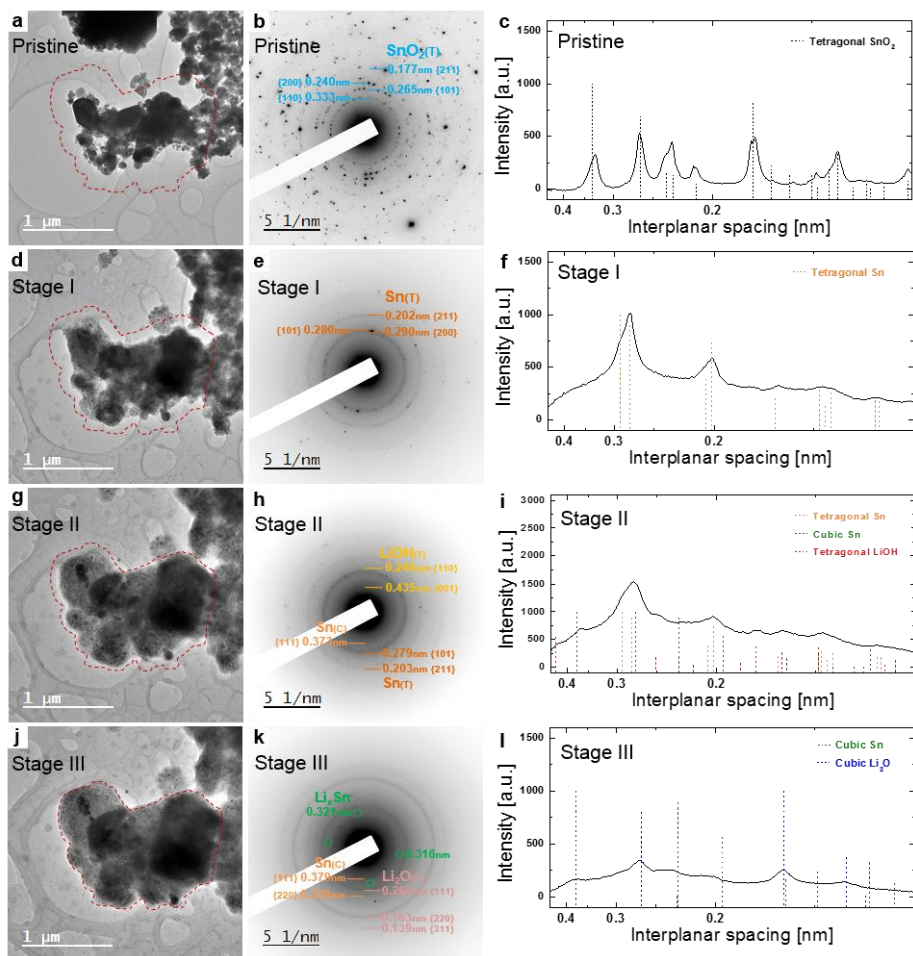


Figure 3.6. (a, d, g, j) TEM images of traced SnO₂ particles on the grid, (b, e, h, k) their corresponding SAED patterns, and (c, f, i, l) background removed radial intensities of the SAED patterns in (a, b, c) the pristine state, (d, e, f) Stage I, (g, h, i) Stage II, and (j, k, l) Stage III. (b, e, h, k) The letters in parentheses next to the chemical formulas in the SAED patterns indicate the crystal structures of the materials (T = tetragonal, C = cubic). (c, f, i, l) Interplanar spacing and the corresponding relative intensities of the reference materials are shown. The data from Table 3.4 were used as reference data.

This is easily recognized by comparing the red dashes shown on the TEM images. It is known that the insertion of lithium ions drives Sn particles to form Li_xSn alloys in Stages II and III.[39, 66] Sn peaks corresponding to the {200} and {101} planes (Figure 3.6e) gradually weakened and faded (Figure 3.6h and k), which is clearly seen in the radial intensity profiles (Figure 3.6f, i, and l). This suggested that lithium ions were being increasingly inserted into Sn particles, forming amorphous and partially crystalline Li_xSn alloys. Notably, we observed other diffraction peaks in these stages, i.e., circular patterns for cubic Sn, LiOH, and nano-crystalline cubic Li₂O. (Details of the phase indexing are described in Section 3.6.) These materials and the specific phases could have been formed when the TEM holder was exposed to air for a few seconds before the TEM grid was placed again in the air-blocking DMC liquid after the first investigation. Additional experiments systematically investigated this possibility, which revealed that LiOH and Li₂O were not created by the reaction in the air; LiOH was formed by normal electrolyte decomposition and Li₂O was simply the crystallized form of the already-existing amorphous phase that was generated from the conversion reactions (the details are explained in the following subsections.). The electron beam effects, e.g. electron energy-induced chemical reactions, damages or crystallization, were also examined, but it turned out that there was no significant electron beam effects on the samples in this experimental conditions (see Section 3.6.4). On the other hand, the changes in diffraction peak intensities from the cubic Sn were hardly differentiated. The presence of the cubic Sn phase during cycling of a Sn-based anode in lithium ion batteries was also reported in previous studies,[71-73] but further studies are required to clarify where the cubic Sn phase arose from. Still, it does not much affect this research

because it did not play a significant role in the extra capacity.

Meanwhile, it should be noted that most of the crystallization of the Li₂O occurred in Stage III, and some LiOH peaks that were observed in Stage II disappeared in Stage III, concomitantly. Considering that the formation reaction of Li₂O and LiH from LiOH is regarded as the origin of the over-capacity in the RuO₂/Li battery,[3] the same reaction could occur during discharge of the SnO₂/Li battery.

3.5.1. Inference on the source of LiOH phase

The LiOH phase was observed everywhere after Stage II, including the Sn/Li battery as shown in Figure 3.7; however, LiOH cannot be derived from the pure electrochemical reactions of SnO₂ or Sn with lithium ions in the absence of hydrogen. In addition, the oxygen element in LiOH also does not seem to come from the active materials, i.e., SnO₂ or Sn, because there is no oxygen element in the electrode components of Sn/Li battery. Nevertheless, LiOH was observable during the first TEM investigation which is prior to the first air exposure.

Thus, its formation was attributed to the ethylene carbonate/dimethyl carbonate (EC/DMC) electrolyte. Combined with the fact that LiOH is a common material formed by electrolyte decomposition,[74, 75] it was concluded that the electrolyte decomposition forming LiOH phase occurs below 0.8 V (vs. Li/Li⁺) and it easily adsorbs on the surface of the active materials during the electrochemical reaction cycles.

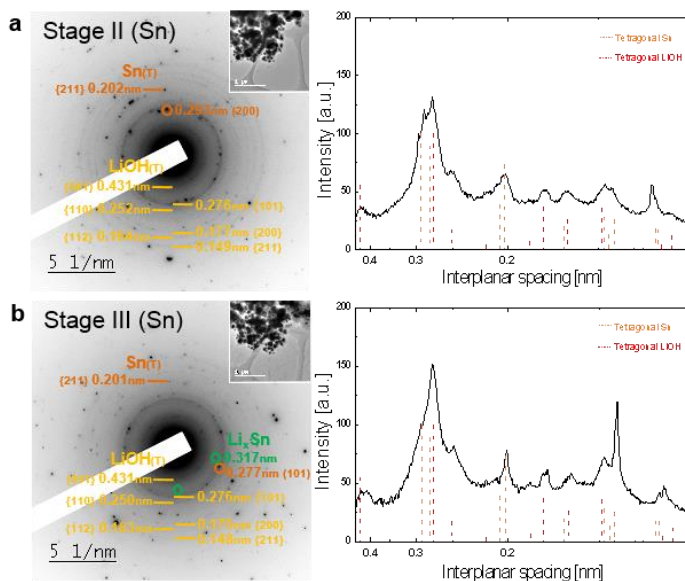


Figure 3.7. Representative example of the SAED patterns of trace Sn particles for (a) Stage II and (b) Stage III.

The removed background radial intensities of the SAED patterns are shown next to each pattern. Reference electron diffraction data of the indexed materials (from Table 3.4) are shown in each radial intensity graph.

3.5.2. Inference on the source of nano-crystalline Li₂O phase

The nano-crystalline Li₂O phase was observed only when the grid electrode was first investigated before Stage III, as shown in Table 3.2. The comparison of grid samples 1–3 with samples 4–6 in Table 3.2 clearly shows changes in the nano-crystalline Li₂O phase, resulting from the environmental conditions. To determine if it was formed in air, we compared the corresponding stages to those of the Sn/Li battery. Commercial Sn nano-powders were used for the investigation. The investigated stages are shown in Figure 3.8. The experimental procedure was same as that for the SnO₂/Li battery. We repeated the experiment several times for the reliability as shown in Table 3.3. As shown in Figure 3.7, the nano-crystalline Li₂O phase did not appear in the Sn/Li battery. The

rarity (or possibly absence) of the nano-crystalline phase is more conspicuous, considering the absence of the corresponding ring patterns. Therefore, we concluded that the nano-crystalline Li₂O phase was not created in air; instead, crystallization was induced in the existing Li₂O, which had already formed as a result of the conversion reaction of SnO₂.

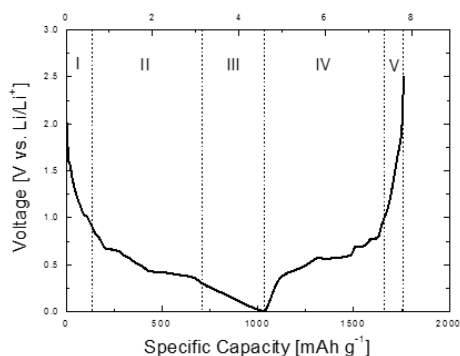


Figure 3.8. Voltage versus specific capacity for the first cycle of a Sn/Li battery in continuous form, reproduced from Figure 3.3. The division marks from I to V indicate the investigated states of charge. Each stage corresponds to the same voltage range as that used for the SnO₂/Li battery in this research.

However, it is noteworthy that the crystallization occurred only in Stage III. It raises other possible source for the Li₂O phase. Most of the LiOH phase in Stage II for the SnO₂/Li battery decreased in Stage III, simultaneous with the emergence of nano-crystalline Li₂O phase, as shown in Table 3.2; however, excluding the influence from some oxidized Sn materials initially contained in Sn/Li battery, the LiOH in Stage II for the Sn/Li battery did not decrease significantly in Stage III, as shown in Figure 3.7. This implies that the reaction of LiOH that results in formation of Li₂O and LiH phases, suggested by Hu et al., may occur only in SnO₂/Li batteries, not in Sn/Li batteries. In

Chapter 3. Extra capacity of SnO₂ anode in lithium-ion battery investigated by ex situ TEM analysis

other words, some of the nano-crystalline Li₂O phase observed in the discharge in the SnO₂/Li battery, as a possible source of the extra capacity, is attributable to the reaction between LiOH and Li₂O.

Table 3.3. Statistical chart of indexed phases from various experimental data from the Sn/Li battery. The chart is in the same format as Table 3.2. A detailed explanation of the table is provided in the caption to Table 3.2.

TEM grid No.	Material	Variation in stage I	Variation in stage II	Variation in stage III	Variation in stage IV	Variation in stage V
1	SnO(T)	-	0/18	0/18	+0/18	+5/18
	Sn(T)	-	18/18	-16/18	+5,-1/18	+2/18
	LiOH(T)	-	15/18	+6,-7/18	+4,-5/18	+4,-1/18
	Li ₂ O(C)	-	0/18	+0/18	+1/18	+0/18
	Sn(C)	-	1/18	-1/18	+0/18	+0/18
2	SnO(T)	-	0/11	+0/11	-	-
	Sn(T)	-	11/11	+3,-7/11	-	-
	LiOH(T)	-	6/11	+9,-2/11	-	-
	Li ₂ O(C)	-	0/11	+0/11	-	-
	Sn(C)	-	0/11	+0/11	-	-
3	SnO(T)	-	-	-	0/17	+1/17
	Sn(T)	-	-	-	17/17	+2,-3/17
	LiOH(T)	-	-	-	14/17	-6/17
	Li ₂ O(C)	-	-	-	0/17	0/17
	Sn(C)	-	-	-	3/17	+1/17

3.6. Details of phase indexing from SAED patterns

3.6.1. Identification of LiOH phase

The LiOH phase could be identified easily when the diffraction peaks were shown as perfect ring patterns. In that case, the LiOH phase could be identified by comparing the radial intensities of the SAED patterns with the interplanar spacings (d -spacing) and relative intensities of the reference data taken from Table 3.4.

However, it was more challenging if the peaks did not form clear ring patterns, such as those shown in Figure 3.6h. Because the d -spacing gaps among various materials become narrower as the d -spacing decreases, identifying the SAED peaks of high-index planes is difficult. For this reason, the peaks corresponding to the (001) planes ($d = 0.433$ nm) were distinct only among the Bragg planes of the LiOH material. Other low-index Bragg planes, such as the (101) ($d = 0.274$ nm) and (110) ($d = 0.251$ nm) planes, overlapped with the (107) planes of tetragonal Sn metal ($d = 0.280$ nm) (ICDD #04-007-3737), the (410) planes of tetragonal Li₂Sn₅ alloy ($d = 0.249$ nm) (ICDD #04-005-5077), and the (-103) planes of monoclinic LiSn alloy ($d = 0.250$ nm) (ICDD #01-071-9514). Nevertheless, they could be clearly indexed as the LiOH phase, because no other material has Bragg planes with a d -spacing close to 0.433 nm. The (101) planes of tetragonal LiSn have a d -spacing of 0.432 nm (ICDD #04-007-3737); however, other Bragg planes with intense reflection of LiSn, for instance, (103) ($d = 0.390$ nm) and (105) ($d = 0.333$ nm) planes, were not observed for any of the investigated points. Even if LiSn nanoparticles can only expose low-index Bragg planes, i.e. (101) planes ($d = 0.432$ nm),

Chapter 3. Extra capacity of SnO₂ anode in lithium-ion battery investigated by ex situ TEM analysis

most of the spot peaks at d -spacing of 0.433 nm still are considered to belong to LiOH phase because diffraction spots indicating 0.274 nm and 0.251 nm frequently appeared together with the spots at 0.433 nm in the absence of spot peaks at 0.333nm d -spacing. In this respect, the LiOH phase could be clearly indexed.

Table 3.4. Simulated electron powder-diffraction data in the form of tables for the Miller indices, interplanar spacings, and corresponding relative intensities. JEMS code was used for the simulation. Kirkland's atomic form factors were taken from simulations.[76] These data were utilized to index the SAED patterns obtained from this experiment. Crystal data were taken from the following ICDD files: #04-004-7747 for tetragonal Sn, #04-014-6265 for cubic Sn, #04-012-6191 for tetragonal LiOH, #04-001-8930 for cubic Li₂O, and #04-005-4540 for tetragonal SnO.

Sn (Tetragonal)								
(h,k,l)	d [nm]	Intensity	(h,k,l)	d [nm]	Intensity	(h,k,l)	d [nm]	Intensity
(2,0,0)	0.292	1000	(2,1,1)	0.202	736	(4,0,0)	0.146	134
(1,0,1)	0.279	897	(3,0,1)	0.166	203	(3,2,1)	0.144	259
(2,2,0)	0.206	392	(1,1,2)	0.148	285	(4,2,0)	0.130	184

Sn (Cubic)								
(h,k,l)	d [nm]	Intensity	(h,k,l)	d [nm]	Intensity	(h,k,l)	d [nm]	Intensity
(1,1,1)	0.375	1000	(1,1,3)	0.196	564	(1,3,3)	0.149	241
(0,2,2)	0.229	891	(0,0,4)	0.162	159	(2,2,4)	0.132	325

Chapter 3. Extra capacity of SnO₂ anode in lithium-ion battery investigated by ex situ TEM analysis

LiOH (Tetragonal)

(h,k,l)	d [nm]	Intensity	(h,k,l)	d [nm]	Intensity	(h,k,l)	d [nm]	Intensity
(0,0,1)	0.433	554	(1,0,2)	0.185	72	(0,0,3)	0.144	9
(1,0,1)	0.274	1000	(2,0,0)	0.177	372	(2,0,2)	0.137	15
(1,1,0)	0.251	175	(2,0,1)	0.164	73	(1,0,3)	0.134	12
(1,1,1)	0.217	42	(1,1,2)	0.164	262			
(0,0,2)	0.217	7	(2,1,1)	0.149	363			

Li₂O (Cubic)

(h,k,l)	d [nm]	Intensity	(h,k,l)	d [nm]	Intensity	(h,k,l)	d [nm]	Intensity
(1,1,1)	0.266	802	(0,2,2)	0.163	1000	(2,2,2)	0.133	10
(0,0,2)	0.230	1	(1,1,3)	0.139	378			

SnO (Tetragonal)

(h,k,l)	d [nm]	Intensity	(h,k,l)	d [nm]	Intensity	(h,k,l)	d [nm]	Intensity
(0,0,1)	0.484	61	(1,0,2)	0.204	10	(2,0,2)	0.149	73
(1,0,1)	0.299	1000	(2,0,0)	0.190	231	(1,0,3)	0.149	127
(1,1,0)	0.269	220	(1,1,2)	0.180	383	(2,1,2)	0.139	6
(0,0,2)	0.242	79	(2,0,1)	0.177	27	(1,1,3)	0.138	27
(1,1,1)	0.235	15	(2,1,1)	0.160	344	(2,2,0)	0.134	76

3.6.2. Identification of nano-crystalline Li₂O phase

The nano-crystalline Li₂O phase, observed in Figure 3.6k, was identified by comparing the radial intensities of the SAED patterns, with reference data taken from Table 3.4. The distinguishing ring patterns shown in Figure 3.6k are at interplanar spacings of 0.268, 0.163, and 0.139 nm in Figure 3.6l. These values are close to the interplanar spacings of the (111), (022), and (113) planes of cubic Li₂O from Table 3.4, of 0.266, 0.163, and 0.139 nm, respectively. Furthermore, among the peaks shown, the intensity of the ring pattern at 0.163 nm was remarkable and in good agreement with the simulated diffraction intensity shown in Table 3.4. Therefore, the Li₂O phases observed in the SnO₂/Li battery were confirmed.

3.6.3. Identification of tetragonal SnO phase

The interplanar spacing of the (101) planes of the tetragonal SnO material ($d = 0.299$ nm) is distinct among various materials containing lithium, tin, or oxygen. We observed crystalline peaks near 0.299 nm, as shown in Figure 3.11e, as a representative example. Because the nearest interplanar spacing among other possible materials is 0.292 nm for the (200) planes of tetragonal Sn, it seems that the crystalline peaks near 0.299 nm should be assigned to tetragonal SnO. However, due to deviation effects in the nano-crystal, we attempted to identify other peaks belonging to SnO to enhance the reliability. Most of the other peaks corresponding to the tetragonal SnO phase overlapped other materials; however, the peaks corresponding to the (200) plane at 0.190 nm were distinguishable.

Several peaks at 0.190 nm, belonging to the SnO phase, are shown in Figure 3.9, confirming the existence of the tetragonal SnO phase.

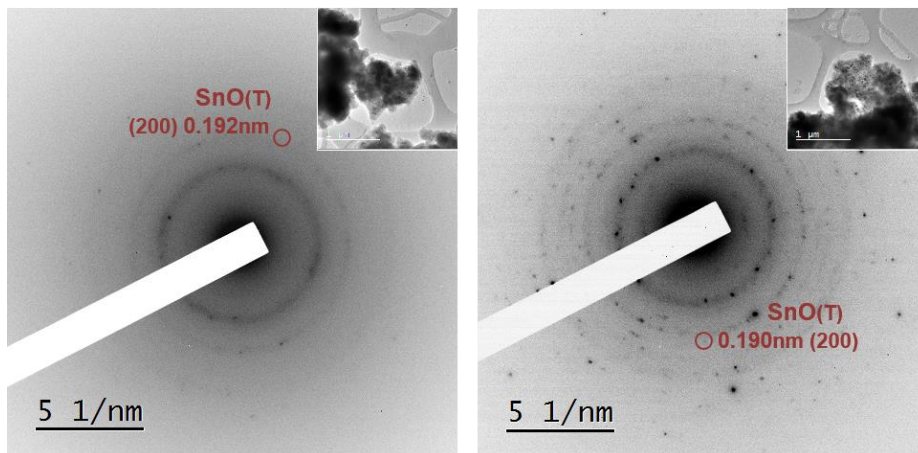


Figure 3.9. Two representative SAED pattern examples of trace SnO₂ particles for Stage V, which have crystalline peaks corresponding to the (200) plane of the tetragonal SnO phase. The relevant peaks are marked in the figures. The corresponding transmission electron microscopy (TEM) images of the SAED patterns are shown in the insets to the figure.

3.6.4. Examination of electron beam effect on filmy layers

Electron beam with 200 keV in TEM facilitates investigation in atomic levels, but its high energy occasionally induces damages on weak materials. The electron beam was broadly spread during TEM investigations to avoid the electron beam damage, but it still needs clear examination. In particular, LiOH and Li₂O are considered as the weakest materials in this research. Accordingly, we inspected the influences of the electron beam on LiOH and Li₂O phase by comparing consecutively acquired electron diffraction patterns. Figure 3.10 shows the SAED patterns, obtained in proper reaction stages from

Chapter 3. Extra capacity of SnO₂ anode in lithium-ion battery investigated by ex situ TEM analysis

the grid electrode samples where LiOH or Li₂O phase is visible, acquired successively for 15 seconds respectively. The testing conditions, e.g. condenser aperture size, magnification, beam spread degree, etc., were identical to the experimental conditions applied to this research. As seen in the SAED patterns, there are no changes observable between the first and second acquired patterns. It is obvious when comparing them by radial intensity profiles shown in Figure 3.10c and f; the two curves in each figure show nearly equal profiles. Those signify that the electron beam radiated during the experiments did not induce damage or transformation on the materials.

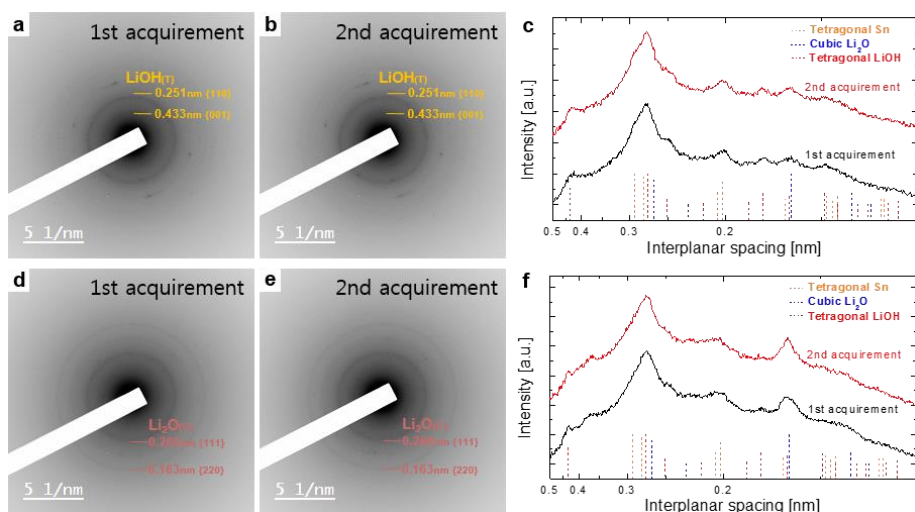


Figure 3.10. (a,b,d,e) SAED patterns acquired consecutively, for 15 seconds respectively, and (c,f) background removed radial intensity profiles of the SAED patterns. The SAED patterns obtained where (a,b) LiOH and (d,e) Li₂O are clearly visible respectively. (a,b,d,e) The contrast of the SAED patterns were inverted for better recognition. (c,f) Background radial intensities were removed using a power law. The *x*-axis was arranged in reciprocal form. There was almost no differences on the radial intensity profiles between the 1st and 2nd acquisition. It signifies that LiOH and Li₂O materials were hardly affected by TEM electron beam.

3.7. The unknown reactions in the charge process

3.7.1. Reactions of Li₂O phase as a major contributor to the extra capacity

A remarkable phenomenon was observed in Stage V. This is the key stage where the controversial reaction curve appears, noted as 'Reaction A' in Figure 3.1, and is generally considered the main source of the substantial extra capacity in the charge process. The nano-crystalline Li₂O peaks were much less intense during this stage (Figure 3.11). Because LiOH peaks reappeared in this stage to some extent, it could indicate the reverse formation reaction of Li₂O and LiH from LiOH, as suggested for the RuO₂/Li battery[3]. However, due to the insufficient consistency in repeated experiments, this effect cannot be fully supported and is not thought to mainly contribute to the additional capacity.

Importantly, the decrement in Li₂O was still consistent and reproducible whenever Li₂O was observed. Moreover, the diminished amount was sufficient to affect the extra capacity of the SnO₂/Li battery, which is clearly shown in Figure 3.11c; the intensity at the interplanar spacing of 0.163nm, where the most intense diffraction occurs in the electron diffraction for Li₂O phase (Table 3.4), was reduced by half according to the radial intensity profile. It amply reaches the additional capacity, if the most of the faded Li₂O was decreased with electron-participating reactions. Furthermore, it was the only notable change in this controversial stage and the only statistically meaningful difference from Sn/Li battery as well; therefore, the Li₂O-decreasing reaction should be the crucial contributor to the extra capacity, regardless of the relation with LiOH. Still, any other increased product comparable to the decreased amount of Li₂O was not detected further.

It may indicate that most of the additional lithium ions were extracted from Li₂O and it became lithium-deficient amorphous lithium oxide, similar to the mainstream idea for the nature of over-charge in lithium-manganese rich cathode materials.[77]

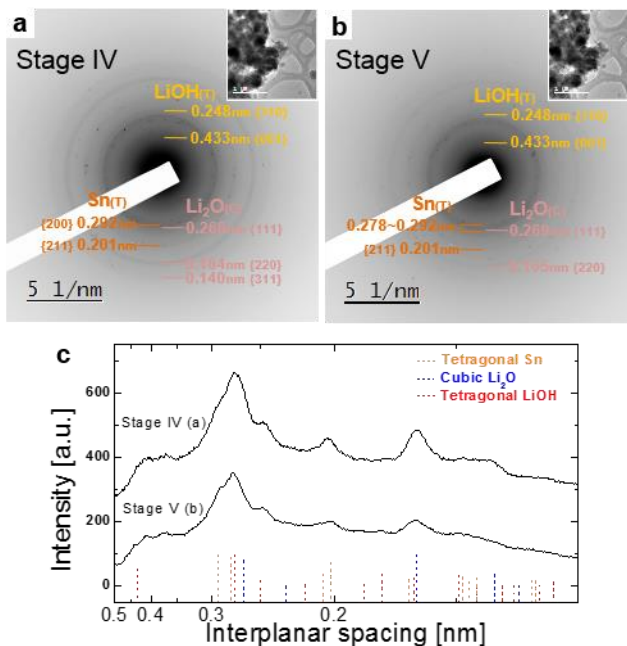


Figure 3.11. (a, b) A representative example of SAED patterns of traced SnO₂ particles from Stages IV and V and (c) background removed radial intensities of the SAED patterns. The example shows the decrement in Li₂O and slight increment in LiOH phases between Stages IV and V. The radial intensities were normalized for compensating the difference of acquisition times between the two SAED patterns. The corresponding TEM images of the SAED patterns at the recorded locations are shown in the inset to each figure.

To clarify the reaction of Li₂O in the controversial stage, we additionally performed electron energy-loss spectroscopy (EELS) experiments in Stage IV and V. Separate grid electrode samples, which were dis/charged straight from pure state to Stage IV and V

respectively, were used for the EELS measurements. EEL spectra were obtained in an energy-filtered TEM mode at an accelerating voltage of 80 kV to avoid electron beam damage on gel-like filmy layers. Representative experimental EEL spectra of Li and O *K*-edges in Stage IV and V are shown in Figure 3.12. (More spectra can be found in Figure 3.13.) The EEL spectra were acquired at the region where filmy layers were much more occupied than Sn-based bulky particles. We focused on the interpretation of the Li *K*-edge spectra, which would be directly affected by electron-participating reactions in lithium ion batteries, rather than the O *K*-edge spectra.

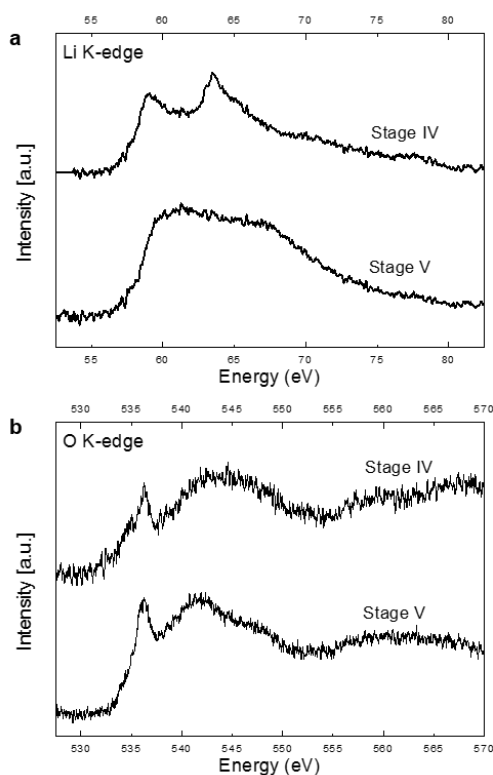


Figure 3.12. Experimental EEL spectra of (a) Li *K*- and (b) O *K*-edges in Stage IV and V. The EEL spectra were recorded in an energy-filtered TEM mode at an accelerating voltage of 80 kV. The spectra from Stage IV

and V were obtained from separate grid electrodes which dis/charged straight toward Stage IV and V respectively.

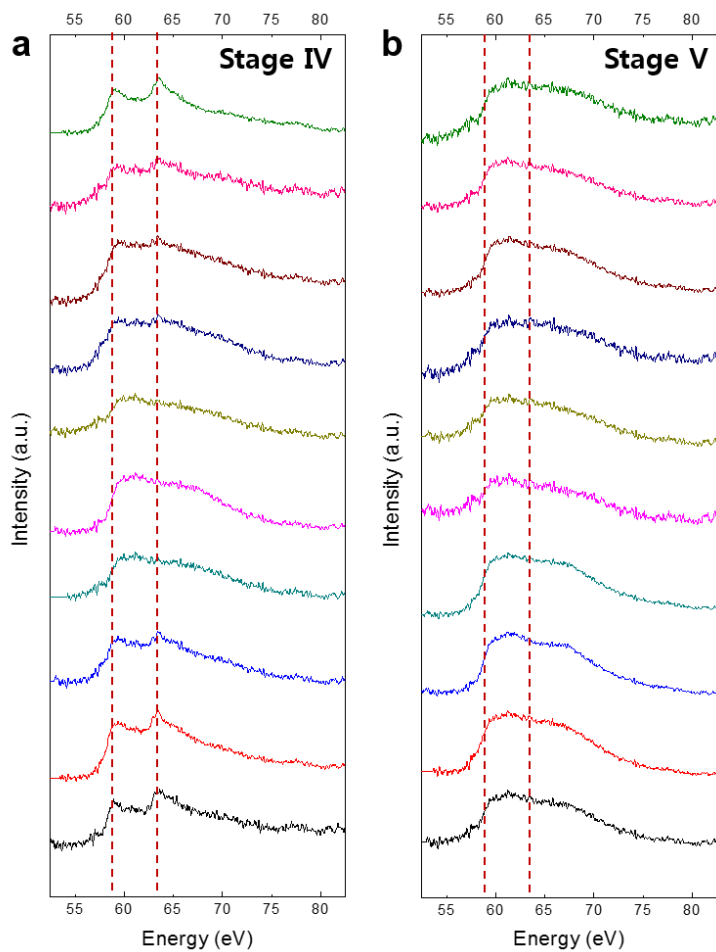


Figure 3.13. The collected experimental EEL spectra of Li *K*-edge in (a) Stage IV and (b) Stage V. The EEL spectra were recorded in an energy-filtered TEM mode at a 80 kV accelerating voltage. The spectra from Stage IV and V were obtained from separate grid electrode samples. Red dashed lines on both figures indicate the energy positions showing sharp peaks in Stage IV. (a) The EEL spectra show that most of them contain Li₂O phase in Stage IV. (b) The spectra in Stage V signify that Li₂O phase was transformed to other phase in this stage.

The experimental EEL spectra of Li *K*-edge from Stage IV are well matched with previously reported EELS or X-ray absorption spectroscopy (XAS) data of Li₂O phase.[78-80] Together with the result of electron diffraction study (Figure 3.11a), it clearly shows that most of the filmy layers in Stage IV are composed of Li₂O phase as expected. However, both Li (Figure 3.12a) and O *K*-edges (Figure 3.12b) changed in Stage V. The Li *K*-edge obtained in Stage V is distinguishable from Li₂O, LiH, LiOH or any possible linear combination of those.[79, 81, 82] (EEL spectrum of LiH was approximated to the imaginary part of calculated dielectric function using density functional theory due to the lack of database.) Considering Li *K*-edges of Li₂O and LiOH have very similar shape, EEL spectra in Stage V indicate that the major reaction in Stage V is not same as the case of RuO₂ electrode in which the reaction was explained as the formation of LiOH from Li₂O and LiH occurred.[3]

The clear difference in near edge structure of Li *K* reveals that transformation of Li₂O to other Li-containing phases occurred in Stage V. However, Li *K*-absorption edges of common Li-based electrolyte degradation products, e.g. Li₂CO₃ and LiF, do not correspond to the observed EELS.[83] It strengthens the validity of our suggestion that Li₂O may have delithiated itself instead of reacting with other materials, which was inferred from the electron diffraction experiment. Furthermore, the Li *K*-edge structure in Stage V does not show sharp peaks but rather blunt possibly because of atomic disordering caused by Li-extraction of Li₂O forming lithium-deficient amorphous lithium oxide. The atomic disordering in here is distinguished from amorphization of Li₂O from crystalline structure considering that Li₂O observed by EELS experiment in

Stage IV already had amorphous structure. It is because the grid electrode samples for EELS experiment were dis/charged straight to the corresponding stages from the pristine one and therefore the filmy layer has no chance to be exposed and crystallized in air. (Figure 3.14, which shows SAED patterns obtained in the same experimental condition with the EELS measurement, confirms that Li₂O already had amorphous structure in Stage IV during the EELS experiment)

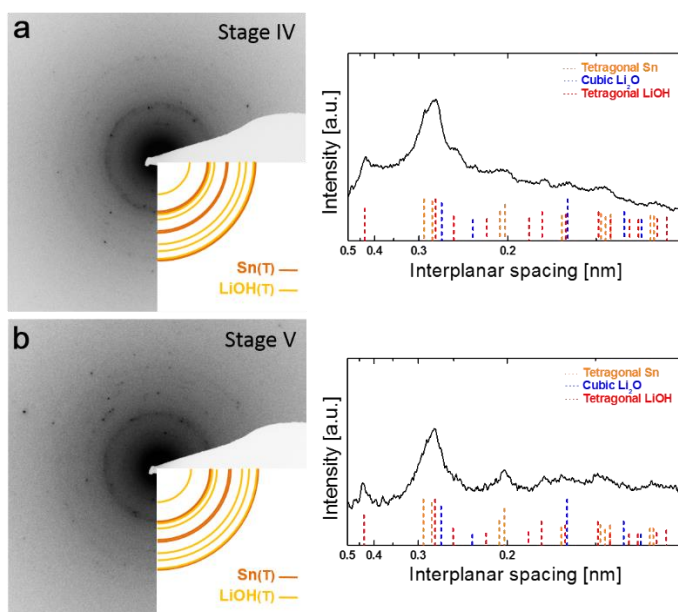


Figure 3.14. An example set of SAED patterns obtained in the same experimental condition with the EELS measurements using 80 kV TEM instrument (Titan G2 Cube 60-300, FEI). The SAED patterns were obtained from the TEM grid electrodes dis/charged straight toward (a) Stage IV and (b) V each. Therefore, the samples had no chance to be exposed and crystallized in air. Background removed radial intensity profiles are also expressed on the right side of each SAED pattern. Nano-crystalline Li₂O phase is not observable due to its amorphous structure. It confirms that Li₂O was already exist in amorphous structure during the EELS measurement in Stage IV and V.

In addition, the near edge structure of Li-K in Stage V could be simulated by assuming co-existence of various Li-deficient lithium oxide. The first principles calculations based on density functional theory were carried out using Vienna Ab initio Simulation Package (VASP) pseudopotential code to understand the different features of EEL spectra between Stage IV and V.[84] We used the functional based on the generalized gradient approximation (GGA) for the exchange-correlations and projector augmented-wave (PAW) method for descriptions of core electrons. Spin-polarized calculations were performed for the system with odd-number electrons. Amorphous phase was approximated to crystalline phase when constructing Li-deficient lithium oxide structure, i.e., several numbers of Li atoms were artificially extracted from the perfect cubic Li₂O unit cell and the cell was periodically arrayed. Then, cell volume and shape as well as all internal atomic coordinates were relaxed by minimizing the Hellmann-Feynman forces less than 0.2 eV/nm. The Fermi-level was aligned by simply locating it in the middle of a band gap. The partial density of states (PDOS) calculations results are shown in Figure 3.15.

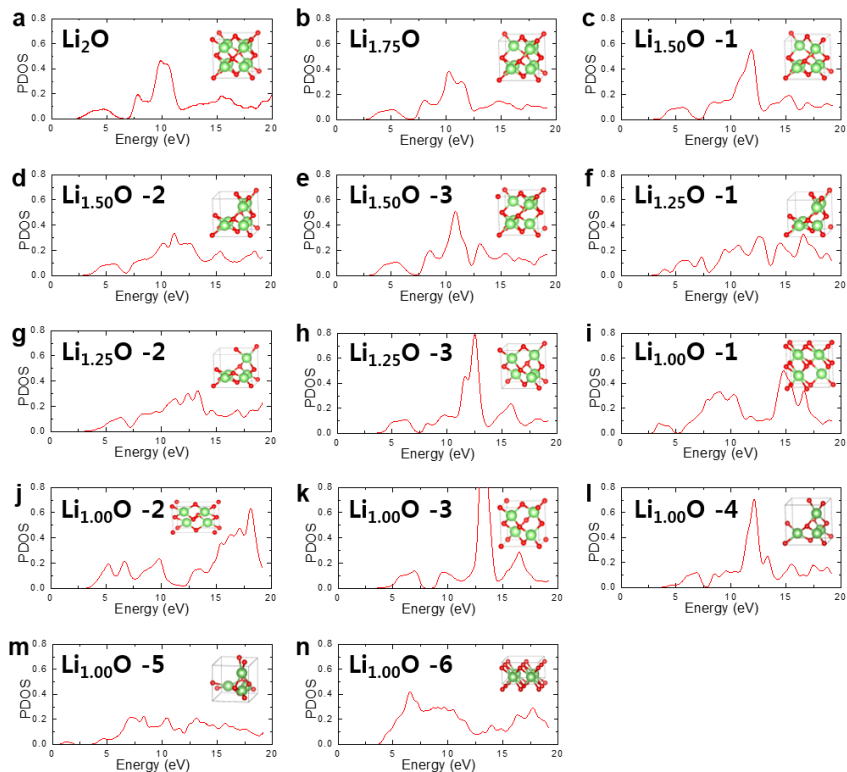


Figure 3.15. Li-p conduction band partial density of states (PDOS) calculation results of (a) cubic Li₂O and (b-n) various Li-deficient lithium oxide. Corresponding numbers of Li atoms were extracted from the unit cell of the cubic Li₂O phase to realize lithium-deficient lithium oxide. All possible configurations of Li atoms were considered for each Li_xO phase (x=1.00, 1.25, 1.50, 1.75). Relaxed structures of each Li_xO phase were shown as insets in each figure. The Fermi-levels were aligned in the middle of each band gap.

Figure 3.16 shows the experimental EEL spectra of Li *K*-edge and the Li-p unoccupied PDOS calculation results together.[14] The smoothed PDOS curves were also displayed to estimate practical curves which can be obtained from the EELS experiments. As shown in Figure 3.16a, the calculated Li-p conduction band PDOS of Li₂O agrees with the experimental Li *K*-edge EEL spectrum, which was already confirmed to Li₂O phase on the basis of other previous reports. In fact, the PDOS

calculations did not consider core-hole effect and practical exceptional cases of dipole selection rule, which could be included in the experimental EELS spectra. Nevertheless, the PDOS calculation results described approximate EELS spectra. It shows the validity of the EELS simulation of this system.

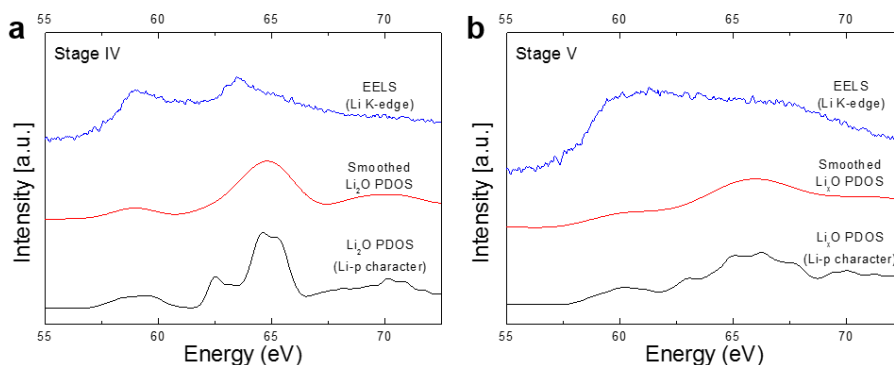


Figure 3.16. The experimental EEL spectra of Li K-edge obtained in (a) Stage IV and (b) Stage V compared with Li-p orbital partial density of states (PDOS) calculation results. Blue, black, and red curves indicate the experimental EELS spectra, the calculated Li p-character PDOS, and smoothed PDOS by fast fourier transform (FFT) filter, respectively. The smoothed PDOS curves show the predicted practical curves that can be obtained from the EELS experiment. (a) Li₂O PDOS curve is identical to the PDOS from Figure 3.15a. (b) Li_xO PDOS indicates the averaged PDOS of various Li-deficient Li_xO phase ($x=1.00, 1.25, 1.50, 1.75$), which are shown in Figure 3.15b-n.

Li_xO PDOS in Figure 3.16b indicates the averaged Li-p orbital PDOS of various Li-deficient lithium oxide ($x=1.00, 1.25, 1.50, 1.75$) which are shown in Figure 3.15. The various PDOS with same x -values that have originated from different configurations of Li atoms were averaged to a single PDOS in advance, respectively. Subsequently, the

resulted four PDOS of Li_xO (one for each x-value, i.e. x=1.00, 1.25, 1.50, 1.75.) were finally averaged to the Li_xO PDOS black line curve. The averaged PDOS of Li-deficient lithium oxide showed positive shift of the onset and lost distinct sharp peaks, which is comparable to the experimental EELS spectrum obtained in Stage V. It supports the possibility of the Li-extraction from Li₂O in Stage V. Thus, the electron diffraction and the EELS studies with PDOS calculations signify the same conclusion of the major contributor to the extra capacity, which is the Li-extraction from Li₂O resulting in the formation of Li-deficient amorphous lithium oxide.

3.7.2. An assessment of the possibility of the reverse conversion reaction

The appearance of tetragonal SnO phase in the Stage V as shown in Figure 3.17a and b may suggest the possibility that a portion of the decreased Li₂O is transformed into the re-formation of the SnO phase. However, it was only little amount as to mainly attribute to the additional capacity (Table 3.2). The SnO phase was observed about 11 % in the examined positions in which merely one or two SnO peaks among scores of Sn peaks for each counted position. Therefore, it is reasonable to conclude that the appearance of the SnO phase is irrelevant to the extra capacity of the SnO₂/Li battery.

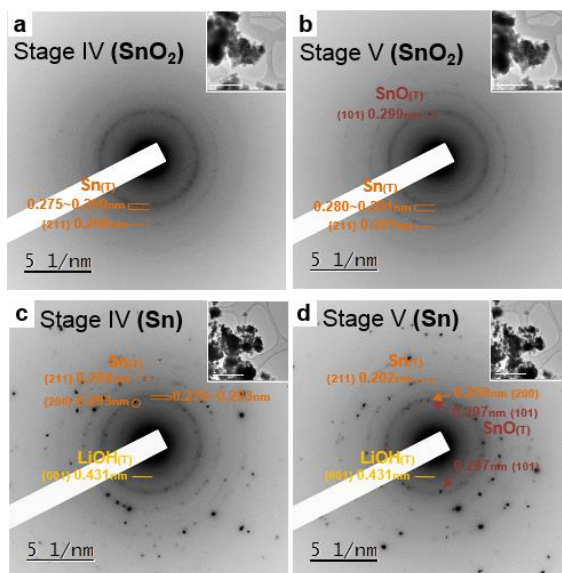


Figure 3.17. Representative SAED patterns of trace (a, b) SnO₂ and (c, d) Sn particles showing the emergence of the SnO tetragonal phase between Stage IV and V. The contrast in the SAED patterns was inverted, and the indexed materials were marked on the SAED patterns together with Miller indices and interplanar spacing. The corresponding TEM images of the SAED patterns are shown in the inset to each figure.

Furthermore, the SnO phase was also observed at a similar level in Sn/Li batteries where extra capacity is not observed (Figure 3.17c and d). Even though the Li₂O phase may also exist in the Sn/Li battery, due to electrolyte decomposition, the amount is much less than that in the SnO₂/Li battery. This indicates that the SnO phase observed in the SnO₂/Li battery have not originated from the reverse conversion reaction of SnO₂, which describes the reaction between Sn and Li₂O; instead, most of the re-formed SnO phases may have resulted from the reaction of Sn with neighboring oxygen that originated from electrolyte decomposition. The tetragonal SnO₂ phase was not observed for any of the investigated points, neither in the SnO₂/Li nor Sn/Li battery. In addition, shape change of Li *K*-edge EEL spectrum (Figure 3.12) supports that reactions other than the reverse

conversion reaction preferentially occur in Stage V considering that the reverse conversion reaction do not cause any structural changes of lithium-containing compounds, which simply leads to the total amount decrement of Li₂O. Those explain that the reverse conversion reaction of SnO₂ does not seem to be possible in the actual battery-operating environment, and accordingly, it is not a major contributor to the additional capacity, in contrast to the previous reports.

3.8. Summary

In summary, we developed an *ex situ* TEM process to examine the electrochemical reactions in a real battery system. The research provided several important new findings. First, we demonstrated that the origin of the additional capacity of the conventional SnO₂ anode material in lithium-ion batteries is related to the reaction of the Li₂O phase. The majority of additional lithium-ion extractions on the charge are derived from the Li₂O, which may possibly accompany the formation of lithium-deficient amorphous lithium oxide. Additionally, it is probable that the origin of the extra capacity in the RuO₂/Li battery also partly contribute to that in the SnO₂ anode, although the two battery systems have different electrochemical reaction mechanisms; the Li₂O phase is participating and part of Li₂O may be attributable to the reaction with LiOH during the charge and the discharge processes. Second, we observed only few reversed SnO phases and hence were unlikely major contributors to the extra capacity. More importantly, the SnO₂ phase did not reappear at all. It indicates that the reverse conversion reaction is scarcely possible in the conventional SnO₂ particle electrodes under the actual battery-operating

Chapter 3. Extra capacity of SnO₂ anode in lithium-ion battery investigated by ex situ TEM analysis

environment. The overall phase evolution of the SnO₂/Li battery investigated in this study is summarized in Table 3.5. This research provides a better understanding of the long-debated issues of the promising SnO₂ lithium-ion battery anode material. Moreover, the experimental scheme presented in this work may provide insight for future TEM analysis strategies in the field of battery science.[85]

Table 3.5. A summary of phase evolution of SnO₂ anode material in lithium-ion batteries. Significant phase changes are written on each stage.

Stage	Phase evolution of SnO ₂ anode
Stage I	Sn + Li _x O(amorphous)
Stage II	Li _x Sn + Sn(decreased) + Li _x O(amorphous) + LiOH(electrolyte decomposition)
Stage III	Li _x Sn + Li ₂ O + LiOH(decreased)
Stage IV	Sn + Li ₂ O + LiOH(not changed)
Stage V	Sn + Li ₂ O(much decreased) + Li _x O(amorphous) + LiOH(increased in some) + SnO(reacted with floating oxygen)

Chapter 4

***In situ* TEM investigation on lithiation mechanism of tunnel-structured α -MnO₂ nanowire**

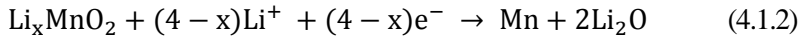
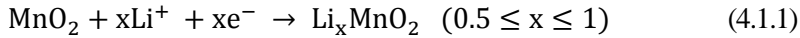
4.1. Introduction

Manganese oxides, which are low cost and environmentally friendly, have been considered as attractive materials for new-generation lithium-ion battery electrodes.[86-88] In particular, α -MnO₂ has a unique [2×2] tunnel structure that is stable in a nanowire configuration and allows easy insertion/extraction of lithium ions, a significant benefit for a lithium-ion battery electrode material.[89-91] This efficient tunnel structure, or cryptomelane-type structure, also exists in other kinds of oxide materials such as titanium,[92] vanadium,[93] tin,[94] and chromium-based oxides,[95] which have a wide range of applications besides lithium-ion batteries. It is generally thought that the tunnels play an important role in fast ionic diffusion; however, lithium-ion diffusion behavior in a single nanowire has not been widely studied.[89, 96, 97]

In addition, the α -MnO₂ material has an advantage on its wide applicability as the lithium-ion battery electrode material. The α -MnO₂ material can be used for both of the

Chapter 4. In situ TEM investigation on lithiation mechanism of tunnel-structured α -MnO₂ nanowire

cathode and anode materials because of its two step reaction mechanism. It is generally known that the α -MnO₂ materials react with lithium ions by two different mechanisms, insertion reaction and conversion reaction, as written below.



Because it is generally believed that lithium ions can be easily inserted and extracted through the empty [2×2] tunnels, Equation 4.1.1 is called insertion reaction, which is thought to be reversible without severe structural deformation. Due to the high voltage range of the reaction 4.1.1, over 1 V versus Li/Li⁺, this insertion reaction makes the α -MnO₂ material applicable to the cathode material in lithium-ion batteries. On the other hand, Equation 4.1.2 accompanies severe structural transformation extruding the manganese elements from the strong bonding with oxygen ions, which is thus called conversion reaction. The conversion reaction is very common in the transition metal oxide material as an example was already shown in SnO₂ anode material of Chapter 3. Because the conversion reaction generally occurs under 1 V (vs. Li/Li⁺), the materials experience this reaction is usually utilized as anode materials in lithium-ion batteries, which is the reason why the MnO₂ material also can be used for the anode material.

However, there is still lack of understanding on the detailed reaction mechanism of α -MnO₂ material in the lithium-ion batteries. There have been several researches that provided more information on the reaction mechanism of α -MnO₂ material. For examples, the positions of lithium ions in the tunnels were investigated by DFT calculations,[89, 98] the asynchronous tunnel expansion was suggested by *in situ* TEM experimental results,[97] and conversion reaction without any intermediate phases was

Chapter 4. In situ TEM investigation on lithiation mechanism of tunnel-structured α -MnO₂ nanowire

argued based on X-ray diffraction studies.[99] Nevertheless, it is still not understood how lithium ions are inserted and how MnO₂ structure is gradually transformed into Mn and Li₂O phase at last. The understanding on the structural evolution of the material is essential for the full explanation on the reaction mechanism.

Here, we investigated lithiation mechanism in a single α -MnO₂ nanowire by *in situ* transmission electron microscopy (TEM). *In situ* TEM studies are one of the best approaches for investigating electrochemical reaction mechanisms at the nano-scale, realizing an open battery cell and enabling direct observations of structural evolution with a bias voltage applied to the TEM instrument.[17] First, we identified the fastest electrochemical lithium-ion diffusion path of the cryptomelane-type structured nanowire with *in situ* TEM observations. By setting up a specific environment that allows comparison of probable lithiation channels, it was verified that lithiation through the longitudinal [2×2] tunnels is more favorable than penetration through the side wall of the nanowire. In addition, we identified the lithiation mechanism of α -MnO₂ electrode material by comprehensive *in situ* TEM analysis. By systematically interpreting fast Fourier transformed (FFT) pattern analysis from high-resolution TEM images, selected area electron diffraction (SAED) pattern, and electron energy loss spectroscopy (EELS) results taken during the *in situ* TEM experiment, we could track the structural evolution of α -MnO₂ nanowire and reveal how the pristine MnO₂ structure gradually transforms into Mn and Li₂O phases during the lithiation procedure. Moreover, we observed the formation of MnO intermediate phase during the conversion reaction. This work provides fundamental understanding on the reaction mechanism of the tunnel-structured α -MnO₂ nanowire in the lithium-ion battery, which can be applicable to both of the

cathode and the anode material.

4.2. Experimental details

4.2.1. Material synthesis and characterization

Tunnel-structured alpha (α) phase manganese dioxide (α -MnO₂) nanowires, also named cryptomelane- or hollandite-type manganese dioxide material, were synthesized using an aqueous hydrothermal redox reaction using potassium persulfate as an oxidant[100-102]. In a typical synthesis, manganese sulfate monohydrate (Mn(SO₄)H₂O), potassium sulfate (K₂SO₄), potassium persulfate (K₂S₂O₈), and purified water were combined in a polytetrafluoroethylene (PTFE)-lined pressure vessel and heated at 220°C for 2 days. The resulting solid was washed, filtered, and dried. Then, the dried solid material was ground and annealed at 400°C for 2 hours (2°C/min heating rate). Powder X-ray diffraction (PXRD) pattern of the sample was obtained with a Rigaku Ultima IV X-ray diffractometer. Cu K α radiation ($\lambda = 0.15406$ nm) was used with Bragg-Brentano focusing geometry.

4.2.2. *In situ* TEM measurement

For the *in situ* TEM experiments, potassium-doped α -MnO₂ nanowires were dispersed in acetone and dropped onto a carbon-support-film-coated copper mesh TEM half-grid as the working electrode. Lithium metal was coated onto a sharp tungsten tip

as the counter electrode, conducted in an argon-filled glove box to prevent excessive oxidation of the lithium metal. The nanowire-dispersed TEM half-grid and the lithium-coated tip were loaded into a Nanofactory TEM-scanning tunneling microscope (STM) specimen holder in the argon-filled glove box, and the holder was then transferred into a TEM instrument using a sealed bag. Upon brief (~5 s) exposure of the specimen holder to air during transfer into the TEM column, a thin Li_xO layer naturally forms on the lithium metal, which acts as a solid electrolyte. The contact between the Li_xO layer and the potassium α -MnO₂ nanowires (or the carbon support film) was formed in the TEM instrument using the STM unit. A constant negative voltage bias (less than 1 V) was applied to cause electrochemical lithiation in the nanowires. There was no current flow before applying the voltage bias.

4.3. Structural characterization of α -MnO₂ nanowire

Before the *in situ* TEM experiment, we confirmed the tunneled structure of the manganese oxide nanowire material. The powder X-ray diffraction (PXRD) pattern of the synthesized sample is shown in Figure 4.1a. All diffraction lines can be indexed to the tunnel-structured alpha phase of manganese dioxide with potassium dopants (K_xMn₈O₁₆, JCPDS 029-1020). The atomic model structures of the ideal potassium α -MnO₂ material (K₂Mn₈O₁₆), along the <100> and <001> axes are shown in Figure 4.1b and 1c. Eight MnO₆ octahedrons constitute a [2×2] tunnel and potassium ions are positioned at the center of the tunnels making the structure stable. The tunnel structure was well aligned along the [001] direction, which is clearly shown in the TEM images

Chapter 4. In situ TEM investigation on lithiation mechanism of tunnel-structured α -MnO₂ nanowire

(Figure 4.1d–h). Figure 4.1d shows that the material was well synthesized as a nanowire structure with a clean, smooth surface. The nanowires were several micrometers long and less than 50 nm wide. Furthermore, the nanowires had an entirely crystalline cryptomelane-type tunnel structure from core to surface, as shown in the high-angle annular dark field (HAADF) scanning TEM (STEM) image (Figure 4.1e) and its fast Fourier-transformed (FFT) pattern (Figure 4.1f). The magnified atomic resolution HAADF-STEM images along $\langle 100 \rangle$ (Figure 4.1g) and $\langle 001 \rangle$ (Figure 4.1h) axes confirm the cryptomelane-type structure of the nanowires. The atomic images well match with the atomic model structure. The K/Mn ratio of the synthesized material was measured to be 0.101 by inductively coupled plasma optical emission spectroscopy (ICP-OES), which defines the formula unit as $\text{K}_{0.8}\text{Mn}_8\text{O}_{16}$.

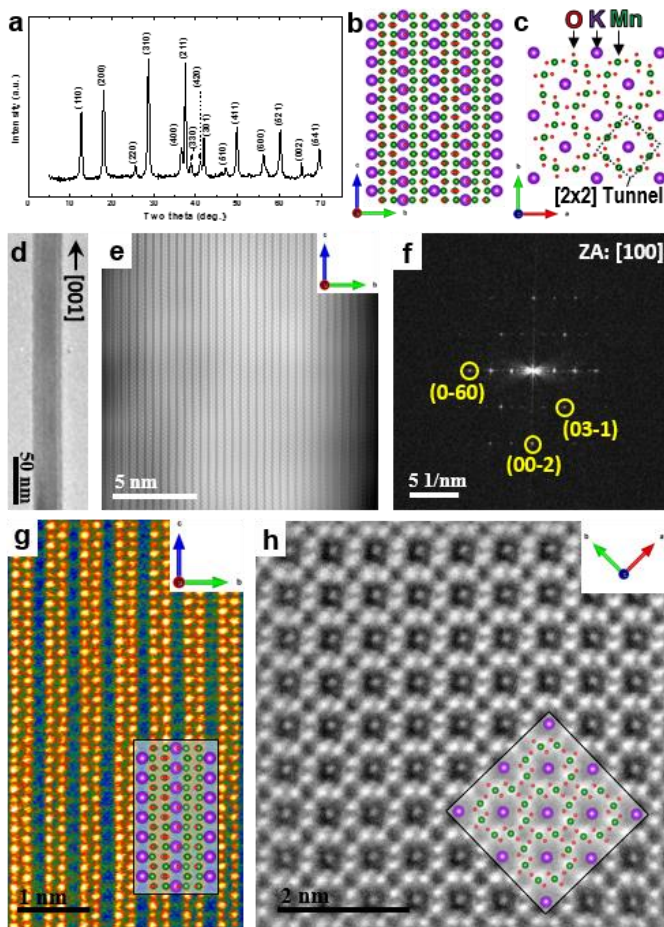


Figure 4.1. Crystallographic structural information of pristine potassium α - MnO_2 nanowire material. (a) PXRD pattern of potassium α - MnO_2 nanowires. (b, c) Atomic model structures of $\text{K}_2\text{Mn}_8\text{O}_{16}$ along the (b) $\langle 100 \rangle$ and (c) $\langle 001 \rangle$ zone axes. One $[2 \times 2]$ tunnel is indicated with a red dashed box. (d) TEM image of a single potassium α - MnO_2 nanowire. (e) HAADF-STEM image of a single nanowire along the $\langle 100 \rangle$ zone axis and (f) its FFT pattern. Corresponding planes of diffraction spots are described on the FFT pattern. (g, h) Atomic-resolution HAADF-STEM images of the nanowire along the (g) $\langle 100 \rangle$ and (h) $\langle 001 \rangle$ zone axis. The images were filtered by the inverse FFT method. Atomic model structures of potassium α - MnO_2 ($\text{K}_2\text{Mn}_8\text{O}_{16}$) are shown on each image.

4.4. Actual lithiation path in a tunnel-structured α -MnO₂ nanowire

To investigate the electrochemical lithiation path in the potassium α -MnO₂ nanowire in a real battery cell, we applied the *in situ* TEM experimental technique developed by F. Wang *et al.* for direct observation of the electrochemical reactions of nanoparticles.[103] Conventionally, *in situ* TEM measurements on battery electrodes have been performed by making direct contact between an Li_xO-coated lithium tip and the endpoint of a nanowire, and forcing lithiation along the longitudinal direction of the nanowire as illustrated in Figure 4.2.[17] This method has the advantages of clear recognition of the reaction front and control of the reaction, but ignores other lithium-ion diffusion paths away from the longitudinal direction. It is possible that lithium ions diffuse more easily through the lateral direction from the side wall of the nanowire in a real battery cell environment; that is, the electrolyte covers the whole surface of the nanowires as shown in Figure 4.3.

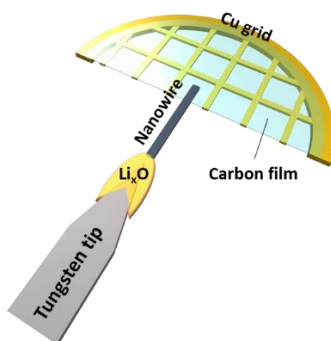


Figure 4.2. Schematic illustration of the conventional *in situ* TEM experimental setup for the observation of lithiation into the nanowire materials.

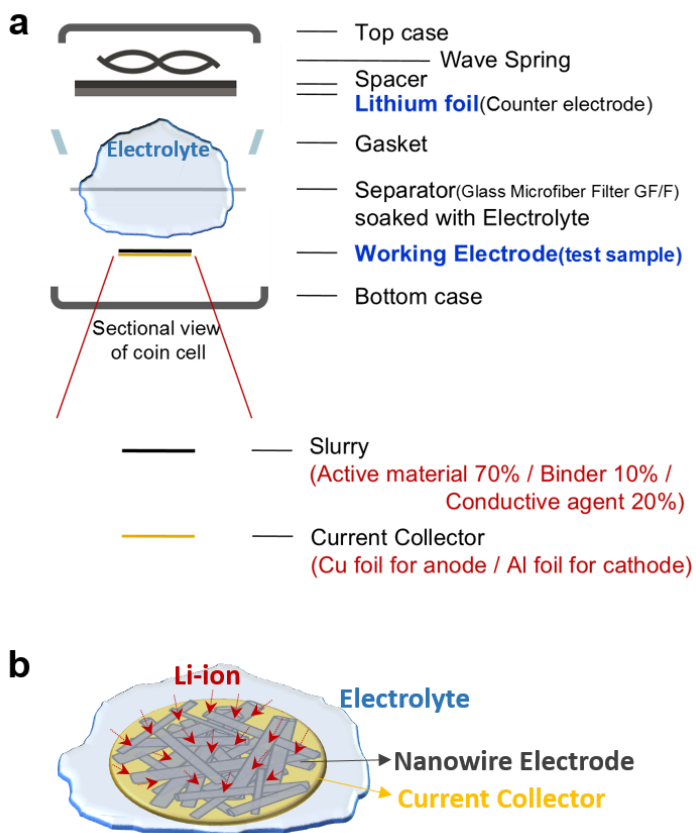


Figure 4.3. (a) Schematic illustration of the configuration of a coin cell battery at the cross-sectional view. (b) Schematic illustration of the working electrode environment with nanowire electrode materials.

Owing to the $[2 \times 2]$ tunnel structure, the direction along the tunnels has been regarded as the fastest lithium-ion diffusion path for cryptomelane-type materials including potassium α - MnO_2 nanowires; however, this has never been proved. To examine the possibility of lithiation along the lateral direction, a contact was formed between the Li_xO tip and a conductive carbon support thin film instead of a nanowire, as shown in Figure 4.4a. In this configuration, lithium ions are first diffused through the conductive amorphous carbon and then encounter the nanowires when the electrical bias is

Chapter 4. In situ TEM investigation on lithiation mechanism of tunnel-structured α -MnO₂ nanowire

applied.[103, 104] Li_xO was attached to the conductive carbon film close to the middle of the nanowires laid perpendicular to the Li_xO tip, using an *in situ* nano-manipulator in the TEM instrument, as shown in Figure 4.4b. After biasing, lithium ions should reach the side wall of the nanowire much earlier than the endpoint, given that lithium ions are expected to diffuse almost uniformly along the radial direction of the amorphous carbon film. However, it was observed that the contrast movement and volume expansion, both of which strongly correlate with lithium-ion diffusion, proceeded very quickly (85 nm in 4 seconds) along the longitudinal direction from the upper to the lower region, and rapid volume expansion from the middle of the nanowires closest to the lithium source was not observed (Figure 4.4c–h). This implies that the longitudinal tunnels are the fastest lithium-ion diffusion paths for cryptomelane-type nanowires. Given that lithium ions did not penetrate the nearest side wall of the nanowires, it is likely that they were inserted into the nanowire, shown in orange in Figure 4.4i, from the endpoint shown in the inset of Figure 4.4b. However, the blue-colored nanowire in Figure 4.4i, which does not have a close endpoint, also expanded (Figure 4.4i and j), implying that lithium ions can pass through the side wall and diffuse laterally, even though this mechanism is slower and more difficult than diffusion through the longitudinal tunnels from the endpoint. The lithium-ion diffusion in the α -MnO₂ nanowires is illustrated in Figure 4.5.

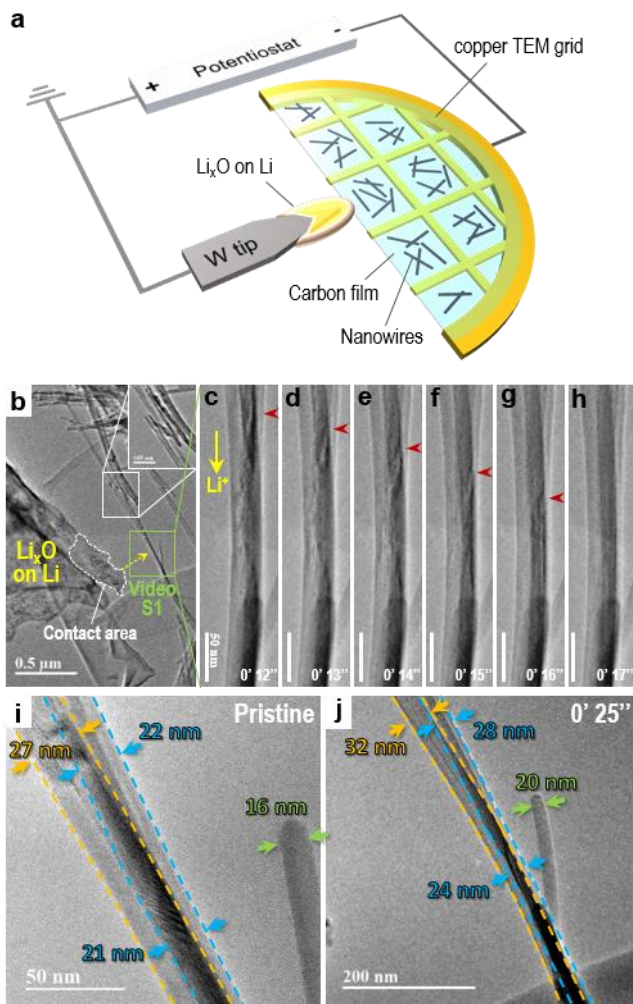


Figure 4.4. In situ TEM experiment for identifying actual lithiation paths in α - MnO_2 nanowire material. (a) Schematic diagram of in situ TEM experiment for investigation of the preferred Li-ion diffusion path in potassium α - MnO_2 nanowires. (b) A low-magnification TEM image of the in situ experiment, which was taken before applying a bias voltage. Nanowires are laid on carbon support film and Li_xO is in contact with the upper side of the carbon support film. The starting point of the nanowire is shown enlarged in the inset. The green box indicates the region recorded in real-time video, as well as the region shown in (c–h). The contact area between the Li_xO and the carbon support film is designated by a closed curve with white dashed lines. The yellow dashed arrow indicates the closest path for lithium ions to reach the nanowire. (c–h) Captured TEM

Chapter 4. In situ TEM investigation on lithiation mechanism of tunnel-structured α - MnO_2 nanowire

images from the real-time video, which are listed in chronological order. Each figure was captured every second, from 12 s after -1 V biasing. The red arrowhead indicates the progress of contrast, which should be strongly linked to lithium-ion movement. The yellow solid arrow indicates the observed Li-ion diffusion path in the nanowires. (i, j) TEM images of nanowires (i) before and (j) after the reaction. The width of each nanowire before and after the reaction is indicated in the figures.

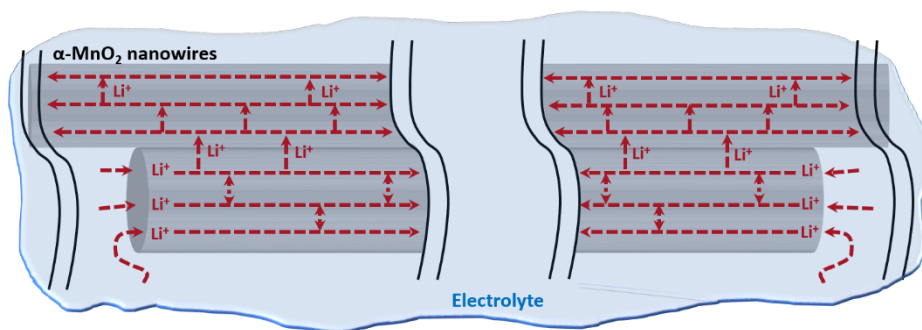


Figure 4.5. Schematic illustration of the lithium-ion diffusion in α - MnO_2 nanowires.

4.5. Structural evolution of α -MnO₂ nanowires during lithiation procedure

4.5.1. Overall phase evolution of a single nanowire

To identify the detailed lithiation mechanism of the α -MnO₂ nanowire electrode material, we further performed the *in situ* TEM experiment with the different setup. The conventional *in situ* TEM experimental method with the Li_xO tip in direct contact with the endpoint of a nanowire was applied for this investigation, for better control over the electrochemical reaction (Figure 4.2).[105, 106] Because we already verified that the longitudinal tunnels are the most favorable lithiation paths in cryptomelane-type nanowires, this setup would not differ significantly from the actual nanowire reaction in a real battery cell. A representative example of the *in situ* lithiation in the single α -MnO₂ nanowire with the conventional approach is shown in Figure 4.6. We applied negative voltage bias (−0.5 V) after the direct contact between the Li_xO tip and the nanowire to induce lithiation into the nanowire. The progress of the volume expansion front due to the continuous lithium-ion insertion and the forward movement of lithium ions is clearly observed in Figure 4.6b. The applied voltage bias was stopped in the middle of the reaction to distinguish the regions with and without lithium ions in a single nanowire, and to track the structural evolution of the nanowire depending on the lithium content. The Li_xO tip was detached from the nanowire after stopping the bias to avoid any additional unexpected reactions. Figure 4.6c–e show structure of the pristine nanowire for reference, which had the well-known α -MnO₂ structure with potassium dopant

placed along [111] zone axis.

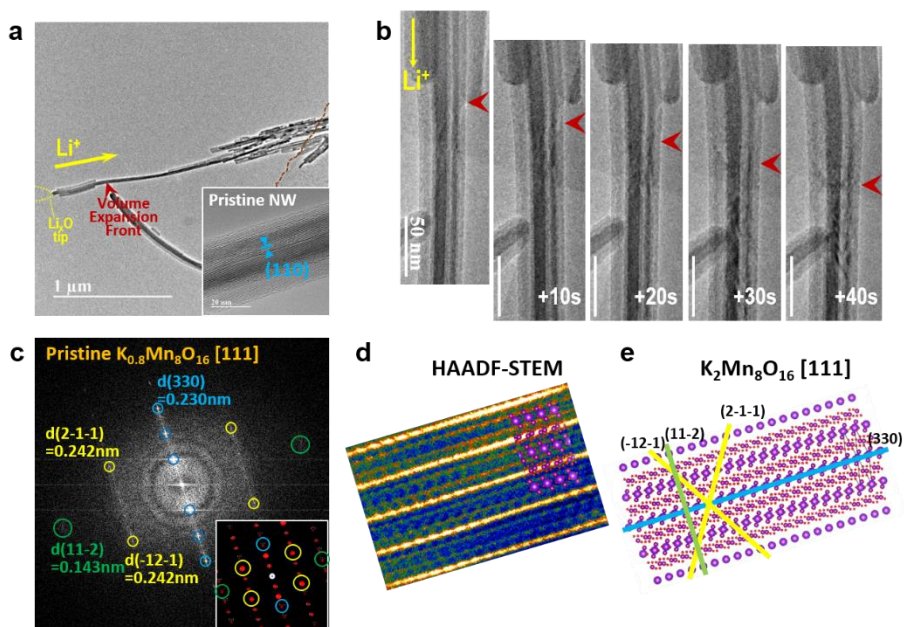


Figure 4.6. A representative example of the *in situ* lithiation in a single α - MnO_2 nanowire with the conventional end-point-contact method. (a) A low-magnification TEM image acquired after the *in-situ* lithiation. (b) Captured TEM images from the real-time video, listed in chronological order. (c) AFFT pattern of the HRTEM image obtained from the pristine nanowire shown in (a). (d) A HAADF-STEM image taken at [111] zone axis of a potassium-doped α - MnO_2 nanowire. (e) Atomic structural model of ideal $\text{K}_2\text{Mn}_8\text{O}_{16}$ material at [111] direction.

Electron energy loss spectra obtained during the *in situ* TEM observation shown in Figure 4.7 confirm the lithiation into the nanowire. The spectra were acquired at several areas of the nanowire after the *in situ* lithiation as marked with dashed circles in Figure 4.7a. Point 1 has the highest lithium content, and the lithium amount decreases as it is further away from the Li_xO tip. The gradual changes of the spectra is observable from

Chapter 4. In situ TEM investigation on lithiation mechanism of tunnel-structured α -MnO₂ nanowire

the Point 8 to 1 marked in the figure. In particular, the EELS shape change is remarkable from Point 3 to 1, which are the volume expanded regions due to the lithiation. The overlap between the Mn M- and Li K-edges hinders the clear recognition of lithium content in the nanowire, but the gradually intensified peaks near 60 and 64 eV can be classified into the Li K-edge. Moreover, the Li K- and O K-edges at Point 1 is close to the well-known EELS shape of Li₂O phase, which implies that the conversion reaction, forming Mn and Li₂O phases, already occurred at Point 1.[78] Thus, the analysis of the lithiated nanowire from Point 3 to 1 would enable the full description of the lithiation mechanism in the single α -MnO₂ nanowire from the insertion reaction to the conversion reaction ranges.

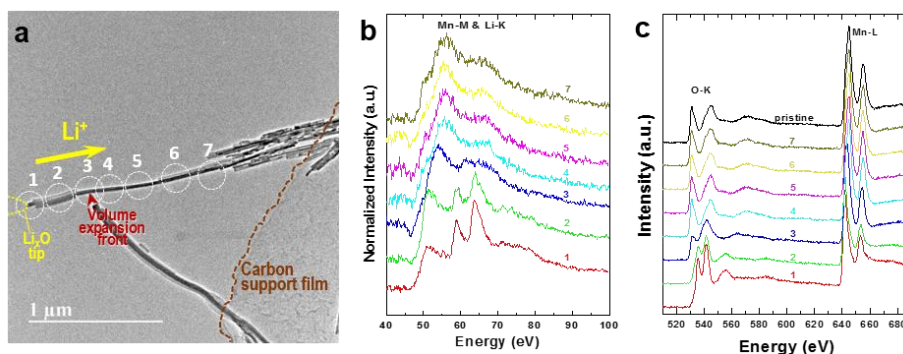


Figure 4.7. Experimental TEM-EELS spectra acquired during the *in situ* TEM measurement procedure. (a) A TEM image of the *in situ* lithiated nanowire reproduced from Figure 4.6a. (b, c) EELS spectra of (b) manganese M- and lithium K-, and (c) oxygen K- and manganese L-edges obtained after *in situ* lithiation. The numbers on each spectrum indicate the regions where the spectra were taken, which correspond to the numbers shown in (a).

During the *in situ* lithiation, the structure of the nanowire was gradually transformed as shown in Figure 4.8. The FFT patterns were obtained from several continuous HRTEM images of the *in situ* lithiated nanowire shown in Figure 4.6 and 4.7. Figure 4.8a shows that the region before the volume expanded maintains the pristine structure, tetragonal structure with lattice parameters of $a=b=0.967$ nm and $c=0.292$ nm, because there were almost no lithium ions inside. At the volume expansion front, the separation of (330) peaks were observed as shown in Figure 4.8b. It is attributed to the overlap of patterns right before and after the volume expansion front. In other words, the split diffraction peaks have originated from the FFT patterns from the overlaid regions with and almost without lithium ions. The FFT pattern of Figure 4.8a and c supports this description. The interplanar distances of (330) planes in Figure 4.8a and c that were obtained from the areas very close to the volume expansion front, match well with the peaks at the volume expansion front.

The estimated lattice parameters at the region shown in Figure 4.8c implies the cell expansion along the a- and b-axes at the early stages of the lithiation retaining the lattice along the c-axis. Because of the drastic structural changes in small ranges of the nanowire, it was impossible to calculate the precise lithium amount at this tiny point from the TEM-EELS data acquired from Point 3 marked in Figure 4.7a, which includes wider area. Nevertheless, the lithium amount at this point could be estimated based on the previous reports that performed DFT calculations.[89, 97, 98] Considering the calculated lattice parameters, volume, and the structural deformation in the previous reports, this state could be approximated as the range between $\text{Li}_4\text{Mn}_8\text{O}_{16}$ and $\text{Li}_6\text{Mn}_8\text{O}_{16}$.

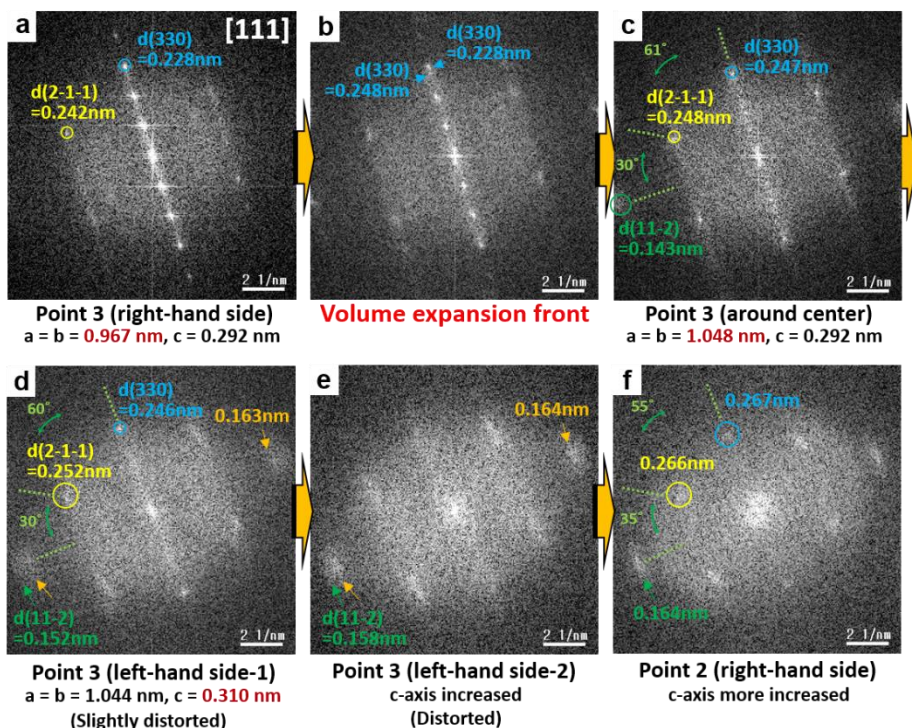


Figure 4.8. The changes of FFT patterns implying the gradual structural deformation depending on the lithiation level. The FFT patterns were obtained from several continuous HRTEM images of the *in situ* lithiated nanowire shown in Figure 4.6. The FFT pattern collected regions are written below the patterns with the corresponding numbers indicated in Figure 4.7a. The FFT patterns show the gradual structure transformation from (a) the state with almost no lithium ions to (f) the state with high lithium-content.

The nanowire began to be distorted with the higher lithiation level shown in Figure 4.8d. As shown in the figure, the interplanar spacing of (330) planes was not increased, but (11-2) planes showed the increased d-spacing, which implies the expansion along the c-axis. However, the FFT pattern cannot be fitted with a single zone axis of the tunnel structure with the tetragonal crystal system. It signifies the slight distortion of the original

tunnel structure. It seems that the early lithiation widens the (001) planes of the [2 \times 2] tunnels, followed by the length extension of the tunnels with the partial distortion and collapse of the tunnel structure. As the nanowire is further lithiated, it undergoes severe structural collapse as shown in Figure 4.8e and f.

4.5.2. MnO intermediate phase formation during conversion reaction

Interestingly, MnO phase was detected by the SAED pattern obtained near Point 3 indicated in Figure 4.7a (Figure 4.9). The detection of more peaks in the SAED pattern may be attributed to the higher sensitivity of the SAED patterns to phases than the FFT patterns from HRTEM images. The calculated lattice parameters from the SAED pattern are in the range of the lattice constants calculated from the FFT patterns obtained at this point (Figure 4.8c and d). The SAED pattern shown in Figure 4.9 contains three different phases: the expanded α - MnO_2 structure, the MnO phase with rocksalt structure, and the Li_2O phase. It could be hasty to determine the phases by a SAED pattern overlapped with several structures, but MnO phase was also observed in other SAED patterns obtained from other *in situ* lithiated nanowires as shown in Figure 4.10 and Figure 4.14.

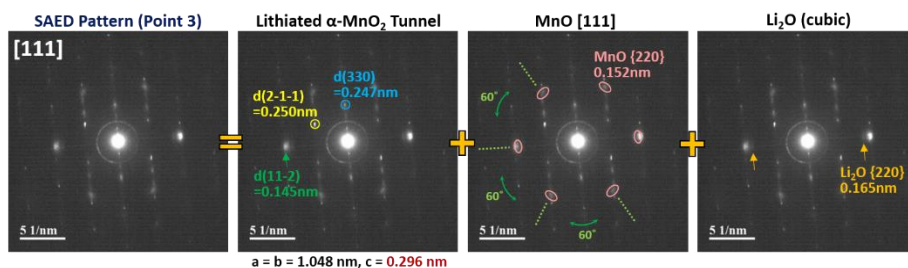


Figure 4.9. ASAED pattern obtained near Point 3 indicated in Figure 4.7a, which shows the formation of MnO

and Li_2O phase.

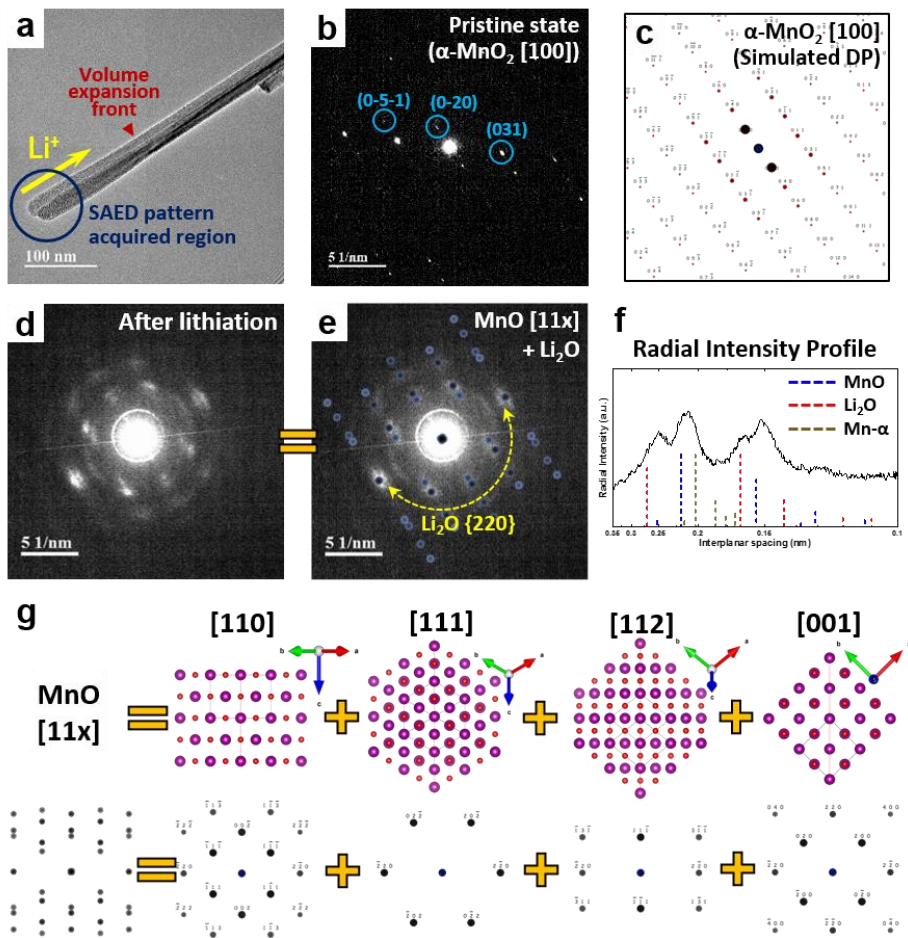


Figure 4.10. MnO phase appearance on an *in situ* lithiated nanowire. (a) A TEM image of the *in situ* lithiated nanowire. (b) The experimental and (c) the simulated SAED pattern obtained from the pristine nanowire shown in (a). (d) The experimental SAED pattern acquired after the *in situ* lithiation. (e) The SAED pattern corresponding to (d) overlaid with the simulated MnO phase at [11x] zone axes. (f) Radial intensity profile of the SAED pattern in (d). (g) Atomic structural models and the simulated electron diffraction patterns of MnO phase at [11x] zone axes.

Figure 4.10 shows one of examples in which MnO phase was observed. The potassium α - MnO_2 nanowire shown in Figure 4.10a was also *in situ* lithiated under the same procedure with the nanowire in Figure 4.6a. It was originally placed along the [100] zone axis as shown in Figure 4.10b. After the in-situ lithiation for a short time, the SAED pattern was completely changed as shown in Figure 4.10d. The radial intensities of the SAED pattern (Figure 4.10f) are close to the mixture of MnO and Li_2O phase. Interestingly, the MnO phase could be perfectly indexed with the sum of all [11x] zone axes, i.e. the sum of [110], [111], [112], [001], and so on. The electron diffraction pattern of MnO phase with the sum of [11x] zone axes is simulated and described in Figure 4.10g, which is overlaid onto the SAED pattern in Figure 4.10e. It is obviously different from the random orientation, and therefore, the formation of MnO phase would correlate with its parent α - MnO_2 structure.

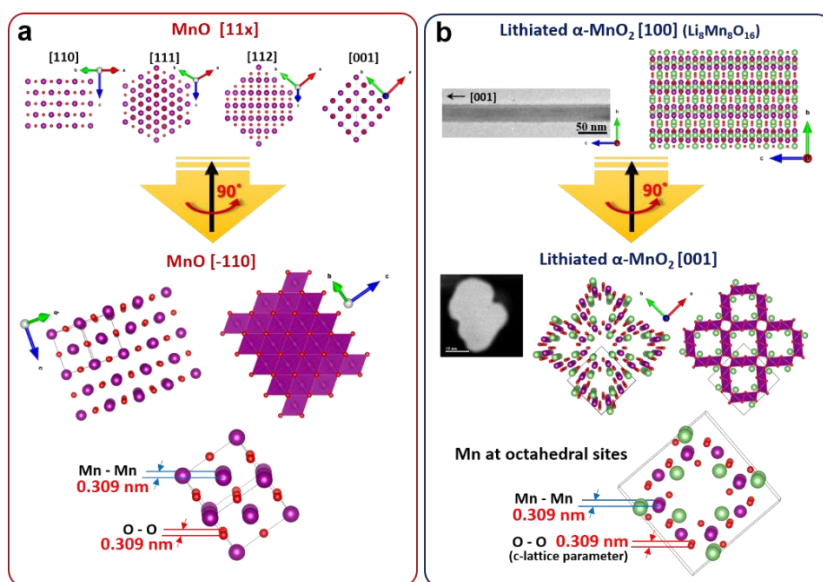


Figure 4.11. Schematic illustration of the crystal structural correlation between the appeared MnO phase and the lithiated α - MnO_2 phase of the nanowire.

The crystal structural correlation between the MnO phase and the lithiated α -MnO₂ structure of the nanowire is schematically described in Figure 4.11. Given that MnO phase with all [11x] zone axes was developed from the [100] zone axis of the α -MnO₂ structure, it could be inferred that MnO phase was arrayed along [-110] direction at the cross-sectional view of the nanowire, i.e. [001] zone axis of the α -MnO₂ nanowire, which is 90-degree rotated direction from the [100] α -MnO₂ nanowire (Figure 4.11). The in-plane rotational direction of [-110] MnO structure would be randomly oriented at the cross-sectional view of the nanowire. At the [-110] view of the rocksalt MnO phase, manganese and oxygen ions stand in a line along the [-110] direction, which is same with manganese and oxygen ions of the α -MnO₂ nanowire standing in a line through the tunnel direction. In addition, the Mn-Mn and O-O distances along the [-110] direction of MnO phase, 0.309 nm, is similar to the Mn-Mn and O-O distances along the [001] direction of the α -MnO₂ nanowire, i.e. the c-lattice parameter of the α -MnO₂ structure, calculated in Figure 4.8d where the tunnel structure began to be distorted and MnO phase observed (Figure 4.9). Thus, it seems that the MnO phase is formed during the partial collapse of the α -MnO₂ structure clustering in small groups, but almost sustaining the one-dimensional arrays of manganese and oxygen ions through the tunnel direction. The in-plane random orientation of MnO phase at [-110] direction should be attributed to the complex orientation relationship of manganese element in the original α -MnO₂ structure.

We further performed the TEM-EELS analysis with the nanowire shown in Figure 4.10a to identify the lithiation level that MnO phase begins to be formed at. Figure 4.12 shows the TEM-EELS spectra array obtained and collected from several nanowires

Chapter 4. In situ TEM investigation on lithiation mechanism of tunnel-structured α -MnO₂ nanowire

during the *in situ* TEM experiment, which are arranged in order of the lithiation levels. The lithiation levels were estimated based on the manganese L₃/L₂ intensity ratio and the spectra evolution trend. The lithium amount per unit structure, K_{0.8}Mn₈O₁₆, in Figure 4.12c was calculated on the basis of the experimental fingerprint shown in Figure 4.13. The EELS reference fingerprint data was acquired from the same K_{0.8}Mn₈O₁₆ nanowire samples, electrochemically lithiated in half-cell batteries. Because the nanowires lithiated up to 8 lithium in K_{0.8}Mn₈O₁₆ were used for collecting the EELS reference data, the lithium amount estimated much over than 8 Li in Mn₈O₁₆ was not written in Figure 4.12c. In addition, contrary to the consistent increasing tendency of the Mn L₃/L₂ intensity ratio with the Mn oxidation state reduction from MnO₂ to MnO phase, it shows the lower Mn L₃/L₂ intensity ratio in Mn metal than MnO phase.[107] It can explain why Spectrum 1 and 2 have lower Mn L₃/L₂ intensity ratio than Spectrum 3 in Figure 4.12c.

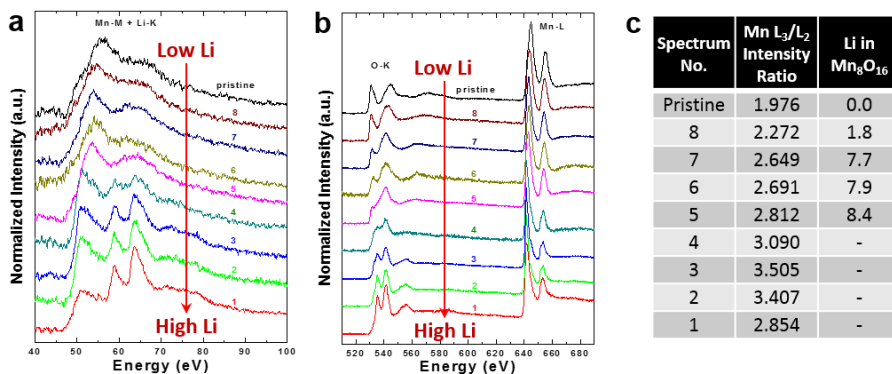


Figure 4.12. TEM-EELS spectra array collected from several *in situ* lithiated nanowires. (a) Mn M- and Li K-edges, and (b) O K- and Mn L-edges of the TEM-EELS spectra obtained during the *in situ* TEM experiment from the several α - MnO_2 nanowires, which are arranged in order of lithiation levels. The lithiation levels were estimated based on both of the manganese L₃/L₂ intensity ratio and the spectra evolution trend. (c) Estimated lithium amount per unit structure, $\text{K}_{0.8}\text{Mn}_8\text{O}_{16}$. The lithium amounts were calculated on the basis of the experimental fingerprint shown in Figure 4.13.

Spectrum 6 in Figure 4.12 was obtained from the marked area of the lithiated nanowire shown in Figure 4.10a, which is same as the SAED pattern obtained area where MnO phase was observed. It was estimated that 7.9 lithium ions are contained in the unit structure, $\text{K}_{0.8}\text{Mn}_8\text{O}_{16}$, at this area as shown in Figure 4.12c. Also, MnO phase observed region in the former nanowire, Point 3 in Figure 4.7, was estimated to contain 5.9 lithium ions in $\text{K}_{0.8}\text{Mn}_8\text{O}_{16}$. Even though TEM-EELS data was acquired from the broad area, it is still reasonable to approximate the lithium amount where MnO phase begins to be formed using the TEM-EELS data. It appears that MnO phase is formed from 6 Li in Mn_8O_{16} approximately, which is the lithiation level that the tunnel structure begins to be broken from.

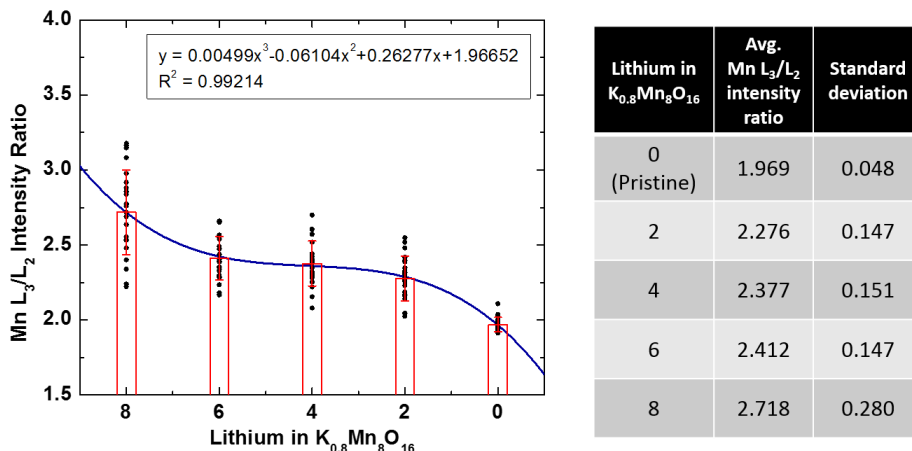


Figure 4.13. Manganese L_3/L_2 intensity ratio variation on lithiation levels in potassium α - MnO_2 nanowires calculated from TEM-EELS experimental data. Nanowire samples with Li^+ content of 0 (pristine), 2, 4, 6, and 8 in $\text{K}_{0.8}\text{Mn}_8\text{O}_{16}$ were prepared by electrochemical lithiation in half-cell batteries. The TEM-EELS data was taken with over 20 points in each sample, and each point contains several nanowires. The calculated Mn L_3/L_2 intensity ratios from each EELS spectrum are indicated with black dots on the graph. The average values of the Mn L_3/L_2 intensity ratios and the standard deviation are indicated with red column/bars. The polynomial fit curve is drawn with a solid line.

Another example of the MnO phase formation during the lithiation into the α - MnO_2 nanowire is shown in Figure 4.14, which obviously supports the description of MnO phase formation mechanism written above. The α - MnO_2 nanowire in Figure 4.14a was also lithiated by the *in situ* TEM experiment. As shown in Figure 4.14b and c, the pristine nanowire was oriented along [133] zone axis. After the *in situ* lithiation that was stopped in the middle of the reaction, additional bright diffraction peaks, which has interplanar spacing close to MnO {002} planes, appeared near the volume expansion front. In addition, the SAED pattern very similar to the pattern in Figure 4.10d was observed at

the further lithiated region, which is close to the Li_xO tip contact point.

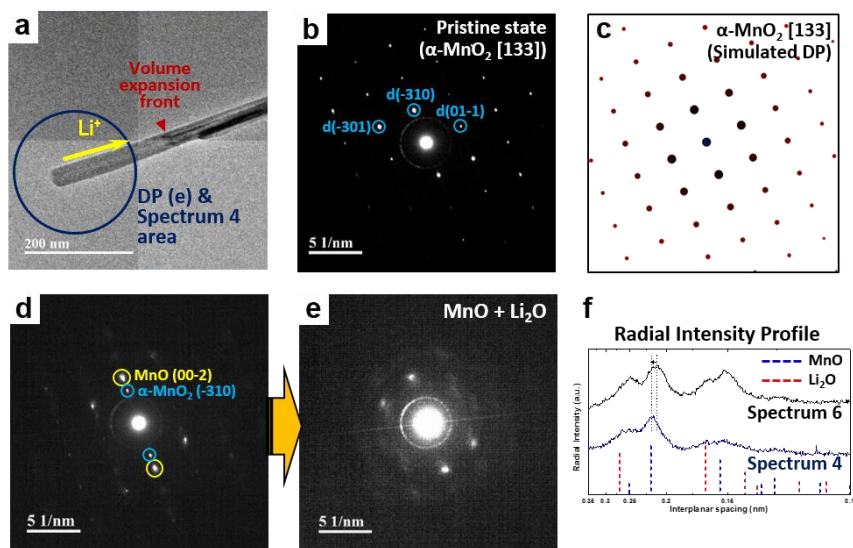


Figure 4.14. Another example of MnO phase formation during the lithiation into the α - MnO_2 nanowire. (a) A TEM image of the *in situ* lithiated nanowire. (b) The experimental and (c) the simulated SAED pattern obtained from the pristine nanowire shown in (a), which is aligned at [133] zone axis. (d, e) The SAED pattern acquired near the (d) volume expansion front and (e) the endpoint of the *in situ* lithiated nanowire. (f) Radial intensity profile of the SAED pattern shown in (e) (lower), comparing with the radial intensity profile of Figure 4.10f (upper). Each intensity profile is indicated with the corresponding EELS spectrum number of Figure 4.12. Spectrum 6 and 4 acquired regions correspond to the circled areas shown in Figure 4.10a and Figure 4.14a, respectively.

In particular, the radial intensity profile from the SAED pattern in Figure 4.14e matches even better with MnO and Li_2O phases than Figure 4.10f. Because the EELS spectra acquired in this area correspond to Spectrum 4 in Figure 4.12, it has the higher lithiation level than Figure 4.10d–f that corresponds to Spectrum 6 in Figure 4.12. Accordingly, it

Chapter 4. In situ TEM investigation on lithiation mechanism of tunnel-structured α -MnO₂ nanowire

seems that more stable MnO phase was formed releasing strain through further reduction reaction with more lithium ions. The O K-edge of the TEM-EELS spectrum strengthens this explanation. As shown in Spectrum 4 of Figure 4.12b, flat spectrum shape was observed in the O K-edge, which is the key feature of MnO phase.[108] It confirms that the MnO phase gradually reaches its ideal structure with higher lithiation levels, which result in the separation of MnO₂ into MnO and Li₂O phases.

Figure 4.15 shows how the SAED pattern from Figure 4.14e can be indexed. From Figure 4.10 and 4.11, we revealed that the MnO clusters oriented along any of the [11x] projecting directions are observed all together during the lithiation from the α -MnO₂ nanowire aligned at [100] zone axis. It implies that the α -MnO₂ nanowire aligned at [xy0] zone axes, perpendicular to c-axis, would show the same SAED pattern of MnO clusters. In addition, even though the projecting direction of the α -MnO₂ nanowire is slightly rotated from [xy0] to [xyz], it will show very similar SAED patterns of MnO clusters as shown in Figure 4.15a and b. In Figure 4.15a and b, the electron diffraction patterns of MnO clusters developed from α -MnO₂ [130] and [133] are compared. Because MnO clusters are randomly oriented under constraints of [11x] projecting directions in the [xy0] zone axis of the α -MnO₂ nanowire, most of the MnO diffraction planes observed in the SAED patterns at α -MnO₂ [xy0] also have to be observed at the slightly rotated α -MnO₂ [xyz] by particular MnO clusters oriented properly at this projecting direction. But, the angle relationship between the diffraction peaks can be different, and MnO (-220) planes, oriented perpendicular to the c-axis, cannot be detected at α -MnO₂ [xyz] ($z \neq 0$), as shown in Figure 4.15b. Nevertheless, note that the diffraction peaks at the position of (-220) planes can appear due to the double diffraction of (-11-1)/(-111) and (02-2)/(-202). As

shown in Figure 4.15c, the simulated diffraction pattern perfectly matches with the SAED pattern, Figure 4.14e, which obviously supports our description on the MnO phase development in the α -MnO₂ nanowire. The additional anticipated SAED patterns of MnO phase developed from several α -MnO₂ [xyz] axes are compared in Figure 4.16. In addition, from Figure 4.17 to 4.19 clearly describe the origins of the MnO diffraction peaks observed at α -MnO₂ [133] projection.

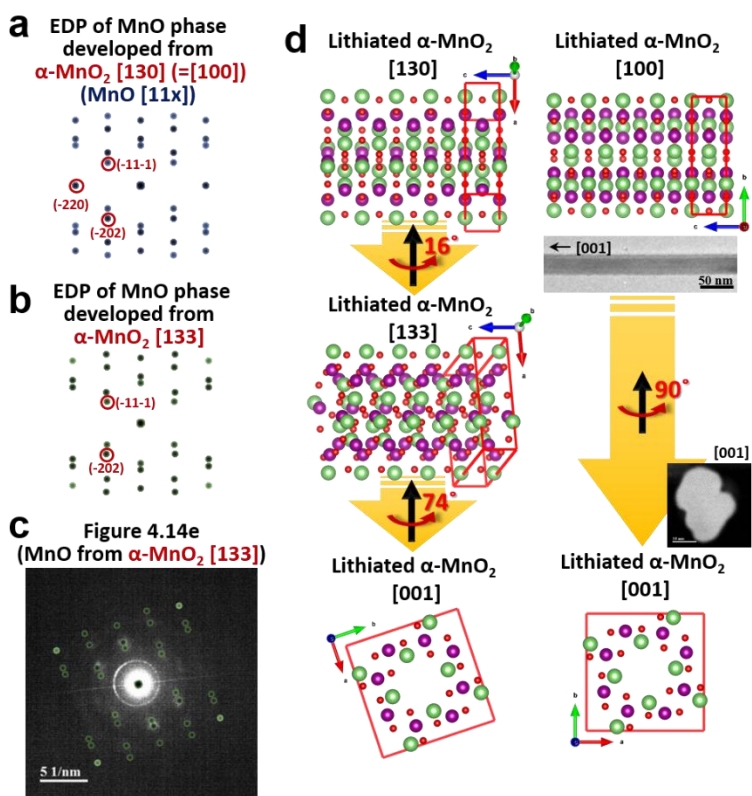


Figure 4.15. (a, b) The simulated electron diffraction patterns of MnO phase developed from the α -MnO₂ nanowire at (a) [130] and (b) [133] zone axes. (c) The SAED pattern shown in Figure 4.14e overlaid with the simulated EDP in (b). (d) Atomic structural models show the 3-D spatial orientation relationship between [100] and [133] directions of the α -MnO₂ nanowire.

EDP of MnO phase developed by lithiation at α - MnO_2 [100], [133], and [113]

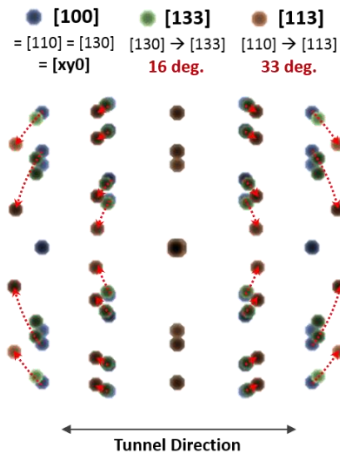


Figure 4.16. The simulated electron diffraction patterns of MnO phase developed during the lithiation from the α - MnO_2 nanowire oriented along [100], [133], [113] projecting directions.

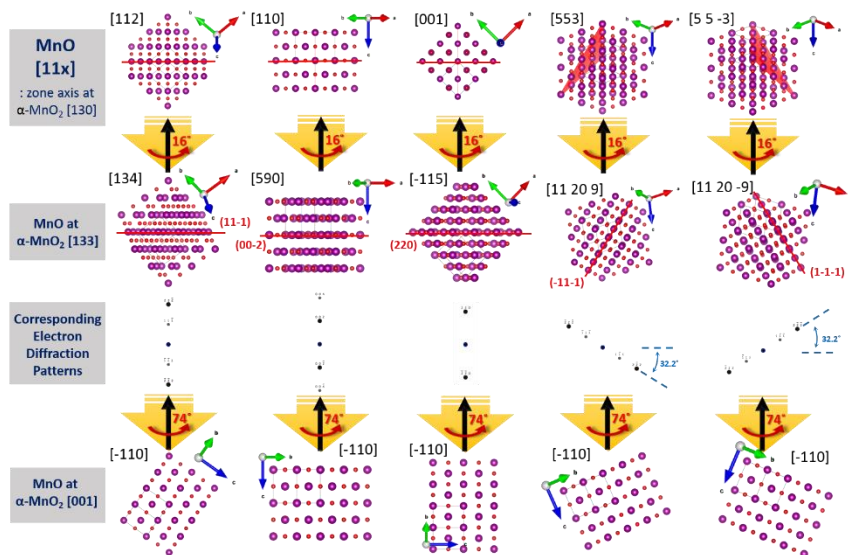


Figure 4.17. Three-dimensional spatial orientation relationship among atomic structural models of MnO phases showing the origins of the diffraction peaks from (11-1), (00-2), (220), (-11-1), and (1-1-1) planes observed at α - MnO_2 [133] projection.

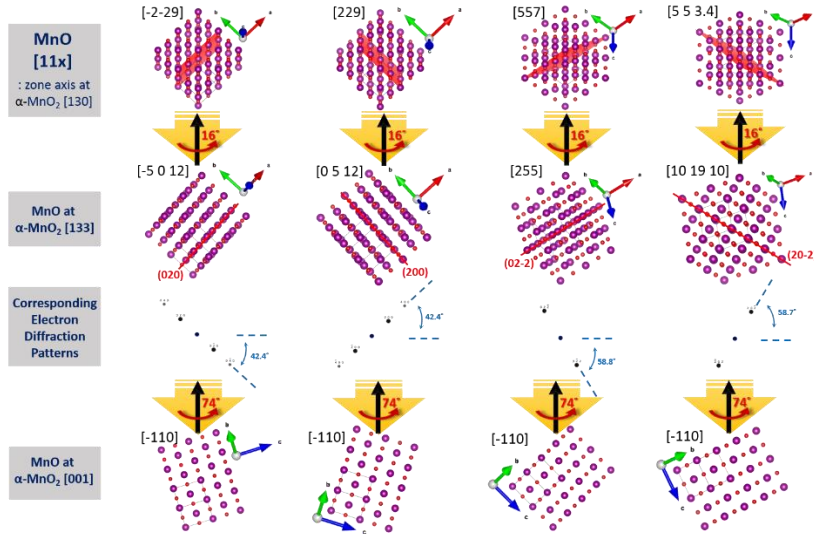


Figure 4.18. Three-dimensional spatial orientation relationship among atomic structural models of MnO phases showing the origins of the diffraction peaks from (020), (200), (02-2), and (20-2) planes observed at α - MnO_2 [133] projection.

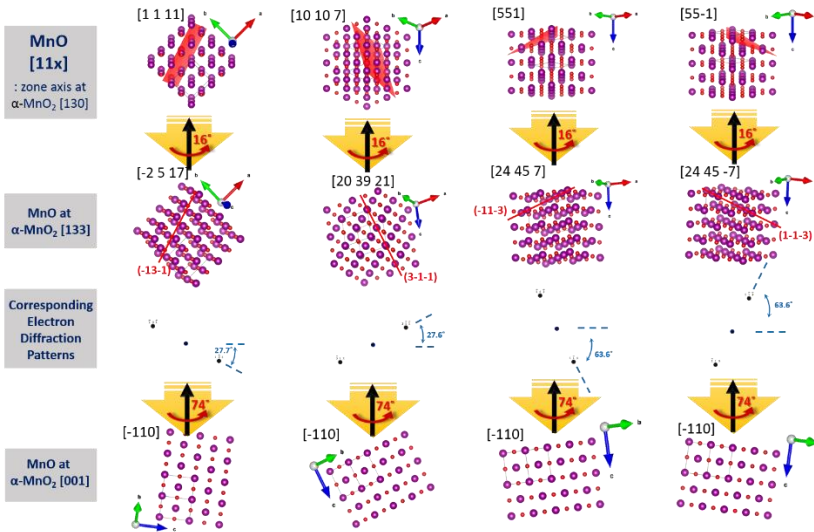


Figure 4.19. Three-dimensional spatial orientation relationship among atomic structural models of MnO phases showing the origins of the diffraction peaks from (-13-1), (3-1-1), (-11-3), and (1-1-3) planes observed at α - MnO_2 [133] projection.

4.5.3. Structural relationship between α -MnO₂ and Li₂O phases

Back to Figure 4.8 again, the d-spacings of the diffraction peaks from the FFT patterns in the much higher lithiation level (Figure 4.8f) match well with the cubic Li₂O phase. The SAED pattern acquired at Point 1 from the *in situ* lithiated nanowire shown in Figure 4.7a clearly shows the coincidence of the d-spacings in the SAED pattern with the Li₂O and Mn phase (Figure 4.20). Furthermore, Li K- and O K-edges of the TEM-EELS data obtained from the same region (Spectrum 1 in Figure 4.12 as well as Point 1 in Figure 4.7) show the well-known EELS shape of Li₂O phase, as already mentioned above.[78] The remarkable decrement of Mn L₃/L₂ intensity ratio at Spectrum 1 in Figure 4.12 also implies the transformation of MnO into Mn metal phase,[107] which indicates the full conversion reaction occurred from MnO₂ into Mn and Li₂O phase.

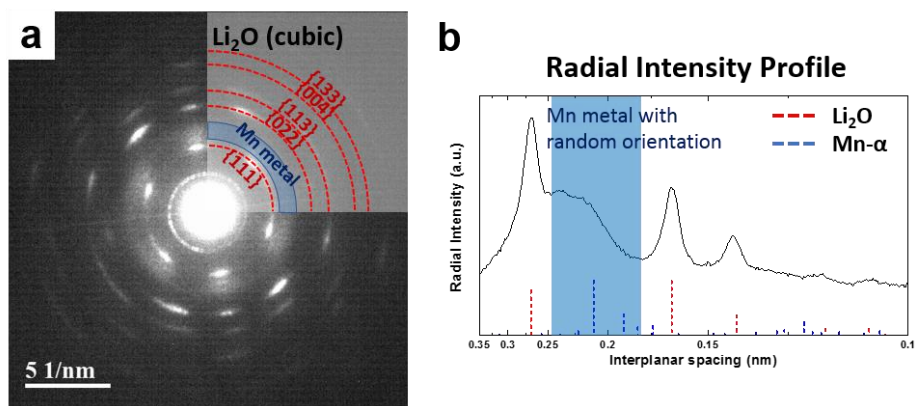


Figure 4.20. (a) A SAED pattern obtained at Point 1 from the *in situ* lithiated nanowire shown in Figure 4.7a, which was originally oriented along the α -MnO₂ [111]. (b) Radial intensity profile of the SAED pattern in (a). The d-spacings in the SAED patterns match well with the cubic Li₂O phase.

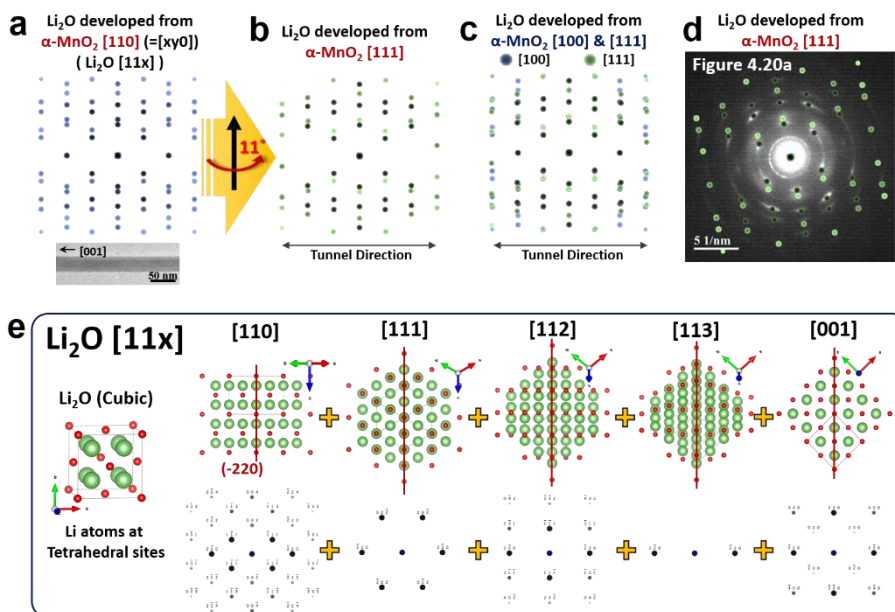


Figure 4.21. (a, b) The simulated electron diffraction patterns of Li_2O phase developed from the $\alpha\text{-MnO}_2$ nanowire at (a) [110] and (b) [111] projections. (c) The overlapped electron diffraction patterns shown in (a) and (b). (d) The SAED pattern shown in Figure 4.20a overlaid with the simulated EDP in (b). (e) Atomic structural models describe the origins of the diffraction peaks from Li_2O [11x] projection directions shown in (a).

Interestingly, the SAED pattern of Li_2O phase shown in Figure 4.20a also can be indexed by the same way as the MnO phase. We first assumed that Li_2O clusters would be randomly oriented along all of the possible [11x] projecting directions at $\alpha\text{-MnO}_2$ [110] projection. The presumed SAED pattern of Li_2O phase at $\alpha\text{-MnO}_2$ [110] projection is shown in Figure 4.21a. The origins of the diffraction peaks are displayed in Figure 4.21e. Even though we consider the $\alpha\text{-MnO}_2$ [111] projection, which is the original orientation of the *in situ* lithiated nanowire as shown in Figure 4.6c, the SAED pattern of Li_2O phase does not much change (Figure 4.21b). In particular, the diffraction peaks

Chapter 4. In situ TEM investigation on lithiation mechanism of tunnel-structured α - MnO_2 nanowire

close to the transmitted center beam are almost overlapped, as seen in Figure 4.21c. Figure 4.21d shows the SAED pattern in Figure 4.20a overlaid with the simulated diffraction pattern in Figure 4.21b; the anticipated SAED pattern matches well with the experimental SAED pattern. The missing (-220) peaks can be obtained by the double diffraction of (-11-1)/(-111) and (02-2)/(-202). The similar SAED pattern was also observed from the previous report, which showed *in situ* TEM lithiation into a single potassium α - MnO_2 nanowire oriented at [100] projection.[97] It supports the reasonability of our explanation.

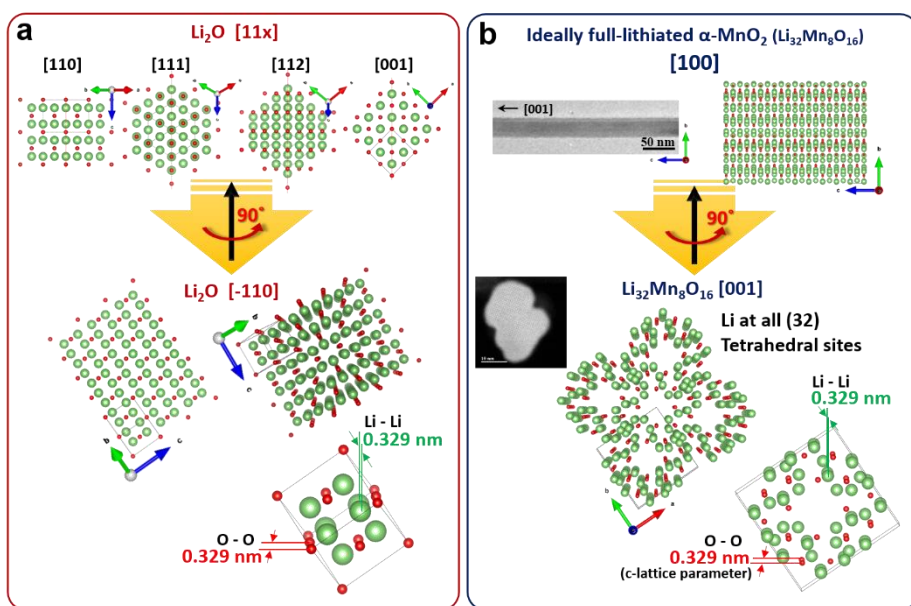


Figure 4.22. Schematic illustration of the crystal structural correlation between the appeared Li_2O phase and the ideally full-lithiated α - MnO_2 nanowire.

Figure 4.22 describes the probability and the meaning of this correlation between the Li₂O and the original α -MnO₂ structure. Similar to the evolution of MnO phase, Li₂O clusters at [-110] projecting directions with the random in-plane rotational orientation are developed from [001] projection of the α -MnO₂ nanowire. In this orientation, Li-Li and O-O distances along the [-110] direction of Li₂O phase are defined as 0.329 nm. The Li-Li and O-O distances along the corresponding direction of α -MnO₂ structure, [001], indicate the c-lattice parameter of the α -MnO₂ structure, which also should be 0.329 nm according to this crystallographic correlation. As shown in Figure 4.23a, ~10 % of the nanowire elongation was observed after the *in situ* lithiation, while the estimated c-lattice parameter increment is about 12.7 % (Figure 4.23b). Nevertheless, given that there was concentration gradient of lithium ions in the *in situ* lithiated nanowires and the position near the nanowire end point was only full-lithiated, the experimentally observed elongation matches quite well with our interpretation. On the basis of the structural correlation between Li₂O and α -MnO₂ structure shown in Figure 4.22, it is inferred that lithium and oxygen ions well maintain their one-dimensional arrays in the tunnels although there should be slight modulation for clustering Li₂O particles causing the break of the tunnel structure. The one-dimensional arrays of lithium ions may also support that the one-dimensional tunnels in α -MnO₂ structure are used for the facile lithium-ion diffusion paths. The 1-D lithium-ion arrays after the full lithiation would be helpful for the better coulombic efficiency and cycle performance in spite of the partial fracture of tunnels. Meanwhile, it appears that manganese atoms are extruded by lithium ions from their octahedral positions in the oxygen framework, which results in the formation of amorphous Mn metal as shown in the SAED pattern in Figure 4.20.

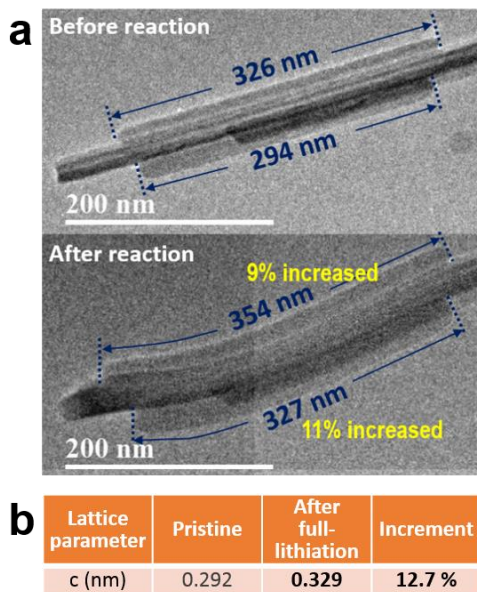


Figure 4.23. (a) Elongation of the nanowire after *in situ* lithiation in the TEM instrument. (b) Increment of c-lattice parameter estimated by the interpretation of the SAED pattern, which may correspond to the stretched length of the nanowire.

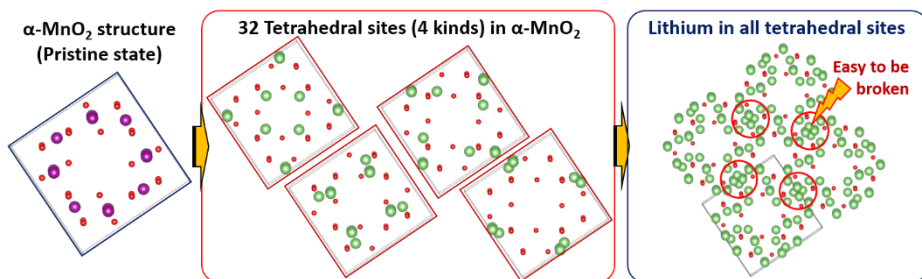
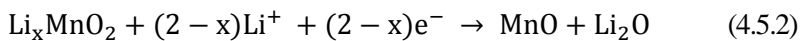


Figure 4.24. Schematic illustration of 32 tetrahedral sites in the α - MnO_2 tunnel structure, which may be the ideal positions for lithium ions after the full lithiation of the α - MnO_2 materials.

The structural correlation between the Li₂O and the α -MnO₂ structure also provides fundamental information on the position of lithium ions in the tunnels. There have been several reports that tried to estimate the position of lithium ions in the α -MnO₂ structure by DFT calculations. [89, 97, 98] Most of the reports suggested that the lithium ions are stable at 8h Wyckoff position in the α -MnO₂ structure, but one of the report insisted the movement of lithium ions from 8h to 8h' Wyckoff position at high lithiation levels due to the energetically stability.[89] Our interpretation on the Li₂O phase development (Figure 4.22) agrees with the occupancy of lithium ions at 8h' position after the full lithiation (32 lithium ions in the unit structure, Mn₈O₁₆) into the α -MnO₂ structure, which is tetrahedral sites with the nearby oxygen ions. All of the tetrahedral sites (32 sites) for lithium ions in the α -MnO₂ structure are drawn in Figure 4.24. As shown in the figure, too close tetrahedral sites for lithium ions in [1×1] tunnels might be the one of sources causing the fracture of the tunnel structure.

Based on the *in situ* TEM investigation, we corrected the generally known electrochemical reaction equations of α -MnO₂ material, as written below.



4.6. Summary

In this study, we revealed the lithiation mechanism of tunnel-structured α -MnO₂ nanowire by *in situ* TEM investigation. First, we directly observed that the [2×2] tunnels along the longitudinal direction are the easiest and fastest lithium-ion diffusion paths in potassium α -MnO₂ nanowires, rather than the lateral direction penetrating through the side wall of the nanowires. Also, we found out that the facile insertion reaction in the voltage range for cathode material (from MnO₂ to Li_{4.6}Mn₈O₁₆) only induces the tunnel expansion along a- and b- axis without the increment of c-lattice parameters.

Furthermore, we identified how conversion reaction occurs during the lithiation. We found out that MnO phase is formed as the intermediate phase during the conversion reaction. Besides, 3-D structural correlation between the developed MnO phase and the original α -MnO₂ tunnel structure was revealed. Partial fracture of the tunnel structure leads to the clustering of the cubic MnO rocksalt structure, which results in the MnO phase oriented along [-110] projecting direction at [001] tunnel direction of α -MnO₂ nanowire, without changing the original octahedral position of manganese ions in the oxygen framework. It turned out that Li₂O phase is also developed in the same way of the MnO development until the α -MnO₂ phase is transformed into Mn and Li₂O phase, finally. It was revealed that the developed Li₂O phase is also oriented along [-110] projecting direction at [001] projection of α -MnO₂ nanowire, with lithium and oxygen ions maintaining the 1-D arrays through the tunnels. Mn atoms seem to be extruded from the oxygen framework and lithium ions occupy 8h' tetrahedral sites in the tunnels. The 1-D arrays of lithium ions after the full lithiation may contribute to the better cycle

Chapter 4. In situ TEM investigation on lithiation mechanism of tunnel-structured α -MnO₂ nanowire

performance of the α -MnO₂ material. By the identification of the structural evolution of the α -MnO₂ lithium-ion battery electrode material, this work provides important information on the electrochemical reaction mechanism of tunnel-structured electrode materials, which extends the fundamental understanding on the field of the lithium-ion battery.[109]

Chapter 5

Conclusion

TEM studies can provide significant information related to the electrochemical reaction mechanisms of lithium-ion battery at nano-scale, but there have been a lot of limitations due to the requirements of special configuration and sampling techniques that are compatible to the lithium-ion battery system. For several years, we have focused on the better approaches to TEM investigation of lithium-ion battery electrode materials that can well describe and explain the electrochemical reactions in the lithium-ion battery. Accordingly, we improved TEM investigation techniques and applied properly for specific purpose of studies on lithium-ion battery electrode materials.

First, to reveal the origin of fast capacity fading shown in Ni-rich NCM cathode material, we directly compared the inside of secondary particles between NCM 1/1/1 and 8/1.5/0.5 materials by using FIB sampling technique. The observation on the cross-section of the same secondary particles before and after the electrochemical cycles clearly showed the severe surface degradation in Ni-rich NCM material, which should be the major source of fast capacity fading. The further investigation with atomic-resolution STEM images and EELS results, it was revealed that the instability of Ni³⁺ ions in Ni-rich NCM material may result in the severe surface degradation by causing

Chapter 5. Conclusion

the structural transformation and transition metal-ion dissolution into the electrolyte from the surface of primary particles. In addition, it was identified that the low-angle grain boundaries in a primary particle can also act as the surface of primary particles, which even lead to the development crack in the primary particle. Based on these findings, the optimization of the primary particle sizes and the surface treatment are suggested for better cycle performance of Ni-rich NCM cathode materials.

Furthermore, we improved the *ex situ* TEM experimental method to track the phase evolution of SnO₂ anode material and reveal the possibility of reverse conversion reaction and the origin of the additional capacity, which has been controversial. SnO₂ particles dispersed on a carbon film-coated copper TEM grid were placed with the conventional SnO₂ slurry electrode in a coin battery cell and electrochemically (dis)charged toward specific voltages to investigate the phase evolution of the same particles during the first full cycle by TEM. By this method, we revealed that the origin of the extra capacity is related to the reaction of the Li₂O phase. The majority of additional capacity on the charge is derived from the lithium-ion extractions from the Li₂O, which possibly accompanies the formation of lithium-deficient amorphous lithium oxide. In addition, few reversed SnO particles were observed during the charge, which implies the probability of the reverse conversion reaction. However, it does not seem to greatly contribute to the additional capacity on the charge process. Notably, SnO₂ phase did not reappear at all. This research provides fundamental knowledge on the electrochemical reaction mechanism of SnO₂ anode material by the developed *ex situ* TEM experimental technique.

Finally, we applied the *in situ* TEM experimental technique to identify the actual

Chapter 5. Conclusion

lithium-ion diffusion paths and the lithiation mechanism of tunnel-structured MnO₂ nanowire. By setting up the special configuration using a carbon film-deposited copper TEM grid, it was possible to distinguish the lithium-ion diffusion through the tunnel direction and the side wall of the nanowire, which is considered to be impossible by *ex situ* studies. It was observed that the lithium ions are diffused rapidly through the tunnel direction in the nanowire although lithium ions first encountered the side wall of the nanowire, which verifies the facile diffusion through the unique tunnels in the α -MnO₂ nanowire. In addition, we revealed the precise lithiation mechanism of α -MnO₂ material up to the full-lithiation procedure. It was exposed that MnO intermediate phase appears during the conversion reaction of α -MnO₂ material, which was identified by electron diffraction, HRTEM, and TEM-EELS results acquired during the *in situ* TEM experiment. In addition, the 3-D structural correlation between the original α -MnO₂ structure and the appeared MnO phase was identified. It was inferred that the MnO phase is developed at the original position of Mn ions in the octahedral site of the oxygen framework with the partial collapse of the tunnel structure. Moreover, it was found out that Li₂O phase is also developed in the same way as MnO phase. It was verified that lithium and oxygen ions well maintain the 1-D array along the tunnels even after the full lithiation. It would be helpful for the reversible conversion reaction that is directly related to the cycle performance of MnO₂ electrode material as the lithium-ion battery anode.

As explained above, we improved the TEM experimental techniques for the investigation of lithium-ion battery electrode materials. These works suggest the robust TEM experimental methods which are widely applicable to the battery analysis. Furthermore, the studies provide the further profound information on the

Chapter 5. Conclusion

electrochemical reaction mechanisms of various promising lithium-ion battery electrode materials.

References

- [1] T. Sasaki, V. Godbole, Y. Takeuchi, Y. Ukyo, and P. Novak, "Morphological and Structural Changes of Mg-Substituted Li(Ni,Co,Al)O₂ during Overcharge Reaction," *Journal of the Electrochemical Society*, vol. 158, no. 11, pp. A1214-A1219, 2011.
- [2] F. Wang, S. W. Kim, D. H. Seo, K. Kang, L. P. Wang, D. Su, J. J. Vajo, J. Wang, and J. Graetz, "Ternary metal fluorides as high-energy cathodes with low cycling hysteresis," *Nature Communications*, vol. 6, 2015.
- [3] Y. Y. Hu, Z. G. Liu, K. W. Nam, O. J. Borkiewicz, J. Cheng, X. Hua, M. T. Dunstan, X. Q. Yu, K. M. Wiaderek, L. S. Du, K. W. Chapman, P. J. Chupas, X. Q. Yang, and C. P. Grey, "Origin of additional capacities in metal oxide lithium-ion battery electrodes," *Nature Materials*, vol. 12, no. 12, pp. 1130-1136, 2013.
- [4] J. M. Zheng, P. H. Xu, M. Gu, J. Xiao, N. D. Browning, P. F. Yan, C. M. Wang, and J. G. Zhang, "Structural and Chemical Evolution of Li- and Mn-Rich Layered Cathode Material," *Chemistry of Materials*, vol. 27, no. 4, pp. 1381-1390, 2015.
- [5] M. Sina, K. W. Nam, D. Su, N. Pereira, X. Q. Yang, G. G. Amatucci, and F. Cosandey, "Structural phase transformation and Fe valence evolution in FeO_xF_{2-x}/C nanocomposite electrodes during lithiation and de-lithiation processes," *Journal of Materials Chemistry A*, vol. 1, no. 38, pp. 11629-11640, 2013.
- [6] X. H. Liu, H. Zheng, L. Zhong, S. Huan, K. Karki, L. Q. Zhang, Y. Liu, A. Kushima, W. T. Liang, J. W. Wang, J. H. Cho, E. Epstein, S. A. Dayeh, S. T. Picraux, T. Zhu, J. Li, J. P. Sullivan, J. Cumings, C. S. Wang, S. X. Mao, Z. Z. Ye, S. L. Zhang, and J. Y. Huang, "Anisotropic Swelling and Fracture of Silicon Nanowires during Lithiation," *Nano Letters*, vol. 11, no. 8, pp. 3312-3318, 2011.
- [7] Y. Idota, T. Kubota, A. Matsufuji, Y. Maekawa, and T. Miyasaka, "Tin-based amorphous oxide: A high-capacity lithium-ion-storage material," *Science*, vol. 276, no. 5317, pp. 1395-1397, 1997.
- [8] B. Xu, C. R. Fell, M. F. Chi, and Y. S. Meng, "Identifying surface structural changes in layered Li-excess nickel manganese oxides in high voltage lithium

- ion batteries: A joint experimental and theoretical study,” *Energy & Environmental Science*, vol. 4, no. 6, pp. 2223-2233, 2011.
- [9] L. Gu, C. B. Zhu, H. Li, Y. Yu, C. L. Li, S. Tsukimoto, J. Maier, and Y. Ikuhara, “Direct Observation of Lithium Staging in Partially Delithiated LiFePO₄ at Atomic Resolution,” *Journal of the American Chemical Society*, vol. 133, no. 13, pp. 4661-4663, 2011.
- [10] M. von Ardenne, “The Scanning Electron Microscope,” *Zeitschrift Fur Physik*, vol. 109, no. 9-10, pp. 553-572, 1938.
- [11] A. V. Crewe, J. Wall, and J. Langmore, “Visibility of Single Atoms,” *Science*, vol. 168, no. 3937, pp. 1338-1340, 1970.
- [12] S. J. Pennycook, “Z-Contrast Transmission Electron-Microscopy - Direct Atomic Imaging of Materials,” *Annual Review of Materials Science*, vol. 22, pp. 171-195, 1992.
- [13] R. Ishikawa, E. Okunishi, H. Sawada, Y. Kondo, F. Hosokawa, and E. Abe, “Direct imaging of hydrogen-atom columns in a crystal by annular bright-field electron microscopy,” *Nature Materials*, vol. 10, no. 4, pp. 278-281, Apr, 2011.
- [14] R. F. Egerton, “Electron energy-loss spectroscopy in the TEM,” *Reports on Progress in Physics*, vol. 72, no. 1, 2009.
- [15] D. H. Pearson, C. C. Ahn, and B. Fultz, “White Lines and D-Electron Occupancies for the 3d and 4d Transition-Metals,” *Physical Review B*, vol. 47, no. 14, pp. 8471-8478, 1993.
- [16] J. Y. Huang, L. Zhong, C. M. Wang, J. P. Sullivan, W. Xu, L. Q. Zhang, S. X. Mao, N. S. Hudak, X. H. Liu, A. Subramanian, H. Y. Fan, L. A. Qi, A. Kushima, and J. Li, “In Situ Observation of the Electrochemical Lithiation of a Single SnO₂ Nanowire Electrode,” *Science*, vol. 330, no. 6010, pp. 1515-1520, 2010.
- [17] X. H. Liu, and J. Y. Huang, “In situ TEM electrochemistry of anode materials in lithium ion batteries,” *Energy & Environmental Science*, vol. 4, no. 10, pp. 3844-3860, 2011.
- [18] J. R. Croy, A. Abouimrane, and Z. C. Zhang, “Next-generation lithium-ion batteries: The promise of near-term advancements,” *Mrs Bulletin*, vol. 39, no. 5, pp. 407-415, 2014.
- [19] S. Liu, L. Xiong, and C. He, “Long cycle life lithium ion battery with lithium nickel cobalt manganese oxide (NCM) cathode,” *Journal of Power Sources*, vol. 261, pp. 285-291, 2014.
- [20] H. S. Liu, M. Bugnet, M. Z. Tessaro, K. J. Harris, M. J. R. Dunham, M. Jiang,

- G. R. Goward, and G. A. Botton, "Spatially resolved surface valence gradient and structural transformation of lithium transition metal oxides in lithium-ion batteries," *Physical Chemistry Chemical Physics*, vol. 18, no. 42, pp. 29064-29075, 2016.
- [21] K. Zhang, X. P. Han, Z. Hu, X. L. Zhang, Z. L. Tao, and J. Chen, "Nanostructured Mn-based oxides for electrochemical energy storage and conversion," *Chemical Society Reviews*, vol. 44, no. 3, pp. 699-728, 2015.
- [22] F. Lin, I. M. Markus, D. Nordlund, T. C. Weng, M. D. Asta, H. L. L. Xin, and M. M. Doeff, "Surface reconstruction and chemical evolution of stoichiometric layered cathode materials for lithium-ion batteries," *Nature Communications*, vol. 5, 2014.
- [23] S. K. Jung, H. Gwon, J. Hong, K. Y. Park, D. H. Seo, H. Kim, J. Hyun, W. Yang, and K. Kang, "Understanding the Degradation Mechanisms of LiNi_{0.5}Co_{0.2}Mn_{0.3}O₂ Cathode Material in Lithium Ion Batteries," *Advanced Energy Materials*, vol. 4, no. 1, 2014.
- [24] R. Hausbrand, G. Cherkashinin, H. Ehrenberg, M. Groting, K. Albe, C. Hess, and W. Jaegermann, "Fundamental degradation mechanisms of layered oxide Li-ion battery cathode materials: Methodology, insights and novel approaches," *Materials Science and Engineering B-Advanced Functional Solid-State Materials*, vol. 192, pp. 3-25, 2015.
- [25] C. P. Liang, F. T. Kong, R. C. Longo, S. Kc, J. S. Kim, S. Jeon, S. Choi, and K. Cho, "Unraveling the Origin of Instability in Ni-Rich LiNi_{1-2x}CoxMnxO₂ (NCM) Cathode Materials," *Journal of Physical Chemistry C*, vol. 120, no. 12, pp. 6383-6393, 2016.
- [26] E. F. Rauch, and M. Veron, "Coupled microstructural observations and local texture measurements with an automated crystallographic orientation mapping tool attached to a tem," *Materialwissenschaft Und Werkstofftechnik*, vol. 36, no. 10, pp. 552-556, 2005.
- [27] D. Mohanty, J. L. Li, D. P. Abraham, A. Huq, E. A. Payzant, D. L. Wood, and C. Daniel, "Unraveling the Voltage-Fade Mechanism in High-Energy-Density Lithium-Ion Batteries: Origin of the Tetrahedral Cations for Spinel Conversion," *Chemistry of Materials*, vol. 26, no. 21, pp. 6272-6280, 2014.
- [28] K. W. Nam, S. M. Bak, E. Y. Hu, X. Q. Yu, Y. N. Zhou, X. J. Wang, L. J. Wu, Y. M. Zhu, K. Y. Chung, and X. Q. Yang, "Combining In Situ Synchrotron X-Ray Diffraction and Absorption Techniques with Transmission Electron

- Microscopy to Study the Origin of Thermal Instability in Overcharged Cathode Materials for Lithium-Ion Batteries,” *Advanced Functional Materials*, vol. 23, no. 8, pp. 1047-1063, 2013.
- [29] J. Li, L. Downie, L. Ma, W. Qiu, and J. Dahn, “Study of the Failure Mechanisms of $\text{LiNi}_{0.8}\text{Mn}_{0.1}\text{Co}_{0.1}\text{O}_2$ Cathode Material for Lithium Ion Batteries,” *Journal of the Electrochemical Society*, vol. 162, no. 7, pp. A1401-A1408, 2015.
- [30] K. Min, K. Kim, C. Jung, S. Seo, Y. Song, H. Lee, J. Shin, and E. Cho, “A comparative study of structural changes in lithium nickel cobalt manganese oxide as a function of Ni content during delithiation process,” *Journal of Power Sources*, vol. 315, pp. 111-119, 2016.
- [31] M. Sathiya, K. Hemalatha, K. Ramesha, J. M. Tarascon, and A. S. Prakash, “Synthesis, Structure, and Electrochemical Properties of the Layered Sodium Insertion Cathode Material: $\text{NaNi}_{1/3}\text{Mn}_{1/3}\text{Co}_{1/3}\text{O}_2$,” *Chemistry of Materials*, vol. 24, no. 10, pp. 1846-1853, 2012.
- [32] S. Lee, M. Kim, Y. Zhu, and G. Park, “Investigation on structural deterioration of Ni-rich NCM cathode material,” in preparation.
- [33] T. Brousse, R. Retoux, U. Herterich, and D. M. Schleich, “Thin-film crystalline SnO_2 -lithium electrodes,” *Journal of the Electrochemical Society*, vol. 145, no. 1, pp. 1-4, 1998.
- [34] H. P. Liu, D. H. Long, X. J. Liu, W. M. Qiao, L. Zhan, and L. C. Ling, “Facile synthesis and superior anodic performance of ultrafine SnO_2 -containing nanocomposites,” *Electrochimica Acta*, vol. 54, no. 24, pp. 5782-5788, 2009.
- [35] S. Nam, S. Kim, S. Wi, H. Choi, S. Byun, S. M. Choi, S. I. Yoo, K. T. Lee, and B. Park, “The role of carbon incorporation in SnO_2 nanoparticles for Li rechargeable batteries,” *Journal of Power Sources*, vol. 211, pp. 154-160, 2012.
- [36] Y. Yu, L. Gu, A. Dhanabalan, C. H. Chen, and C. L. Wang, “Three-dimensional porous amorphous SnO_2 thin films as anodes for Li-ion batteries,” *Electrochimica Acta*, vol. 54, no. 28, pp. 7227-7230, 2009.
- [37] M. D. Slater, D. Kim, E. Lee, and C. S. Johnson, “Sodium-Ion Batteries,” *Advanced Functional Materials*, vol. 23, no. 8, pp. 947-958, 2013.
- [38] D. W. Su, H. J. Ahn, and G. X. Wang, “ SnO_2 @graphene nanocomposites as anode materials for Na-ion batteries with superior electrochemical performance,” *Chemical Communications*, vol. 49, no. 30, pp. 3131-3133, 2013.

- [39] I. A. Courtney, and J. R. Dahn, "Electrochemical and in situ x-ray diffraction studies of the reaction of lithium with tin oxide composites," *Journal of the Electrochemical Society*, vol. 144, no. 6, pp. 2045-2052, 1997.
- [40] J. Q. Wang, I. D. Raistrick, and R. A. Huggins, "Behavior of Some Binary Lithium Alloys as Negative Electrodes in Organic Solvent-Based Electrolytes," *Journal of the Electrochemical Society*, vol. 133, no. 3, pp. 457-460, 1986.
- [41] W. F. Liu, X. J. Huang, Z. X. Wang, H. Li, and L. Q. Chen, "Studies of stannic oxide as an anode material for lithium-ion batteries," *Journal of the Electrochemical Society*, vol. 145, no. 1, pp. 59-62, 1998.
- [42] C. M. Wang, W. Xu, J. Liu, J. G. Zhang, L. V. Saraf, B. W. Arey, D. W. Choi, Z. G. Yang, J. Xiao, S. Thevuthasan, and D. R. Baer, "In Situ Transmission Electron Microscopy Observation of Microstructure and Phase Evolution in a SnO₂ Nanowire during Lithium Intercalation," *Nano Letters*, vol. 11, no. 5, pp. 1874-1880, 2011.
- [43] Y. Yu, C. H. Chen, and Y. Shi, "A tin-based amorphous oxide composite with a porous, spherical, multideck-cage morphology as a highly reversible anode material for lithium-ion batteries," *Advanced Materials*, vol. 19, no. 7, pp. 993-997, 2007.
- [44] P. Balaya, H. Li, L. Kienle, and J. Maier, "Fully reversible homogeneous and heterogeneous Li storage in RuO₂ with high capacity," *Advanced Functional Materials*, vol. 13, no. 8, pp. 621-625, 2003.
- [45] J. Cabana, L. Monconduit, D. Larcher, and M. R. Palacin, "Beyond Intercalation-Based Li-Ion Batteries: The State of the Art and Challenges of Electrode Materials Reacting Through Conversion Reactions," *Advanced Materials*, vol. 22, no. 35, pp. E170-E192, 2010.
- [46] J. Z. Wang, N. Du, H. Zhang, J. X. Yu, and D. R. Yang, "Large-Scale Synthesis of SnO₂ Nanotube Arrays as High-Performance Anode Materials of Li-Ion Batteries," *Journal of Physical Chemistry C*, vol. 115, no. 22, pp. 11302-11305, 2011.
- [47] D. Deng, and J. Y. Lee, "Hollow core-shell mesospheres of crystalline SnO₂ nanoparticle aggregates for high capacity Li⁺ ion storage," *Chemistry of Materials*, vol. 20, no. 5, pp. 1841-1846, 2008.
- [48] R. Q. Liu, N. Li, D. Y. Li, G. F. Xia, Y. M. Zhu, S. Y. Yu, and C. Wang, "Template-free synthesis of SnO₂ hollow microspheres as anode material for lithium-ion battery," *Materials Letters*, vol. 73, pp. 1-3, 2012.

- [49] A. J. Gmitter, F. Badway, S. Rangan, R. A. Bartynski, A. Halajko, N. Pereira, and G. G. Amatucci, "Formation, dynamics, and implication of solid electrolyte interphase in high voltage reversible conversion fluoride nanocomposites," *Journal of Materials Chemistry*, vol. 20, no. 20, pp. 4149-4161, 2010.
- [50] E. Bekaert, P. Balaya, S. Murugavel, J. Maier, and M. Menetrier, "Li6 MAS NMR Investigation of Electrochemical Lithiation of RuO2: Evidence for an Interfacial Storage Mechanism," *Chemistry of Materials*, vol. 21, no. 5, pp. 856-861, 2009.
- [51] S. Laruelle, S. Pilard, P. Guenot, S. Grugeon, and J. M. Tarascon, "Identification of Li-based electrolyte degradation products through DEI and ESI high-resolution mass spectrometry," *Journal of the Electrochemical Society*, vol. 151, no. 8, pp. A1202-A1209, 2004.
- [52] Y. F. Zhukovskii, E. A. Kotomin, P. Balaya, and J. Maier, "Enhanced interfacial lithium storage in nanocomposites of transition metals with LiF and Li2O: Comparison of DFT calculations and experimental studies," *Solid State Sciences*, vol. 10, no. 4, pp. 491-495, 2008.
- [53] J. Jamnik, and J. Maier, "Nanocrystallinity effects in lithium battery materials - Aspects of nano-ionics. Part IV," *Physical Chemistry Chemical Physics*, vol. 5, no. 23, pp. 5215-5220, 2003.
- [54] A. Ponrouch, P. L. Taberna, P. Simon, and M. R. Palacin, "On the origin of the extra capacity at low potential in materials for Li batteries reacting through conversion reaction," *Electrochimica Acta*, vol. 61, pp. 13-18, 2012.
- [55] D. Larcher, D. Bonnin, R. Cortes, I. Rivals, L. Personnaz, and J. M. Tarascon, "Combined XRD, EXAFS, and Mossbauer studies of the reduction by lithium of alpha-Fe2O3 with various particle sizes," *Journal of the Electrochemical Society*, vol. 150, no. 12, pp. A1643-A1650, 2003.
- [56] J. Maier, "Mass storage in space charge regions of nano-sized systems (Nano-ionics. Part V)," *Faraday Discussions*, vol. 134, pp. 51-66, 2007.
- [57] S. Laruelle, S. Grugeon, P. Poizot, M. Dolle, L. Dupont, and J. M. Tarascon, "On the origin of the extra electrochemical capacity displayed by MO/Li cells at low potential," *Journal of the Electrochemical Society*, vol. 149, no. 5, pp. A627-A634, 2002.
- [58] R. Demir-Cakan, Y. S. Hu, M. Antonietti, J. Maier, and M. M. Titirici, "Facile one-pot synthesis of mesoporous SnO2 microspheres via nanoparticles

- assembly and lithium storage properties,” *Chemistry of Materials*, vol. 20, no. 4, pp. 1227-1229, 2008.
- [59] J. Yao, X. P. Shen, B. Wang, H. K. Liu, and G. X. Wang, “In situ chemical synthesis of SnO₂-graphene nanocomposite as anode materials for lithium-ion batteries,” *Electrochemistry Communications*, vol. 11, no. 10, pp. 1849-1852, 2009.
- [60] G. Kilibarda, D. V. Szabo, S. Schlabach, V. Winkler, M. Bruns, and T. Hanemann, “Investigation of the degradation of SnO₂ electrodes for use in Li-ion cells,” *Journal of Power Sources*, vol. 233, pp. 139-147, 2013.
- [61] S. T. Chang, I. C. Leu, C. L. Liao, J. H. Yen, and M. H. Hon, “Electrochemical behavior of nanocrystalline tin oxide electrodeposited on a Cu substrate for Li-ion batteries,” *Journal of Materials Chemistry*, vol. 14, no. 12, pp. 1821-1826, 2004.
- [62] J. Chouvin, C. Branci, J. Sarradin, J. Olivier-Fourcade, J. C. Jumas, B. Simon, and P. Biensan, “Lithium intercalation in tin oxide,” *Journal of Power Sources*, vol. 81, pp. 277-281, 1999.
- [63] I. A. Courtney, R. A. Dunlap, and J. R. Dahn, “In-situ Sn-119 Mossbauer effect studies of the reaction of lithium with SnO and SnO : 0.25 B₂O₃ : 0.25 P₂O₅ glass,” *Electrochimica Acta*, vol. 45, no. 1-2, pp. 51-58, 1999.
- [64] I. Sandu, T. Brousse, D. M. Schleich, and M. Danot, “The chemical changes occurring upon cycling of a SnO₂ negative electrode for lithium ion cell: In situ Mossbauer investigation,” *Journal of Solid State Chemistry*, vol. 179, no. 2, pp. 476-485, 2006.
- [65] K. Shiva, H. B. Rajendra, K. S. Subrahmanyam, A. J. Bhattacharyya, and C. N. R. Rao, “Improved Lithium Cyclability and Storage in Mesoporous SnO₂ Electronically Wired with Very Low Concentrations ($\leq 1\%$) of Reduced Graphene Oxide,” *Chemistry-a European Journal*, vol. 18, no. 15, pp. 4489-4494, 2012.
- [66] M. Mohamedi, S. J. Lee, D. Takahashi, M. Nishizawa, T. Itoh, and I. Uchida, “Amorphous tin oxide films: preparation and characterization as an anode active material for lithium ion batteries,” *Electrochimica Acta*, vol. 46, no. 8, pp. 1161-1168, 2001.
- [67] M. W. Xu, M. S. Zhao, F. Wang, W. Guan, S. Yang, and X. P. Song, “Facile synthesis and electrochemical properties of porous SnO₂ micro-tubes as anode material for lithium-ion battery,” *Materials Letters*, vol. 64, no. 8, pp. 921-923,

- 2010.
- [68] H. Wu, G. Chan, J. W. Choi, I. Ryu, Y. Yao, M. T. McDowell, S. W. Lee, A. Jackson, Y. Yang, L. B. Hu, and Y. Cui, "Stable cycling of double-walled silicon nanotube battery anodes through solid-electrolyte interphase control," *Nature Nanotechnology*, vol. 7, no. 5, pp. 309-314, 2012.
- [69] F. Lin, D. Nordlund, T. C. Weng, Y. Zhu, C. M. Ban, R. M. Richards, and H. L. Xin, "Phase evolution for conversion reaction electrodes in lithium-ion batteries," *Nature Communications*, vol. 5, 2014.
- [70] T. Moon, C. Kim, S. T. Hwang, and B. Park, "Electrochemical properties of disordered-carbon-coated SnO₂ nanoparticles for Li rechargeable batteries," *Electrochemical and Solid State Letters*, vol. 9, no. 9, pp. A408-A411, 2006.
- [71] C. Kim, M. Noh, M. Choi, J. Cho, and B. Park, "Critical size of a nano SnO₂ electrode for Li-secondary battery," *Chemistry of Materials*, vol. 17, no. 12, pp. 3297-3301, 2005.
- [72] H. S. Im, Y. J. Cho, Y. R. Lim, C. S. Jung, D. M. Jang, J. Park, F. Shojaei, and H. S. Kang, "Phase Evolution of Tin Nanocrystals in Lithium Ion Batteries," *Acs Nano*, vol. 7, no. 12, pp. 11103-11111, 2013.
- [73] L. P. Xu, C. Kim, A. K. Shukla, A. G. Dong, T. M. Mattox, D. J. Milliron, and J. Cabana, "Monodisperse Sn Nanocrystals as a Platform for the Study of Mechanical Damage during Electrochemical Reactions with Li," *Nano Letters*, vol. 13, no. 4, pp. 1800-1805, 2013.
- [74] D. Aurbach, "Review of selected electrode-solution interactions which determine the performance of Li and Li ion batteries," *Journal of Power Sources*, vol. 89, no. 2, pp. 206-218, 2000.
- [75] P. Verma, P. Maire, and P. Novak, "A review of the features and analyses of the solid electrolyte interphase in Li-ion batteries," *Electrochimica Acta*, vol. 55, no. 22, pp. 6332-6341, 2010.
- [76] A. G. Fox, M. A. Okeefe, and M. A. Tabbernor, "Relativistic Hartree-Fock X-Ray and Electron Atomic Scattering Factors at High Angles," *Acta Crystallographica Section A*, vol. 45, pp. 786-793, 1989.
- [77] E. Lee, and K. A. Persson, "Structural and Chemical Evolution of the Layered Li-Excess Li_xMnO₃ as a Function of Li Content from First-Principles Calculations," *Advanced Energy Materials*, vol. 4, no. 15, 2014.
- [78] N. Jiang, and J. C. H. Spence, "Core-hole effects on electron energy-loss spectroscopy of Li₂O," *Physical Review B*, vol. 69, no. 11, 2004.

- [79] H. Zheng, Y. Liu, S. X. Mao, J. B. Wang, and J. Y. Huang, "Beam-assisted large elongation of in situ formed Li₂O nanowires," *Scientific Reports*, vol. 2, 2012.
- [80] Y. C. Lu, D. G. Kwabi, K. P. C. Yao, J. R. Harding, J. G. Zhou, L. Zuin, and Y. Shao-Horn, "The discharge rate capability of rechargeable Li-O₂ batteries," *Energy & Environmental Science*, vol. 4, no. 8, pp. 2999-3007, 2011.
- [81] M. J. van Setten, V. A. Popa, G. A. de Wijs, and G. Brocks, "Electronic structure and optical properties of lightweight metal hydrides," *Physical Review B*, vol. 75, no. 3, 2007.
- [82] A. H. Reshak, "MgH₂ and LiH metal hydrides crystals as novel hydrogen storage material: Electronic structure and optical properties," *International Journal of Hydrogen Energy*, vol. 38, no. 27, pp. 11946-11954, 2013.
- [83] U. Boesenberg, M. A. Marcus, A. K. Shukla, T. H. Yi, E. McDermott, P. F. Teh, M. Srinivasan, A. Moewes, and J. Cabana, "Asymmetric pathways in the electrochemical conversion reaction of NiO as battery electrode with high storage capacity," *Scientific Reports*, vol. 4, 2014.
- [84] G. Kresse, and J. Furthmuller, "Efficient iterative schemes for ab initio total-energy calculations using a plane-wave basis set," *Physical Review B*, vol. 54, no. 16, pp. 11169-11186, 1996.
- [85] S. Lee, K. Park, W. Kim, S. Yoon, S. Hong, K. Kang, and M. Kim, "Unveiling origin of additional capacity of SnO₂ anode in lithium-ion batteries by realistic ex situ TEM analysis," *Nano Energy*, vol. 19, pp. 234-245, 2016.
- [86] K. J. Takeuchi, S. Z. Yau, A. Subramanian, A. C. Marschilok, and E. S. Takeuchi, "The Electrochemistry of Silver Hollandite Nanorods, Ag_xMn₈O₁₆: Enhancement of Electrochemical Battery Performance via Dimensional and Compositional Control," *Journal of the Electrochemical Society*, vol. 160, no. 5, pp. A3090-A3094, 2013.
- [87] M. J. Lee, S. Lee, P. Oh, Y. Kim, and J. Cho, "High Performance LiMn₂O₄ Cathode Materials Grown with Epitaxial Layered Nanostructure for Li-Ion Batteries," *Nano Letters*, vol. 14, no. 2, pp. 993-999, 2014.
- [88] Z. Y. Cai, L. Xu, M. Y. Yan, C. H. Han, L. He, K. M. Hercule, C. J. Niu, Z. F. Yuan, W. W. Xu, L. B. Qu, K. N. Zhao, and L. Q. Mai, "Manganese Oxide/Carbon Yolk-Shell Nanorod Anodes for High Capacity Lithium Batteries," *Nano Letters*, vol. 15, no. 1, pp. 738-744, 2015.
- [89] D. A. Tompsett, and M. S. Islam, "Electrochemistry of Hollandite alpha-MnO₂: Li-Ion and Na-Ion Insertion and Li₂O Incorporation," *Chemistry of Materials*,

- vol. 25, no. 12, pp. 2515-2526, 2013.
- [90] Y. F. Yuan, S. M. Wood, K. He, W. T. Yao, D. Tompsett, J. Lu, A. M. Nie, M. S. Islam, and R. Shahbazian-Yassar, "Atomistic Insights into the Oriented Attachment of Tunnel-Based Oxide Nanostructures," *Acs Nano*, vol. 10, no. 1, pp. 539-548, 2016.
- [91] T. Sasaki, S. Komaba, N. Kumagai, and I. Nakai, "Synthesis of hollandite-type K-gamma(Mn_{1-x}Mx)O₂ (M = Co, Fe) by oxidation of Mn(II) precursor and preliminary results on electrode characteristics in rechargeable lithium batteries," *Electrochemical and Solid State Letters*, vol. 8, no. 9, pp. A471-A475, 2005.
- [92] J. C. Perez-Flores, C. Baehtz, A. Kuhn, and F. Garcia-Alvarado, "Hollandite-type TiO₂: a new negative electrode material for sodium-ion batteries," *Journal of Materials Chemistry A*, vol. 2, no. 6, pp. 1825-1833, 2014.
- [93] C. Z. Wu, and Y. Xie, "Promising vanadium oxide and hydroxide nanostructures: from energy storage to energy saving," *Energy & Environmental Science*, vol. 3, no. 9, pp. 1191-1206, 2010.
- [94] N. Sharma, J. Plevert, G. V. S. Rao, B. V. R. Chowdari, and T. J. White, "Tin oxides with hollandite structure as anodes for lithium ion batteries," *Chemistry of Materials*, vol. 17, no. 18, pp. 4700-4710, 2005.
- [95] P. Mahadevan, A. Kumar, D. Choudhury, and D. D. Sarma, "Charge Ordering Induced Ferromagnetic Insulator: K₂Cr₈O₁₆," *Physical Review Letters*, vol. 104, no. 25, 2010.
- [96] L. H. Li, C. Y. Nan, J. Lu, Q. Peng, and Y. D. Li, "alpha-MnO₂ nanotubes: high surface area and enhanced lithium battery properties," *Chemical Communications*, vol. 48, no. 55, pp. 6945-6947, 2012.
- [97] Y. F. Yuan, A. M. Nie, G. M. Odegard, R. Xu, D. H. Zhou, S. Santhanagopalan, K. He, H. Asayesh-Ardakani, D. D. Meng, R. F. Klie, C. Johnson, J. Lu, and R. Shahbazian-Yassar, "Asynchronous Crystal Cell Expansion during Lithiation of K⁺-Stabilized alpha-MnO₂," *Nano Letters*, vol. 15, no. 5, pp. 2998-3007, 2015.
- [98] C. Ling, and F. Mizuno, "Capture Lithium in alpha MnO₂: Insights from First Principles," *Chemistry of Materials*, vol. 24, no. 20, pp. 3943-3951, 2012.
- [99] X. P. Fang, X. Lu, X. W. Guo, Y. Mao, Y. S. Hu, J. Z. Wang, Z. X. Wang, F. Wu, H. K. Liu, and L. Q. Chen, "Electrode reactions of manganese oxides for secondary lithium batteries," *Electrochemistry Communications*, vol. 12, no.

- 11, pp. 1520-1523, 2010.
- [100] A. S. Poyraz, J. Huang, S. Cheng, D. C. Bock, L. Wu, Y. Zhu, A. C. Marschilok, K. J. Takeuchi, and E. S. Takeuchi, "Effective recycling of manganese oxide cathodes for lithium based batteries," *Green Chem.*, vol. 18, pp. 3414-3421, 2016.
- [101] A. S. Poyraz, J. Huang, L. Wu, D. C. Bock, Y. Zhu, A. C. Marschilok, K. J. Takeuchi, and E. S. Takeuchi, "Potassium-Based α -Manganese Dioxide Nanofiber Binder-Free Self-Supporting Electrodes: A Design Strategy for High Energy Density Batteries," *Energy Technology*, vol. 4, no. 11, pp. 1358-1368, 2016.
- [102] J. Yuan, X. Liu, O. Akbulut, J. Hu, S. L. Suib, J. Kong, and F. Stellacci, "Superwetting nanowire membranes for selective absorption," *Nat Nanotechnol*, vol. 3, no. 6, pp. 332-336, 2008.
- [103] F. Wang, H. C. Yu, M. H. Chen, L. J. Wu, N. Pereira, K. Thornton, A. Van der Ven, Y. M. Zhu, G. G. Amatucci, and J. Graetz, "Tracking lithium transport and electrochemical reactions in nanoparticles," *Nature Communications*, vol. 3, 2012.
- [104] K. He, Y. N. Zhou, P. Gao, L. P. Wang, N. Pereira, G. G. Amatucci, K. W. Nam, X. Q. Yang, Y. M. Zhu, F. Wang, and D. Su, "Sodiation via Heterogeneous Disproportionation in FeF₂ Electrodes for Sodium-Ion Batteries," *Acs Nano*, vol. 8, no. 7, pp. 7251-7259, 2014.
- [105] Y. Liu, N. S. Hudak, D. L. Huber, S. J. Limmer, J. P. Sullivan, and J. Y. Huang, "In Situ Transmission Electron Microscopy Observation of Pulverization of Aluminum Nanowires and Evolution of the Thin Surface Al₂O₃ Layers during Lithiation-Delithiation Cycles," *Nano Letters*, vol. 11, no. 10, pp. 4188-4194, 2011.
- [106] K. E. Gregorczyk, Y. Liu, J. P. Sullivan, and G. W. Rubloff, "In Situ Transmission Electron Microscopy Study of Electrochemical Lithiation and Delithiation Cycling of the Conversion Anode RuO₂," *Acs Nano*, vol. 7, no. 7, pp. 6354-6360, 2013.
- [107] J. H. Rask, B. A. Miner, and P. R. Buseck, "Determination of Manganese Oxidation-States in Solids by Electron Energy-Loss Spectroscopy," *Ultramicroscopy*, vol. 21, no. 4, pp. 321-326, 1987.
- [108] H. Kurata, and C. Colliex, "Electron-Energy-Loss Core-Edge Structures in Manganese Oxides," *Physical Review B*, vol. 48, no. 4, pp. 2102-2108, 1993.

- [109] S. Lee, L. Wu, A. S. Poyraz, A. C. Marschlok, E. S. Takeuchi, Y. Zhu, and M. Kim, "Lithiation mechanism of tunnel-structured alpha-MnO₂ material revealed by in situ TEM," in preparation.

요약(국문초록)

리튬이온전지는 에너지 밀도가 높아 휴대용 전자기기의 에너지원으로 널리 이용되고 있지만, 이차전지 만으로 구동이 가능한 전기 자동차 등의 개발을 위해 여전히 많은 연구가 필요하다. 이에 따라 리튬이온전지 전극 재료의 전기화학 반응 메커니즘을 규명하고 성능 향상을 위한 효과적인 방향을 제시하기 위해 다양한 분석 방법들을 이용하여 수많은 연구들이 이루어져 왔다. 특히 투과전자현미경(TEM) 연구는 나노 수준에서 전기화학 반응 메커니즘을 밝힐 수 있다는 점에서 매우 강력한 분석 기술이지만, 리튬이온전지에서 일어나는 반응을 있는 그대로 해석하기 위해 특별한 환경 설정과 샘플링 방법을 필요로 하기 때문에 많은 제약이 있어 분석을 어렵게 만든다. 따라서 우리는 리튬이온전지 전극 재료의 전기화학 반응을 잘 묘사할 수 있는 투과전자현미경 연구 접근 방식에 초점을 맞추어 연구를 진행하였고, 투과전자현미경 연구 기술을 발전시키고 그 기술을 특정 목적에 적절하게 적용함으로써 다양한 리튬이온전지 전극 재료의 반응 메커니즘에 대한 이슈들을 해결하였다.

먼저, 니켈 함량이 풍부한 니켈코발트망간(NCM) 양극 재료에서 나타나는 빠른 용량 저하 현상의 근원을 밝혀내기 위하여, 우리는 집속이온빔(FIB) 샘플링 기술을 활용하여 니켈코발트망간 1/1/1 과 8/1.5/0.5 양극 재료의 이차 입자 내부를 직접적으로 비교하였다. 주사전자현미경(SEM)과 투과전자현미경을 이용하여 이차 입자의 사이클 전후 단면을 관찰함으로써 니켈이 풍부한 니켈코발트망간 재료의 부피 팽창 현상으로 나타나는 일차 입자 간의 균열과 심각한 표면 저하 현상과

이 빠른 용량 저하의 주요한 원인인 것으로 파악되었다. 표면 저하 현상은 니켈 3+ 이온의 불안정성으로 인해 발생하는 표면의 구조적 변형과 전이금속 이온들의 전해질로의 용해 때문일 것으로 추론되었다. 또한 우리는 일차 입자 내부에 존재하는 저각 결정립계들이 일차 입자 내에서 균열을 일으키는 근원지임을 밝혀내었고, 니켈이 풍부한 니켈코발트망간 양극 재료의 빠른 용량 저하 현상의 또 다른 원인이 될 수 있음을 확인하였다.

더 나아가 우리는 비실시간 투과전자현미경 실험 방법을 발전시켜 산화주석(SnO_2) 음극 재료의 상 변화 과정을 추적 관찰하였고, 역 변환 과정의 가능성과 추가 용량의 근원을 밝혀내었다. 산화주석 입자가 분산된 투과전자현미경용 구리 그리드를 일반적인 슬러리 전극과 함께 코인 셀 전지 안에 놓아 전기화학적으로 충·방전시킴으로써, 같은 입자들에서의 상 변화 과정을 투과전자현미경으로 추적하여 연구할 수 있었다. 이러한 방법을 통해 우리는 산화리튬(Li_2O)의 반응이 추가 용량에 기여하며, 역 변환 반응을 통해 일산화주석(SnO)은 일부 재형성될 수 있지만 이산화주석(SnO_2)은 형성되지 않음을 밝혀내었다.

마지막으로, 우리는 터널 구조를 가진 산화망간(MnO_2) 나노와이어의 실제 리튬 확산 경로와 리튬 삽입 메커니즘을 규명하기 위하여 실시간 투과전자현미경 실험 기술을 적용하였다. 탄소 필름이 증착된 투과전자현미경용 그리드를 활용하여 특수한 실험 환경을 조성함으로써, 우리는 알파 산화망간 나노와이어 내에서의 터널을 통한 빠른 확산을 증명하였고, 알파 산화망간 재료에 리튬이 완전히 삽입되는 과정까지의 메커니즘을 정밀하게 밝혀내었다. 변환 반응이 일어나는 동안 터널이

부분적으로 붕괴하면서 망간 이온이 본래의 위치에서 일산화망간(MnO) 중간상을 형성함을 확인하였다. 더 나아가 리튬 이온이 완전히 삽입된 이후에도 리튬과 산소 이온이 일차원 배열을 잘 유지함을 밝혀내었다.

이러한 연구를 통해 이차 전지 분석에 다양하게 적용할 수 있는 유용한 투과전자현미경 실험 기술을 소개할 뿐만 아니라, 전도유명한 다양한 리튬이온전지 전극 재료들의 전기화학 반응 메커니즘에 대한 근본적인 정보들을 제공함으로써, 투과전자현미경과 리튬이온전지 분야 모두의 발전에 기여할 수 있을 것으로 기대한다.

주요어: 리튬이온전지, 전기화학 반응 메커니즘, 투과전자현미경, 실시간 투과전자현미경, 리튬 니켈코발트망간 산화물, 산화주석(SnO₂), 산화망간(MnO₂).

학 번: 2012-24165